arXiv:1411.0589v2 [stat.ML] 30 Dec 2014

Modular proximal optimization for multidimensional total-variation regularization

Álvaro Barbero alvaro.barbero@uam.es
Instituto de Ingeniería del Conocimiento and Universidad Autónoma de Madrid
Francisco Tomás y Valiente 11, Madrid, Spain

Suvrit Sra* suvrit@gmail.com
Max Planck Institute for Intelligent Systems, Tübingen, Germany

Abstract

One of the most frequently used notions of "structured sparsity" is that of sparse (discrete) gradients, a structure typically elicited through *Total-Variation (TV)* regularizers. This paper focuses on anisotropic TV-regularizers, in particular on ℓ_p-norm *weighted TV regularizers* for which it develops efficient algorithms to compute the corresponding proximity operators. Our algorithms enable one to scalably incorporate TV regularization of vector, matrix, or tensor data into a proximal convex optimization solvers. For the special case of vectors, we derive and implement a highly efficient weighted 1D-TV solver. This solver provides a backbone for subsequently handling the more complex task of higher-dimensional (two or more) TV by means of a modular proximal optimization approach. We present numerical experiments that demonstrate how our 1D-TV solver matches or exceeds the best known 1D-TV solvers. Thereafter, we illustrate the benefits of our modular design through extensive experiments on: (i) image denoising; (ii) image deconvolution; (iii) four variants of fused-lasso; and (iv) video denoising. Our results show the flexibility and speed our TV solvers offer over competing approaches. To underscore our claims, we provide our TV solvers in an easy to use multi-threaded C++ library (which also aids reproducibility of our results).

1 Introduction

Sparsity impacts the entire data analysis pipeline, touching algorithmic, mathematical modeling, as well as practical aspects. Sparsity is frequently elicited through ℓ_1-norm regularization [Tibshirani, 1996, Candès and Tao, 2004]. But more refined, "structured" notions of sparsity are also greatly valuable: e.g., groupwise-sparsity [Meier et al., 2008, Liu and Zhang, 2009, Yuan and Lin, 2006, Bach et al., 2011], hierarchical sparsity [Bach, 2010, Mairal et al., 2010], gradient sparsity [Rudin et al., 1992, Vogel and Oman, 1996, Tibshirani et al., 2005], or sparsity over structured 'atoms' [Chandrasekaran et al., 2012].

Typical sparse models in machine learning involve problems of the form

$$\min_{\boldsymbol{x}\in\mathbb{R}^n} \quad \Phi(\boldsymbol{x}) := \ell(\boldsymbol{x}) + r(\boldsymbol{x}), \tag{1.1}$$

where $\ell : \mathbb{R}^n \to \mathbb{R}$ is (usually) a convex and smooth loss function, while $r : \mathbb{R}^n \to \mathbb{R} \cup \{+\infty\}$ is (usually) a lower semicontinuous, convex, and nonsmooth regularizer that induces sparsity. For example, if $\ell(\boldsymbol{x}) = \frac{1}{2}\|\boldsymbol{A}\boldsymbol{x} - \boldsymbol{b}\|_2^2$ and $r(\boldsymbol{x}) = \|\boldsymbol{x}\|_1$, we obtain the Lasso problem [Tibshirani, 1996]; more complex choices of $r(\boldsymbol{x})$ help model richer structure—for a longer exposition of several such choices of $r(\boldsymbol{x})$ see e.g., Bach et al. [2011].

We focus on instances of (1.1) where r is a weighted *anisotropic Total-Variation* (TV) regularizer[1], which, for a vector $\boldsymbol{x} \in \mathbb{R}^n$ and a fixed set of weights $\boldsymbol{w} \geq 0$ is defined as

$$r(\boldsymbol{x}) \stackrel{\text{def}}{=} \mathrm{Tv}_p^1(\boldsymbol{w};\boldsymbol{x}) \stackrel{\text{def}}{=} \Big(\sum\nolimits_{j=1}^{n-1} w_j|x_{j+1} - x_j|^p\Big)^{1/p} \quad p \geq 1. \tag{1.2}$$

*Part of this work was done when the author was visiting Carnegie Mellon University (2013-14)
[1]We use the term "anisotropic" to refer to the specific TV penalties considered in this paper.

More generally, if X is an order-m tensor in $\mathbb{R}^{\prod_{j=1}^{m} n_j}$ with entries $\mathsf{X}_{i_1,i_2,\ldots,i_m}$ ($1 \le i_j \le n_j$ for $1 \le j \le m$); we define the weighted *m-dimensional anisotropic TV* regularizer

$$\mathrm{Tv}^m_{\boldsymbol{p}}(\mathsf{W};\mathsf{X}) \stackrel{\text{def}}{=} \sum_{k=1}^{m} \sum_{I_k=\{i_1,\ldots,i_m\}\setminus i_k} \Big(\sum_{j=1}^{n_k-1} w_{I_k,j} |\mathsf{X}^{[k]}_{j+1} - \mathsf{X}^{[k]}_{j}|^{p_k} \Big)^{1/p_k}, \tag{1.3}$$

where $\mathsf{X}^{[k]}_j \equiv \mathsf{X}_{i_1,\ldots,i_{k-1},j,i_{k+1},\ldots,i_m}$, $w_{I_k,j} \ge 0$ are weights, and $\boldsymbol{p} \equiv [p_k \ge 1]$ for $1 \le k \le m$. If X is a matrix, expression (1.3) reduces to (note, $p, q \ge 1$)

$$\mathrm{Tv}^2_{p,q}(\mathsf{W};\mathsf{X}) = \sum_{i=1}^{n_1} \Big(\sum_{j=1}^{n_2-1} w_{1,j} |x_{i,j+1} - x_{i,j}|^p \Big)^{1/p} + \sum_{j=1}^{n_2} \Big(\sum_{i=1}^{n_1-1} w_{2,i} |x_{i+1,j} - x_{i,j}|^q \Big)^{1/q}, \tag{1.4}$$

These definitions look formidable, and are indeed nontrivial; already 2D-TV (1.4) or even the simplest 1D-TV (1.2) are fairly complex, which can complicate the overall optimization problem (1.1). Fortunately, their complexity can be "localized" by wrapping into using the notion of *prox-operators* [Moreau, 1962], which are now widely used across machine learning [Sra et al., 2011]—see also the classic work on the proximal-point method [Martinet, 1970, Rockafellar, 1976].

The main idea of using prox-operators while solving (1.1) is as follows. Suppose Φ is a convex lsc function on a set $\mathcal{X} \subset \mathbb{R}^n$. The *prox-operator* of Φ is defined as the map

$$\mathrm{prox}_\Phi \stackrel{\text{def}}{=} \boldsymbol{y} \mapsto \operatorname*{argmin}_{\boldsymbol{x}\in\mathcal{X}} \quad \tfrac{1}{2}\|\boldsymbol{x}-\boldsymbol{y}\|_2^2 + \Phi(\boldsymbol{x}) \quad \text{for} \quad \boldsymbol{y} \in \mathbb{R}^n. \tag{1.5}$$

This map is used in the *proximal-point* method to minimize $\Phi(\boldsymbol{x})$ over $\mathcal{X}$ by iterating

$$\boldsymbol{x}_{k+1} = \mathrm{prox}_\Phi(\boldsymbol{x}_k), \quad k = 0, 1, \ldots. \tag{1.6}$$

Applying (1.6) directly can be impractical: computing prox_Φ may be even harder than minimizing Φ! But for problems that have a *composite objective* $\Phi(\boldsymbol{x}) \equiv \ell(\boldsymbol{x}) + r(\boldsymbol{x})$, instead of iteration (1.6), closely related *proximal splitting* methods may be more effective.

Here, one 'splits' the optimization into two parts: a part that depends only on $\nabla\ell$ and another that computes prox_r, a step typically much easier than computing prox_Φ. This idea is realized by the *proximal gradient method* (also known as 'forward backward splitting'), which performs a gradient (forward) step followed by a proximal (backward) step to iterate

$$\boldsymbol{x}_{k+1} = \mathrm{prox}_{\eta_k r}(\boldsymbol{x}_k - \eta_k \nabla\ell(\boldsymbol{x}_k)), \quad k = 0, 1, \ldots. \tag{1.7}$$

Numerous other proximal splitting methods exist—please see [Beck and Teboulle, 2009, Nesterov, 2007, Combettes and Pesquet, 2009, Kim et al., 2010, Schmidt et al., 2011] and the references therein for additional examples.

Iteration (1.7) suggests that to profit from proximal splitting we must implement the prox-operator prox_r efficiently. An additional concern is whether the overall proximal splitting algorithm requires *exact* computation of prox_r, or moderately *inexact* computations are sufficient. This concern is very practical: rarely does r admit an exact algorithm for computing prox_r. Fortunately, proximal methods easily admit inexactness, e.g., [Schmidt et al., 2011, Salzo and Villa, 2012, Sra, 2012], which allows approximate prox-operators (as long as the approximation is sufficiently accurate).

1.1 Contributions

In light of the above background and motivation, we focus on computing prox-operators for TV regularizers, for which we develop, analyze, and implement a variety of fast algorithms. The ensuing contributions of this paper are summarized below.

- A new algorithm for ℓ_1-norm *weighted* 1D-TV proximity, which not only matches Condat's remarkably fast method [Condat, 2012] for unweighted TV, but provides the fastest (to our knowledge) method for weighted TV; moreover, it has an intuitive derivation.
- Efficient prox-operators for general ℓ_p-norm ($p \geq 1$) 1D-TV. In particular,
  - For $p = 1$ we also derive a projected-Newton method, which, though slower than our new algorithm, is of instructive value while also providing a practical framework for some subroutines needed for handling the difficult $p > 1$ case. Moreover, our derivations may be useful to readers seeking efficient prox-operators for other problems with structures similar to TV (e.g., ℓ_1-trend filtering [Kim et al., 2009, Tibshirani, 2014]); in fact our projected-Newton ideas provided a basis for the recent fast "group fused-lasso" algorithms of [Wytock et al., 2014].
  - For $p = 2$, we present a specialized Newton method based on root-finding, while for the general $p > 1$ case we describe both "projection-free" and projection based first-order methods.
- Scalable algorithms based on proximal-splitting techniques for computing 2D (1.4) and higher-D TV (1.3) prox-operators; our algorithms are designed to reuse our fast 1D-TV routines and to exploit the massive parallelization inherent in matrix and tensor TV problems.
- The practically most important contribution of our paper is a well-tuned, multi-threaded open-source C++ implementation of our algorithms.[2,3]

To complement our algorithmic contribution, we illustrate several applications of TV prox-operators: (i) to image and video denoising; (ii) as subroutines in some image deconvolution solvers; and (iii) as regularizers in four variants of fused-lasso.

Note: Our paper strives to support reproducible research. Given the vast attention that TV problems have received in the literature, we find it is valuable to both users of TV and other researchers to have access to our code, datasets, and scripts, to independently verify our claims, if desired.[4]

1.2 Related work

The literature on TV is dauntingly large, so we will not attempt any pretense at comprehensiveness. Instead, we mention some of the most directly related work for placing our contributions in perspective.

We focus on *anisotropic*-TV (in the sense of [Bioucas-Dias and Figueiredo, 2007]), in contrast to *isotropic*-TV [Rudin et al., 1992]. Like isotropic TV, anisotropic-TV is also amenable to efficient optimization, and proves quite useful in applications seeking parameters with sparse (discrete) gradients.

The anisotropic TV regularizers $\mathrm{Tv}_1^{1\mathrm{D}}$ and $\mathrm{Tv}_{1,1}^{2\mathrm{D}}$ arise in image denoising and deconvolution [Dahl et al., 2010], in the fused-lasso [Tibshirani et al., 2005], in logistic fused-lasso [Kolar et al., 2010], in change-point detection [Harchaoui and Lévy-Leduc, 2010], in graph-cut based image segmentation [Chambolle and Darbon, 2009], in submodular optimization [Jegelka et al., 2013]; see also the related work in [Vert and Bleakley, 2010]. This broad applicability and importance of anisotropic TV is the key motivation towards developing carefully tuned proximity operators.

Isotropic TV regularization arises frequently in image denoising and signal processing, and quite a few TV-based denoising algorithms exist [Zhu and Chan, 2008, see e.g.]. Most TV-based methods, however, use the standard ROF model [Rudin et al., 1992]. There are also several methods tailored to anisotropic TV, e.g., those developed in the context of fused-lasso [Friedman et al., 2007, Liu et al., 2010], graph-cuts [Chambolle and Darbon, 2009], ADMM-style approaches [Combettes and Pesquet, 2009, Wahlberg et al., 2012], or fast methods based on dynamic programming [Johnson, 2013] or KKT

[2] See https://github.com/albarji/proxTV

[3] For instance, the recent paper of Jegelka et al. [2013] relies on our toolbox for achieving several of its state-of-the-art results on fast submodular function minimization.

[4] This material shall be made available at: http://suvrit.de/work/soft/tv.html

conditions analysis [Condat, 2012]. However, it seems that anisotropic TV norms other than ℓ_1 has not been studied much in the literature, although recognized as a form of Sobolev semi-norms [Pontow and Scherzer, 2009].

Previously, Vogel and Oman [1996] suggested a Newton approach for TV; they smoothed the objective, but noted that it leads to numerical difficulties. In contrast, we directly solve the nonsmooth problem. Recently, Liu et al. [2010] presented tuned algorithms for Tv_1^{1D}-proximity based on a careful "restart" heuristic; their methods show strong empirical performance but do not extend easily to higher-D TV. Our Newton-type methods outperform the tuned methods of [Liu et al., 2010], and fit nicely in a general algorithmic framework that allows tackling the harder two- and higher-D TV problems. The gains obtained are especially prominent for 2D fused-lasso, for which previously Friedman et al. [2007] presented a coordinate descent approach that turns out to be slower.

Recently, Goldstein T. [2009] presented a so-called "Split-Bregman" (SB) method that applies directly to 2D-TV. It turns out that this method is essentially a variant of the well-known ADMM method. In contrast to our 2D approach, the SB strategy followed by Goldstein T. [2009] is to rely on ℓ_1-soft thresholding substeps instead of 1D-TV substeps. From an implementation viewpoint, the SB approach is somewhat simpler, but not necessarily more accurate. Incidentally, sometimes such direct ADMM approaches turn out to be less effective than ADMM methods that rely on more complex 1D-TV prox-operators [Ramdas and Tibshirani, 2014].

For 1D-TV, there exist several direct methods that are exceptionally fast. We treat the 1D-TV problem in detail in Section 2, hence refer the reader to that section for discussion of closely related work on fast 1D-TV solvers. We note here, however, that in contrast to all previous fast solvers, our 1D-TV solver allows weights, a capability that can be very important in applications [Jegelka et al., 2013].

It is tempting to assume that existing isotropic algorithms, such as the state-of-the-art PDHG [Zhu and Chan, 2008] method, can be easily adapted to our problems. But this is not true. PDHG requires fine-tuning of its parameters, and to obtain fast performance its authors apply non-trivial adaptive rules that fail on our anisotropic model. In stark contrast, our solvers do not require *any parameter tuning*; the default values work across a wide spectrum of inputs.

It is worth highlighting that it is not just proximal solvers such as FISTA [Beck and Teboulle, 2009], SpaRSA [Wright et al., 2009], SALSA [Afonso et al., 2010], TwIST [Bioucas-Dias and Figueiredo, 2007], Trip [Kim et al., 2010], that can benefit from our fast prox-operators. All other 2D and higher-D TV solvers, e.g., [Yang et al., 2013], as well as the recent ADMM based trend-filtering solvers of Tibshirani [2014] immediately benefit (and in fact, even gain the ability to solve weighted versions of their problems, a feature that they currently lack).

Outline of the Paper

1 Introduction **1**

2 Prox Operators for 1D-TV **5**
2.1 TV-L1: Proximity for Tv_1^{1D} . . . 6
2.1.1 Optimized taut-string method for Tv_1^{1D} . . . 6
2.1.2 Optimized taut–string method for weighted Tv_1^{1D} . . . 10
2.1.3 Projected-newton for weighted Tv_1^{1D} . . . 12
2.2 TV-L2: Proximity for Tv_2^{1D} . . . 14
2.3 TV-Lp: Proximity for Tv_p^{1D} . . . 17
2.3.1 Efficient projection onto the ℓ_q-ball . . . 17
2.3.2 Frank-Wolf algorithm for TV ℓ_p proximity . . . 18
2.4 Prox operator for TV-L_∞ . . . 19

3 Prox operators for multidimensional TV **19**

4 1D-TV: Experiments and Applications 22

5 2D-TV: Experiments and Applications 29

6 Application of multidimensional TV 39

A Mathematical background 45

B proxTV toolbox 46

C Proof on the equality of taut-string problems 47

D Testing images and videos, and experimental results 48

2 Prox Operators for 1D-TV

We begin with the 1D-TV problem (1.2), for which we develop below carefully tuned algorithms. This tuning pays off: our weighted-TV algorithm offers a fast, robust, and low-memory (in fact, in place) algorithm, which is not only of independent value, but is also an ideal building block for scalably solving 2D- and higher-D TV problems.

To express (1.2) more compactly we introduce the usual *differencing matrix*

$$\boldsymbol{D} = \begin{pmatrix} -1 & 1 & & & \\ & -1 & 1 & & \\ & & & \ddots & \\ & & & -1 & 1 \end{pmatrix} \in \mathbb{R}^{(n-1)\times n},$$

using which, (1.2) becomes $\mathrm{Tv}_p^{1\mathrm{D}}(\boldsymbol{x}) = \|\boldsymbol{D}\boldsymbol{x}\|_p$. The associated prox-operator solves

$$\min_{\boldsymbol{x}\in\mathbb{R}^n} \quad \tfrac{1}{2}\|\boldsymbol{x}-\boldsymbol{y}\|_2^2 + \lambda\|\boldsymbol{D}\boldsymbol{x}\|_p. \tag{2.1}$$

The presence of $\boldsymbol{D}$ and well as the ℓ_p-norm makes (2.1) fairly challenging to solve; even the simpler variants for $p \in \{1, 2, \infty\}$ are nontrivial. When solving (2.1) we may equivalently consider its dual form (obtained using Proposition A.4 and formula (A.3), for instance):

$$\min_{\boldsymbol{u}\in\mathbb{R}^{n-1}} \quad \tfrac{1}{2}\|\boldsymbol{D}^T\boldsymbol{u}\|_2^2 - \boldsymbol{u}^T\boldsymbol{D}\boldsymbol{y}, \quad \text{s.t. } \|\boldsymbol{u}\|_q \le \lambda, \tag{2.2}$$

where $p^{-1}+q^{-1}=1$ and $\|\cdot\|_q$ is the *dual-norm* of $\|\cdot\|_p$. If $\boldsymbol{u}^*$ is the dual solution, then using KKT conditions we can recover the primal solution $\boldsymbol{x}^*$; indeed, using $\nabla_{\boldsymbol{x}} L = 0$, we obtain $\nabla_{\boldsymbol{x}}\left(\frac{1}{2}\|\boldsymbol{x}-\boldsymbol{y}\|_2^2 + \lambda\|\boldsymbol{z}\|_p + \boldsymbol{u}^T(\boldsymbol{D}\boldsymbol{x}-\boldsymbol{z})\right) = 0$, from which we obtain the primal solution

$$\boldsymbol{x}^* = \boldsymbol{y} - \boldsymbol{D}^T\boldsymbol{u}^*.$$

If we have a feasible dual variable $\boldsymbol{u}$, we can compute a candidate primal solution $\boldsymbol{x} = \boldsymbol{y} - \boldsymbol{D}^T\boldsymbol{u}$; the associated *duality gap* is given by (noting that we wrote (2.2) as a minimization):

$$\begin{aligned} \mathrm{gap}(\boldsymbol{x},\boldsymbol{u}) &\overset{\text{def}}{=} \tfrac{1}{2}\|\boldsymbol{x}-\boldsymbol{y}\|_2^2 + \lambda\|\boldsymbol{D}\boldsymbol{x}\|_p - \left(-\tfrac{1}{2}\|\boldsymbol{D}^T\boldsymbol{u}\|_2^2 - \boldsymbol{u}^T\boldsymbol{D}\boldsymbol{y}\right), \\ &= \lambda\|\boldsymbol{D}\boldsymbol{x}\|_p - \boldsymbol{u}^T\boldsymbol{D}\boldsymbol{x}. \end{aligned} \tag{2.3}$$

The duality gap provides a handy stopping criterion for many of our algorithms.

With these basic ingredients we are now ready to present specialized 1D-TV algorithms for different choices of p. The choices $p \in \{1, 2\}$ are the most common, so we treat them in greater detail—especially the case $p = 1$, which is the most important of all the TV problems studied below. Other choices of p find fewer practical applications, but we nevertheless cover them for completeness.

2.1 TV-L1: Proximity for $\mathbf{Tv}_1^{\mathbf{1D}}$

In this section we present two efficient methods for computing the $\mathrm{Tv}_1^{\mathrm{1D}}$ prox-operator. The first method employs a carefully tuned "taut-string" approach, while the second method adapts the classical projected-Newton (PN) method [Bertsekas, 1982] to TV. We first derive our methods for unweighted TV, before presenting details for the elementwise weighted TV problem (2.8). The previous fastest methods handle only unweighted-TV. It is is nontrivial to extend them to handle weighted-TV, a problem that is crucial to several applications, e.g., segmentation [Chambolle and Darbon, 2009] and certain submodular optimization problems Jegelka et al. [2013].

Taut-string approaches are already known to provide extremely efficient solutions to unweighted TV-L1, as seen in [Condat, 2012]. In addition to our optimized taut-string approach for weighted-TV, we also present details of a PN approach for its instructive value, and also because it provides key subroutines for solving $p > 1$ problems. Moreover, our derivation may be helpful to readers seeking to implement efficient prox-operators for other problems that have structure similar to TV, for instance ℓ_1-trend filtering [Kim et al., 2009, Tibshirani, 2014]. Indeed, the PN approach proved foundational for the recent fast "group fused-lasso" algorithms of [Wytock et al., 2014].

Before proceeding we note that other than [Condat, 2012], other efficient methods to address unweighted $\mathrm{Tv}_1^{\mathrm{1D}}$ proximity have been proposed. Johnson [2013] shows how solving $\mathrm{Tv}_p^{\mathrm{1D}}$ proximity is equivalent to computing the data likelihood of an specific Hidden Markov Model (HMM), which suggests a dynamic programming approach based on the well-known Viterbi algorithm for HMMs. The resulting algorithm is very competitive, and guarantees an overall $O(n)$ performance while requiring approximately $8n$ storage. We will also consider this algorithm in our experimental comparison in §4. Another, roughly similar approach to the proposed projected-Newton method was already presented in Ito and Kunisch [1999], which by means of an augmented Langrangian method a dual formulation is obtained and solved following a Newton–like strategy, though with the additional burden of requiring manual setting of a number of optimization parameters to ensure convergence.

2.1.1 Optimized taut-string method for $\mathbf{Tv}_1^{\mathbf{1D}}$

While taut-string methods seem to be largely unknown in machine learning, they have been widely applied in the field of statistics—see e.g. [Grasmair, 2007, Davies and Kovac, 2001]. Even the recent efficient method of Condat [2012]—though derived using KKT conditions of the dual problem (2.2) (for $p = 1, q = \infty$)—can be given a taut-string interpretation.

Below we introduce the general idea behind the taut-string approach and present our optimized version of it. Surprisingly, the resulting algorithm is equivalent to the fast algorithm of [Condat, 2012], though now with a clearer interpretation based on taut-strings, which proves key to obtaining a similarly fast method for weighted-TV.

For TV-L1 the dual problem (2.2) becomes

$$\min_{\boldsymbol{u}} \tfrac{1}{2}\|\boldsymbol{D}^T\boldsymbol{u}\|_2^2 - \boldsymbol{u}^T\boldsymbol{D}\boldsymbol{y}, \text{ s.t. } \|\boldsymbol{u}\|_\infty \leq \lambda, \tag{2.4}$$

whose objective can be (i.e., without changing the argmin) replaced by $\|\boldsymbol{D}^T\boldsymbol{u} - \boldsymbol{y}\|_2^2$, which upon using the structure of matrix $\boldsymbol{D}$ unfolds into

$$\left((u_1 - y_1)^2 + \sum\nolimits_{i=2}^{n-1}(-u_{i-1} + u_i - y_i)^2 + (-u_{n-1} - y_n)^2\right)^2.$$

Introducing the fixed extreme points $u_0 = u_n = 0$, we can thus replace the dual (2.4) by

$$\min_{\boldsymbol{u}} \sum\nolimits_{i=1}^{n}(y_i - u_i + u_{i-1})^2, \text{ s.t. } \|\boldsymbol{u}\|_\infty \leq \lambda, \quad u_0 = u_n = 0. \tag{2.5}$$

Now we perform a change of variables by defining the new set of variables $\boldsymbol{s} = \boldsymbol{r} - \boldsymbol{u}$, where $r_i := \sum_{k=1}^{i} y_k$ is the cumulative sum of input signal values. Thus, (2.5) becomes

$$\min_{\boldsymbol{s}} \sum_{i=1}^{n} (y_i - r_i + s_i + r_{i-1} - s_{i-1})^2, \text{ s.t. } \|\boldsymbol{s} - \boldsymbol{r}\|_\infty \leq \lambda, \quad r_0 - s_0 = r_n - s_n = 0,$$

which upon simplification becomes

$$\min_{\boldsymbol{s}} \sum_{i=1}^{n} (s_i - s_{i-1})^2, \quad \text{s.t.} \quad \|\boldsymbol{s} - \boldsymbol{r}\|_\infty \leq \lambda, s_0 = 0, \; s_n = r_n. \tag{2.6}$$

Now the key trick: Problem (2.6) can be shown to share the same optimum as

$$\min_{\boldsymbol{s}} \sum_{i=1}^{n} \sqrt{1 + (s_i - s_{i-1})^2}, \text{ s.t. } \|\boldsymbol{s} - \boldsymbol{r}\|_\infty \leq \lambda, \quad s_0 = 0, \; s_n = r_n. \tag{2.7}$$

A proof of this relationship may be found in [Steidl et al., 2005]; for completeness and also because this proof will serve us for the weighted $\mathrm{Tv}_1^{1\mathrm{D}}$ variant, we include an alternative proof in Appendix C.

The name "taut-string" is explained as follows. The objective in (2.7) can be interpreted as the euclidean length of a polyline through the points $(i, \boldsymbol{s}_i)$. Thus, (2.7) seeks the minimum length polyline (the *taut string*) crossing a tube of height λ with center the cumulative sum $\boldsymbol{r}$, and with the fixed endpoints (s_0, s_n). An example illustrating this is shown in Figure 1.

Once the taut string is found, the solution for the original proximity problem can be recovered by observing that

$$s_i - s_{i-1} \quad = \quad r_i - u_i - (r_{i-1} - u_{i-1}) \quad = \quad y_i - u_i + u_{i-1} \quad = \quad x_i,$$

where we used the primal-dual relation $\boldsymbol{x} = \boldsymbol{y} - \boldsymbol{D}^T \boldsymbol{u}$. Intuitively, the above argument shows that the solution to the TV-L1 proximity problem is obtained as the discrete gradient of the taut string, or as the slope of its segments.

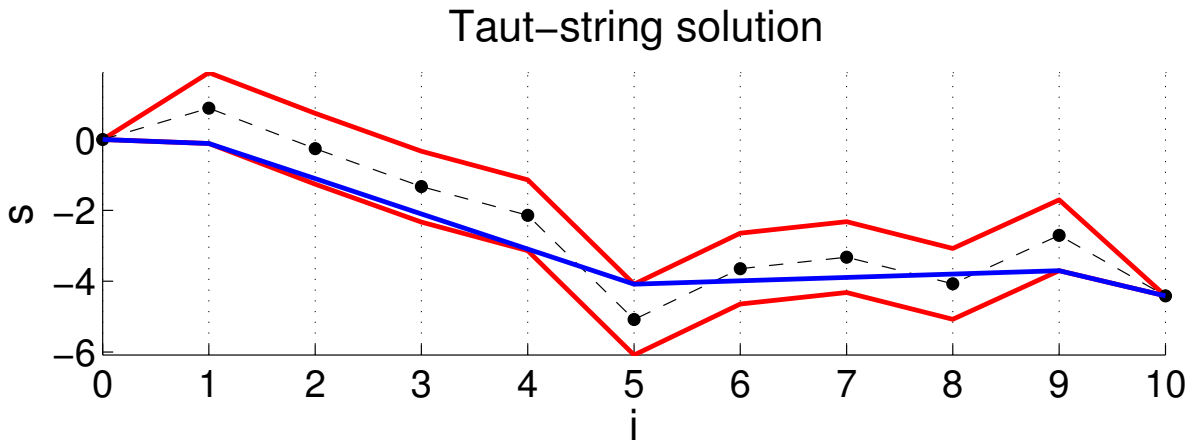

Figure 1: Example of the taut string method. The cumulative sum $\boldsymbol{r}$ of the input signal values $\boldsymbol{y}$ is shown as the dashed line; the black dots mark the points (i, r_i). The bottom and top of the λ-width tube are shown in red. The taut string solution $\boldsymbol{s}$ is shown as a blue line.

It remains to describe how to find the taut string. The most widely used approach seems to be the one of Davies and Kovac [2001]. This approach starts from the fixed point $s_0 = 0$, and incrementally

computes the *greatest convex minorant* of the upper bounds on the λ tube, as well as the *smallest concave majorant* of the lower bounds on the λ tube. When both curves intersect, a segment of the taut string can be identified and added to the solution. The procedure is then restarted at the end of the identified segment, and iterated until all taut string segments have been obtained.

In the worst-case, the identification of a single segment can require analyzing on the order of n points in the signal, and the taut string may contain up to n segments. Thus, the worst-case complexity of the taut-string approach is $O(n^2)$. However, as also noted in [Condat, 2012], in practice the performance is close to the best case $O(n)$. But in [Condat, 2012], it is noted that maintaining the minorant and majorant functions in memory is inefficient, whereby a taut-string approach is viewed as potentially inferior to their proposed method. Surprisingly, the geometry-aware construction of taut-strings that we propose below, yields in a method analogous to [Condat, 2012], both in space and time complexity. Owing to its intuitive derivation, our geometry-aware ideas extend naturally to weighted-TV—in our opinion, vastly more easily than the KKT-based derivations in [Condat, 2012].

Details. Our geometry-aware method requires only the following bookkeeping variables.

1. i_0: index of the current segment start
2. $\bar{\delta}$: slope of the line joining segment start with majorant at the current point
3. $\underline{\delta}$: slope of the line joining segment start with minorant at the current point
4. $\bar{h}$: height of majorant w.r.t. the λ-tube center
5. $\underline{h}$: height of minorant w.r.t. λ-tube center
6. $\bar{i}$: index of last point where $\bar{\delta}$ was updated—potential majorant break point
7. $\underline{i}$: index of last point where $\underline{\delta}$ was updated—potential minorant break point.

Figure 2 gives a geometric interpretation of these variables; we use these variables to detect minorant-majorant intersections, without the need to compute or store them explicitly.

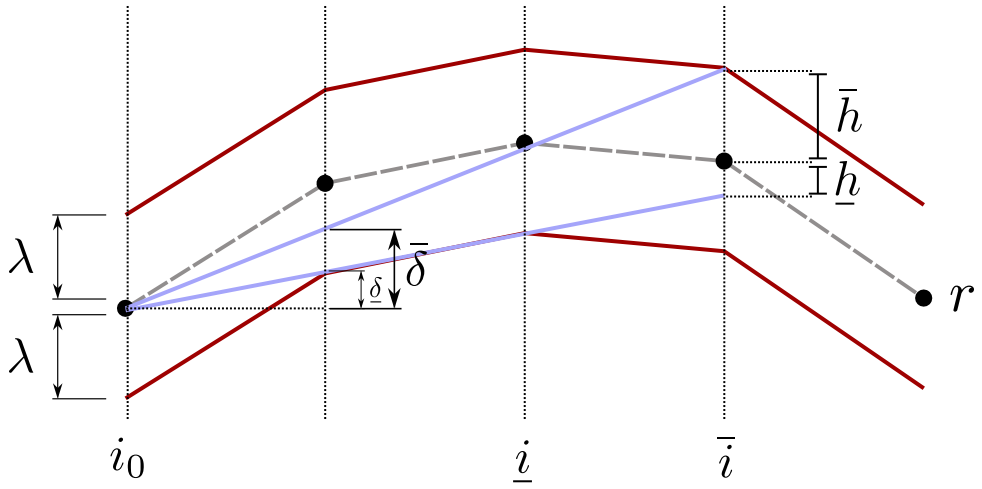

Figure 2: Illustration of the geometric concepts involved in our taut string method. The δ slopes and h heights are presented updated up to the index shown as $\bar{i}$.

Algorithm 1 presents full pseudocode of our optimized taut-string method. Starting from the initial point, the method tries to build a single segment traversing the λ-tube up to the end point r_n. In this way, at each iteration the method steps one point further through the tube, updating the maximum/minimum slope of each such hypothetical segment (δ) as well as the minimum/maximum height that each segment

Algorithm 1 Optimized taut string algorithm for TV-L1-proximity

Initialize $i = \bar{i} = \underline{i} = \bar{h} = \underline{h} = 0$, $\bar{\delta} = \infty$, $\underline{\delta} = -\infty$.
while $i < n$ **do**
  Find tube height: $\tilde{\lambda} = \lambda$ if $i < n-1$, else $\tilde{\lambda} = 0$
  Update minorant height following current slope: $\underline{h} = \underline{h} + \underline{\delta} - y_i$.
  /* Check for ceiling violation: minorant is above tube ceiling */
  if $\underline{h} > \tilde{\lambda}$ **then**
    Build valid segment up to last minorant breaking point: $\boldsymbol{x}_{i_0+1:\underline{i}} = \underline{\delta}$.
    Start new segment after break: $(i_0, \bar{i}) = \underline{i}$, $i = \underline{i} + 1$, $\bar{h} = \underline{h} = -\lambda$, $\bar{\delta} = \infty$, $\underline{\delta} = -\infty$
    continue
  end if
  Update majorant height following current slope: $\bar{h} = \bar{h} + \bar{\delta} - y_i$.
  /* Check for bottom violation: majorant is below tube bottom */
  if $\bar{h} < -\tilde{\lambda}$ **then**
    Build valid segment up to last majorant breaking point: $\boldsymbol{x}_{i_0+1:\bar{i}} = \bar{\delta}$.
    Start new segment after break: $(i_0, \underline{i}) = \bar{i}$, $i = \bar{i} + 1$, $\bar{h} = \underline{h} = \lambda$, $\bar{\delta} = \infty$, $\underline{\delta} = -\infty$
    continue
  end if
  /* Check if majorant height is above the ceiling */
  if $\bar{h} \geq \tilde{\lambda}$ **then**
    Correct slope: $\bar{\delta} = \bar{\delta} + \frac{\tilde{\lambda} - \bar{h}}{i - i_0}$
    We are touching the majorant: $\bar{h} = \tilde{\lambda}$
    This is a possible majorant breaking point: $\bar{i} = i$
  end if
  /* Check if minorant height is below the bottom */
  if $\underline{h} \leq -\tilde{\lambda}$ **then**
    Correct slope: $\underline{\delta} = \underline{\delta} + \frac{-\tilde{\lambda} - \underline{h}}{i - i_0}$
    We are touching the minorant: $\underline{h} = -\tilde{\lambda}$
    This is a possible minorant breaking point: $\underline{i} = i$
  end if
  Continue building current segment: $i = i + 1$
end while
Build last valid segment: $\boldsymbol{x}_{i_0+1:n} = \bar{\delta}$.

could have at the current point (h). If at some point the tube has limits such that the maximum height $\bar{h}$ falls below the tube bottom, or such that the minimum height $\underline{h}$ grows above the tube ceiling, then it is not possible to continue building the segment. In this event, the segment under construction must be broken at some point, and a new segment must be started after it. It can be shown that the segment must be broken at the point where it last touched the tube limits: either at the bottom limit if the segment has grown above the tube, or at the top limit if the segment has grown under the tube. With this criterion the segment is fixed from the starting point to such a breaking point and the procedure is restarted to build the next segment. Figure 3 visually shows an example of the algorithm's workings.

Height variables. It should be noted that in order to implement the method described above, the height variables h are not strictly necessary as they can be obtained from the slopes δ. However, explicitly including them leads to efficient updating rules at each iteration, as we show below.

Suppose we are updating the heights and slopes from their estimates at step $i-1$ to step i. Updating the heights is immediate given the slopes, as we have that

$$h_i = h_{i-1} + \delta - y_i,$$

which is to say, since we are following a line with slope δ, the change in height from one step to the

next is given by precisely such slope. Note, however, that in our algorithm we do not compute absolute heights but instead relative heights with respect to the λ–tube center. Therefore we need to account for the change in the tube center between steps $i-1$ and i, which is given by $r_i - r_{i-1} = y_i$. This completes the update, which is shown in Algorithm 1 as lines 4 and 11.

Of course it might well happen that the new height h runs over or under the tube. This would mean that we cannot continue using the current slope in the majorant or minorant, and a recalculation is needed, which again can be done efficiently by now using the height information. Let us assume, without loss of generality, that the starting index of the current segment is 0 and the absolute height of the starting point of the segment is given by α. Then, for adjusting the majorant slope $\bar{\delta}_i$ so that it touches the tube ceiling at the current point we note that

$$\bar{\delta}_i = \frac{\lambda + r_i - \alpha}{i} = \frac{\lambda + (\bar{h}_i - \bar{h}_i) + r_i - \alpha}{i},$$

where we have also added and subtracted the current value of $\bar{h}_i$. Observe that this value was computed using the estimate of the slope so far δ_{i-1}, so we can rewrite it as the projection of the initial point in the segment following such slope, that is, as $\bar{h}_i = i\bar{\delta}_i - r_i + \alpha$. Doing so for one of the added heights $\bar{h}_i$ produces

$$\bar{\delta}_i = \frac{\lambda + (i\bar{\delta}_{i-1} - r_i + \alpha) - \bar{h}_i + r_i - \alpha}{i} = \bar{\delta}_{i-1} + \frac{\lambda - \bar{h}_i}{i},$$

which generates a simple updating rule. A similar derivation holds for the minorant. The resultant updates are included in the algorithm in lines 20 and 26. After recomputing this slope we need to adjust the corresponding height back to the tube: since the heights are relative to the tube center we can just set $\bar{h} = \lambda$, $\underline{h} = -\lambda$; this is done in lines 21 and 27.

Notice also that the special case of the last point in the tube where the taut-string must meet $s_n = r_n$ is handled by line 3, where $\tilde{\lambda}$ is set to 0 at such a point to enforce this constraint. In practice, it is more efficient to add a separate step to the algorithm's main loop for handling this special case, as was already observed in Condat [2012]. Overall, one iteration of the method is very efficient, as mostly just additions and subtractions are involved with the sole exception of the fraction required for the slope updates, which are not performed at every iteration. Moreover, no additional memory is required beyond the constant number of bookkeeping variables, and in-place updates are also possible due to the fact that y_i values for already fixed sections of the taut-string are not required again, so the output $\boldsymbol{x}$ and the input $\boldsymbol{y}$ can both refer to the same memory locations.

2.1.2 Optimized taut–string method for weighted $\mathbf{Tv}_1^{\mathbf{1D}}$

Several applications TV require penalizing the discrete gradients individually, which can be done by solving the *weighted TV-L1* problem

$$\min_{\boldsymbol{x}} \quad \tfrac{1}{2}\|\boldsymbol{x} - \boldsymbol{y}\|_2^2 + \sum_{i=1}^{n-1} w_i |x_{i+1} - x_i|, \tag{2.8}$$

where the weights w_i are all positive. To solve (2.8) using our optimized taut-string approach, we again begin with its dual

$$\min_{\boldsymbol{u}} \quad \tfrac{1}{2}\|\boldsymbol{D}^T\boldsymbol{u}\|_2^2 - \boldsymbol{u}^T\boldsymbol{D}\boldsymbol{y} \quad \text{s.t.} \quad |u_i| \le w_i, \quad 1 \le i < n. \tag{2.9}$$

Then, we repeat the derivation of the unweighted taut-string method with a few key modifications. More precisely, we transform (2.9) by introducing $u_0 = u_n = 0$ to obtain

$$\min_{\boldsymbol{u}} \sum_{i=1}^{n} (y_i - u_i + u_{i-1})^2 \quad \text{s.t.} \quad |u_i| \le w_i, \quad 1 \le i < n.$$

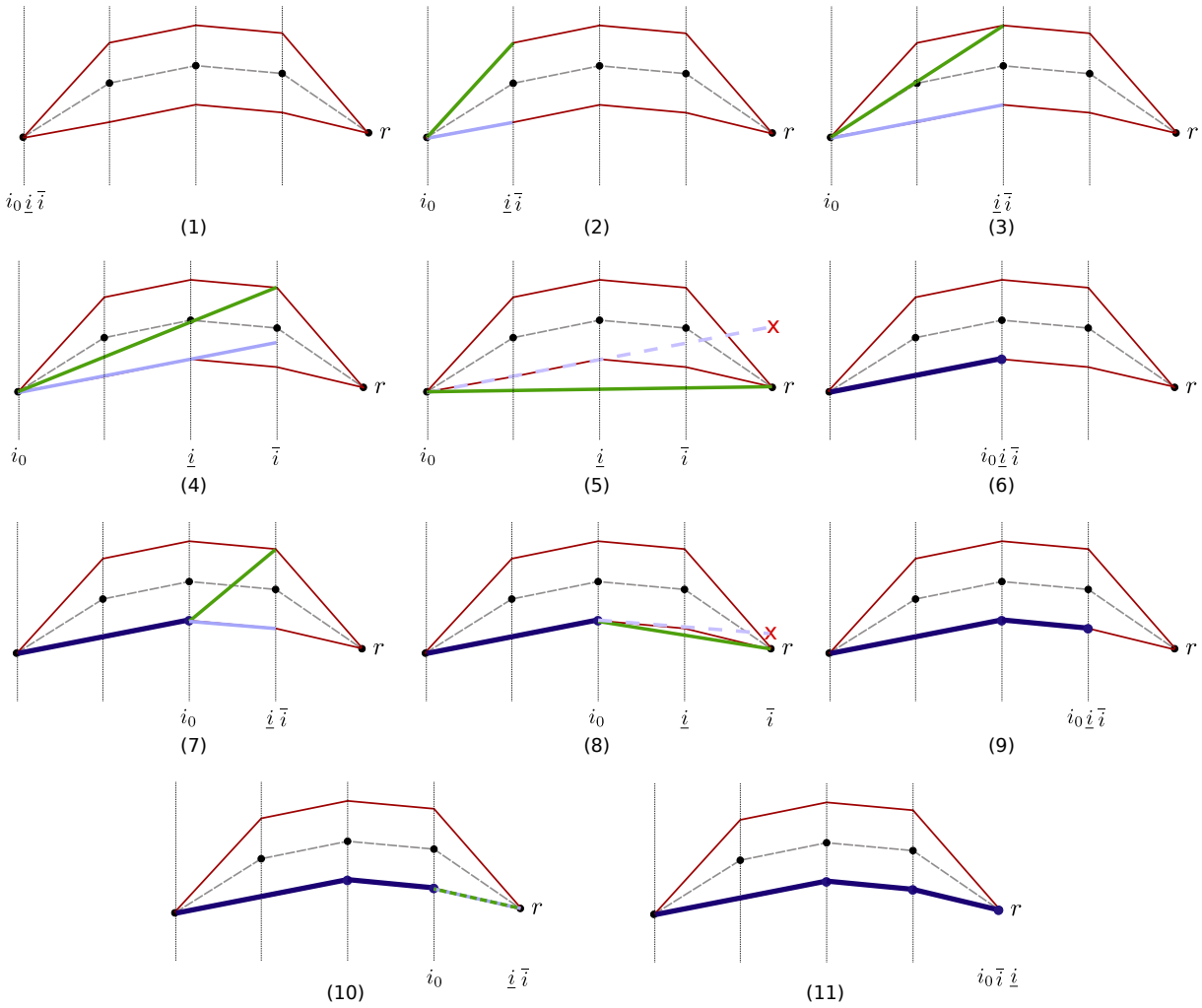

Figure 3: Example of the evolution of the proposed optimized taut string method. The majorant/minorant slopes are shown in green/blue colors, respectively. At step (1) the algorithm is initialized. Steps (2) to (4) successfully manage to update majorant/minorant slopes respecting the tube limits. At step (5), however, the minorant grows over the tube ceiling, and so it is necessary to break the segment. Since the one under violation is the minorant, it is broken at the point where it last touched the tube bottom. A segment piece is thus fixed at step (6), and the algorithm is restarted at its end. The slopes are updated at step (7), though at step (8) once again the minorant grows over the tube ceiling. Hence, at step (9) a breaking point is introduced again and the algorithm is restarted. Following this, step (10) manages to update majorant/minorant slopes up to the end of the tube, and so at step (11) the final segment is built using the (now equal) slopes.

Next, we perform the change of variable $\boldsymbol{s} = \boldsymbol{r} - \boldsymbol{u}$, where $r_i := \sum_{k=1}^{i} y_k$, and consider

$$\min_{\boldsymbol{s}} \sum_{i=1}^{n} (s_i - s_{i-1})^2 \quad \text{s.t. } |s_i - r_i| \leq w_i, \quad 1 \leq i < n \; s_0 = 0, \; s_n = r_n.$$

Finally, applying Theorem C.1 we obtain the equivalent *weighted taut-string* problem

$$\min_{\boldsymbol{s}} \sum_{i=1}^{n} \sqrt{1 + (s_i - s_{i-1})^2} \quad \text{s.t. } |s_i - r_i| \leq w_i, \; 1 \leq i < n, \; s_0 = 0, \; s_n = r_n. \tag{2.10}$$

Problem (2.10) differs from its unweighted counterpart (2.7) in the constraints $|s_i - r_i| \leq w_i$ $(1 \leq i < n)$, which allow different weights for each component instead of using the same value λ. Our geometric intuition also carries over to the weighted problem, albeit with a slight modification: the tube we are trying to traverse now has varying widths at each step (instead of fixed λ width)—Figure 4 illustrate this idea.

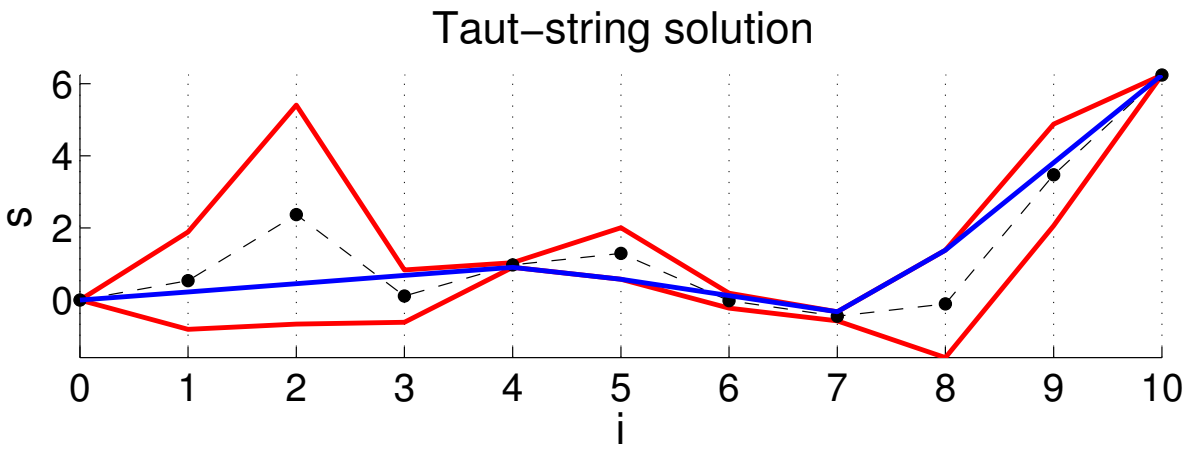

Figure 4: Example of the weighted taut string method with $\boldsymbol{w} = (1.35, 3.03, 0.73, 0.06, 0.71, 0.20, 0.12, 1.49, 1.41)$. The cumulative sum $\boldsymbol{r}$ of the input signal values $\boldsymbol{y}$ is shown as the dashed line, with the black dots marking the points $(i, \boldsymbol{r}_i)$. The bottom and ceiling of the tube are shown in red, which vary in width at each step following the weights $\boldsymbol{w}_i$. The weighted taut string solution $\boldsymbol{s}$ is shown as a blue line.

As a consequence of the above derivation and intuition, we ultimately obtain a weighted taut-string algorithm that can handle varying tube width by suitably modifying Algorithm 1. In particular, when checking ceiling/floor violations as well as when checking slope recomputations and restarts, we must account for varying tube heights. Algorithm 2 presents the precise modifications that we must make to Algorithm 1 to handle weights.

Algorithm 2 Modified lines for weighted version of Algorithm 1

3: Find tube height: $\tilde{\lambda} = w_{i+1}$ if $i < n-1$, else $\tilde{\lambda} = 0$
8: Start new segment after break: $(i_0, \bar{i}) = \underline{i}$, $i = \underline{i} + 1$, $\bar{h} = \underline{h} = -w_i$, $\bar{\delta} = \infty$, $\underline{\delta} = -\infty$
15: Start new segment after break: $(i_0, \underline{i}) = \bar{i}$, $i = \bar{i} + 1$, $\bar{h} = \underline{h} = w_i$, $\bar{\delta} = \infty$, $\underline{\delta} = -\infty$

2.1.3 Projected-newton for weighted $\mathbf{Tv}_1^{\mathbf{1D}}$

In this section we present details of a projected-Newton (PN) approach to solving the weighted-TV problem (2.8). Although, our optimized taut-string approach is empirically superior to our PN approach, as mentioned before we still present its details. These details prove useful when developing subroutines for handling ℓ_p-norm TV prox-operators, but perhaps their greatest use lies in presenting a general method that could be applied to other problems that have structures similar to TV, e.g., group total-variation [Alaız et al., 2013, Wytock et al., 2014] and ℓ_1-trend filtering [Kim et al., 2009, Tibshirani, 2014].

The weighted-TV dual problem (2.9) is a bound-constrained QP, so it could be solved using a variety of methods such as TRON [Lin and Moré, 1999], L-BFGS-B [Byrd et al., 1994], or projected-Newton

(PN) [Bertsekas, 1982]. Obviously, these methods will be inefficient if invoked off-the-shelf; exploitation of problem structure is a must for solving (2.9) efficiently. PN lends itself well to such structure exploitation; we describe the details below.

PN runs iteratively in three key steps: first it identifies a special subset of *active variables* and uses these to compute a *reduced* Hessian. Then, it uses this Hessian to scale the gradient and move in the direction opposite to it, damping with a stepsize, if needed. Finally, the next iterate is obtained by projecting onto the constraints, and the cycle repeats. PN can be regarded as an extension of the gradient-projection method (GP, Bertsekas [1999]), where the components of the gradient that make the updating direction infeasible are removed; in PN both the gradient and the Hessian are *reduced* to guarantee this feasibility.

At each iteration PN selects the active variables

$$I := \{i \mid (u_i = -w_i \text{ and } [\nabla\phi(\boldsymbol{u})]_i > \epsilon) \quad \text{or} \quad (u_i = w_i \text{ and } [\nabla\phi(\boldsymbol{u})]_i < -\epsilon)\}\,, \tag{2.11}$$

where $\epsilon \geq 0$ is small scalar. This corresponds to the set of variables at a bound, and for which the gradient points inside the feasible region; that is, for these variables to further improve the objective function we would have to step out of bounds. It is thus clear that these variables are of no use for this iteration, so we define the complementary set $\bar{I} := \{1 \dots n\} \setminus I$ of indices not in I, which are the variables we are interested in updating. From the Hessian $\boldsymbol{H} = \nabla^2\phi(u)$ we extract the *reduced Hessian* $\boldsymbol{H}_{\bar{I}}$ by selecting rows and columns indexed by $\bar{I}$, and in a similar way the *reduce gradient* $[\nabla\phi(\boldsymbol{u})]_{\bar{I}}$. Using these we perform a Newton–like "reduced" update in the form

$$\boldsymbol{u}_{\bar{I}} \leftarrow P(\boldsymbol{u}_{\bar{I}} - \alpha \boldsymbol{H}_{\bar{I}}^{-1}[\nabla\phi(\boldsymbol{u})]_{\bar{I}}), \tag{2.12}$$

where α is a stepsize, and P denotes projection onto the constraints, which for box–constraints reduces to simple element–wise projection. Note that only the variables in the set $\bar{I}$ are updated in this iterate, leaving the rest unchanged. While such update requires computing the inverse of the reduced Hessian $\boldsymbol{H}_{\bar{I}}$, which in the general case can amount to computational costs in the $O(n^3)$ order, we will see now how exploiting the structure of the problem allows us to perform all the steps above efficiently.

First, observe that for (2.9) the Hessian is

$$\boldsymbol{H} = \boldsymbol{D}\boldsymbol{D}^T = \begin{pmatrix} 2 & -1 & & & \\ -1 & 2 & -1 & & \\ & -1 & 2 & \ddots & \\ & & \ddots & \ddots & -1 \\ & & & -1 & 2 \end{pmatrix} \in \mathbb{R}^{(n-1)\times(n-1)}.$$

Next, observe that whatever the active set I, the corresponding reduced Hessian $\boldsymbol{H}_{\bar{I}}$ remains symmetric tridiagonal. This observation is crucial because then we can quickly compute the updating direction $\boldsymbol{d}_{\bar{I}} = \boldsymbol{H}_{\bar{I}}^{-1}[\nabla\phi(\boldsymbol{u})]_{\bar{I}}$, which can be done by solving the linear system $\boldsymbol{H}_{\bar{I}}\boldsymbol{d}_{\bar{I}} = [\nabla\phi(\boldsymbol{u}^t)]_{\bar{I}}$ as follows:

1. Compute the Cholesky decomposition $\boldsymbol{H}_{\bar{I}} = \boldsymbol{R}^T\boldsymbol{R}$.
2. Solve the linear system $\boldsymbol{R}^T\boldsymbol{v} = [\nabla\phi(\boldsymbol{u})]_{\bar{I}}$ to obtain $\boldsymbol{v}$.
3. Solve the linear system $\boldsymbol{R}\boldsymbol{d}_{\bar{I}} = \boldsymbol{v}$ to obtain $\boldsymbol{d}_{\bar{I}}$.

Because the reduced Hessian is also tridiagonal, its Cholesky decomposition can be computed in *linear time* to yield a bidiagonal matrix $\boldsymbol{R}$, which in turn allows to solve the subsequent linear systems also in linear time. Extremely efficient routines to perform all these tasks are available in the LAPACK libraries [Anderson et al., 1999].

Algorithm 3 Stepsize selection for Projected Newton

Initialize: $\alpha_0 = 1$, $k = 0$, $\boldsymbol{d}$, tolerance parameter σ
while $\phi(\boldsymbol{u}) - \phi(P[\boldsymbol{u} - \alpha_k \boldsymbol{d}]) < \sigma \cdot \alpha_k \cdot (\nabla\phi(\boldsymbol{u}) \cdot \boldsymbol{d})$ **do**
  Minimize quadratic model: $\alpha_{k+1} = -\frac{\alpha^2 \|\nabla\phi(\boldsymbol{u})\|_2^2}{2(-a - \alpha\|\nabla\phi(\boldsymbol{u})\|_2^2)}$.
  if $\alpha_{k+1} > \alpha_k$ **or** $\alpha_{k+1} \simeq \alpha_k$, **then** $\alpha_{k+1} = \frac{1}{2}\alpha_k$.
  $k \leftarrow k + 1$
end while
return α_k

The next crucial ingredient is efficient selection of the stepsize α. The original PN algorithm Bertsekas [1982] recommends Armijo-search along projection arc. However, for our problem this search is inordinately expensive. So we resort to a backtracking strategy using quadratic interpolation [Nocedal and Wright, 2000], which works admirably well. This strategy is as follows: start with an initial stepsize $\alpha_0 = 1$. If the current stepsize α_k does not provide sufficient decrease in ϕ, build a quadratic model using $\phi(\boldsymbol{u})$, $\phi(\boldsymbol{u} - \alpha_k \boldsymbol{d})$, and $\partial_\alpha \phi(\boldsymbol{u} - \alpha_k \boldsymbol{d})$. Then, the stepsize α_{k+1} is set to the value that minimizes this quadratic model. In the event that at some point of the procedure the new α_{k+1} is larger than or too similar to α_k, its value is halved. In this fashion, quadratic approximations of ϕ are iterated until a good enough α is found. The goodness of a stepsize is measured using the following Armijo-like sufficient descent rule

$$\phi(\boldsymbol{u}) - \phi(P\left[\boldsymbol{u} - \alpha_k \boldsymbol{d}\right]) \geq \sigma \cdot \alpha_k \cdot (\nabla\phi(\boldsymbol{u}) \cdot \boldsymbol{d}),$$

where a tolerance $\sigma = 0.05$ works well practice.

Note that the gradient $\nabla\phi(\boldsymbol{u})$ might be misleading in the condition above if $\boldsymbol{u}$ has components at the boundary and $\boldsymbol{d}$ points outside this boundary (because then, due to the subsequent projection no real improvement would be obtained by stepping outside the feasible region). To address this concern, we modify the computation of the gradient $\nabla\phi(\boldsymbol{u})$, zeroing our the entries that relate to direction components pointing outside the feasible set.

The whole stepsize selection procedure is shown in Algorithm 3. The costliest operation in this procedure is the evaluation of ϕ, which, nevertheless can be done in linear time. Furthermore, in practice a few iterations more than suffice to obtain a good stepsize.

Overall, a full PN iteration as described above runs at $O(n)$ cost. Thus, by exploiting the structure of the problem, we manage to reduce the $O(n^3)$ cost per iteration of a general PN algorithm to a linear-cost method. The pseudocode of the resulting method is shown as Algorithm 4. Note that in the special case when the weights $\boldsymbol{W} := \mathrm{Diag}(w_i)$ are so large that the unconstrained optimum coincides with the constrained one, we can obtain $\boldsymbol{u}^*$ directly via solving $\boldsymbol{D}\boldsymbol{D}^T\boldsymbol{W}\boldsymbol{u}^* = \boldsymbol{D}\boldsymbol{y}$ (which can also be done at $O(n)$ cost). The duality gap of the current solution (see formula 2.3) is used as a stopping criterion, where we use a tolerance of $\epsilon = 10^{-5}$ in practice.

2.2 TV-L2: Proximity for $\mathrm{Tv}_2^{\mathbf{1D}}$

For TV-L2 proximity ($p = 2$) the dual (2.2) reduces to

$$\min_{\boldsymbol{u}} \ \phi(\boldsymbol{u}) := \tfrac{1}{2}\|\boldsymbol{D}^T\boldsymbol{u}\|_2^2 - \boldsymbol{u}^T\boldsymbol{D}\boldsymbol{y}, \quad \text{s.t. } \|\boldsymbol{u}\|_2 \leq \lambda. \tag{2.13}$$

Problem (2.13) is nothing but a version of the well-known trust-region subproblem (TRS), for which a variety of numerical approaches are known [Conn et al., 2000].

We derive a specialized algorithm based on the classic Moré-Sorensen Newton (MSN) method [Moré and Sorensen, 1983]. This method in general can be quite expensive, but again we can exploit the tridiagonal Hessian to make it efficient. Curiously, experiments show that for a limited range of λ values,

Algorithm 4 PN algorithm for TV-L1-proximity

Let $\boldsymbol{W} = \mathrm{Diag}(w_i)$; solve $\boldsymbol{D}\boldsymbol{D}^T\boldsymbol{W}\boldsymbol{u}^* = \boldsymbol{D}\boldsymbol{y}$.
if $\|\boldsymbol{W}^{-1}\boldsymbol{u}^*\|_\infty \leq 1$, **return** $\boldsymbol{u}^*$.
$\boldsymbol{u}^0 = P[\boldsymbol{u}^*]$, $t = 0$.
while gap$(\boldsymbol{u}) > \epsilon$ **do**
  Identify set of active constraints I; let $\bar{I} = \{1 \dots n\} \setminus I$.
  Construct reduced Hessian $\boldsymbol{H}_{\bar{I}}$.
  Solve $\boldsymbol{H}_{\bar{I}}\boldsymbol{d}_{\bar{I}} = [\nabla\phi(\boldsymbol{u}^t)]_{\bar{I}}$.
  Compute stepsize α using backtracking + interpolation (Alg. 3).
  Update $\boldsymbol{u}_{\bar{I}}^{t+1} = P[\boldsymbol{u}_{\bar{I}}^t - \alpha\boldsymbol{d}_{\bar{I}}]$.
  $t \leftarrow t + 1$.
end while
return $\boldsymbol{u}^t$.

even ordinary gradient-projection (GP) can be competitive. Thus for overall best performance, one may prefer a hybrid MSN-GP approach.

Towards solving (2.13), consider its KKT conditions:

$$\begin{aligned} &(\boldsymbol{D}\boldsymbol{D}^T + \alpha\boldsymbol{I})\boldsymbol{u} = \boldsymbol{D}\boldsymbol{y}, \\ &\alpha(\|\boldsymbol{u}\|_2 - \lambda) = 0, \quad \alpha \geq 0, \end{aligned} \tag{2.14}$$

where α is a Lagrange multiplier. There are two possible cases regarding the $\|\boldsymbol{u}\|_2 \leq \lambda$: either $\|\boldsymbol{u}\|_2 < \lambda$, or $\|\boldsymbol{u}\|_2 = \lambda$.

If $\|\boldsymbol{u}\|_2 < \lambda$, then the KKT condition $\alpha(\|\boldsymbol{u}\|_2 - \lambda) = 0$, implies that $\alpha = 0$ must hold and $\boldsymbol{u}$ can be obtained immediately by solving the linear system $\boldsymbol{D}\boldsymbol{D}^T\boldsymbol{u} = \boldsymbol{D}\boldsymbol{y}$. This can be done in $O(n)$ time owing to the bidiagonal structure of $\boldsymbol{D}$. Conversely, if the solution to $\boldsymbol{D}\boldsymbol{D}^T\boldsymbol{u} = \boldsymbol{D}\boldsymbol{y}$ lies in the interior of the $\|\boldsymbol{u}\|_2 \leq 1$, then it solves (2.14). Therefore, this case is trivial to solve, and we need to consider only the harder case $\|\boldsymbol{u}\|_2 = \lambda$.

For any given α one can obtain the corresponding vector $\boldsymbol{u}$ as $\boldsymbol{u}(\alpha) = (\boldsymbol{D}\boldsymbol{D}^T + \alpha\boldsymbol{I})^{-1}\boldsymbol{D}\boldsymbol{y}$. Therefore, optimizing for $\boldsymbol{u}$ reduces to the problem of finding the "true" value of α.

An obvious approach is to solve $\|\boldsymbol{u}(\alpha)\|_2^2 = \lambda^2$. Less obvious is the *MSN equation*

$$h(\alpha) := \lambda^{-1} - \|\boldsymbol{u}(\alpha)\|_2^{-1} = 0, \tag{2.15}$$

which has the benefit of being almost linear in the search interval, which results in fast convergence [Moré and Sorensen, 1983]. Thus, the task is to find the root of the function $h(\alpha)$, for which we use Newton's method, which in this case leads to the iteration

$$\alpha \leftarrow \alpha - h(\alpha)/h'(\alpha). \tag{2.16}$$

Some calculation shows that the derivative h' can be computed as

$$\frac{1}{h'(\alpha)} = \frac{\|\boldsymbol{u}(\alpha)\|_2^3}{\boldsymbol{u}(\alpha)^T(\boldsymbol{D}\boldsymbol{D}^T + \alpha\boldsymbol{I})^{-1}\boldsymbol{u}(\alpha)}. \tag{2.17}$$

The key idea in MSN is to eliminate the matrix inverse in (2.17) by using the Cholesky decomposition $\boldsymbol{D}\boldsymbol{D}^T + \alpha\boldsymbol{I} = \boldsymbol{R}^T\boldsymbol{R}$ and defining a vector $\boldsymbol{q} = (\boldsymbol{R}^T)^{-1}\boldsymbol{u}$, so that $\|\boldsymbol{q}\|_2^2 = \boldsymbol{u}(\alpha)^T(\boldsymbol{D}\boldsymbol{D}^T + \alpha\boldsymbol{I})^{-1}\boldsymbol{u}(\alpha)$. As a result, the Newton iteration (2.16) becomes

Algorithm 5 MSN based TV-L2 proximity

Initialize: $\alpha^0 = 0$, $t = 0$, $\boldsymbol{u} = 0$.
while $\left|\|\boldsymbol{u}\|_2^2 - \lambda\right| > \epsilon_\lambda$ **or** $\text{gap}(\boldsymbol{u}) > \epsilon_{\text{gap}}$ **do**
  Compute Cholesky decomp. $\boldsymbol{D}\boldsymbol{D}^T + \alpha^t \boldsymbol{I} = \boldsymbol{R}^T\boldsymbol{R}$.
  Obtain $\boldsymbol{u}$ by solving $\boldsymbol{R}^T\boldsymbol{R}\boldsymbol{u} = \boldsymbol{D}\boldsymbol{y}$.
  Obtain $\boldsymbol{q}$ by solving $\boldsymbol{R}^T\boldsymbol{q} = \boldsymbol{u}$.
  $\alpha^{t+1} = \alpha^t + \alpha - \frac{\|\boldsymbol{u}(\alpha)\|_2^2}{\|\boldsymbol{q}\|_2^2}\left(1 - \frac{\|\boldsymbol{u}(\alpha)\|_2}{\lambda}\right)$.
  $t \leftarrow t + 1$.
end while
return $\boldsymbol{u}^t$

$$\begin{aligned}
\alpha - \frac{h(\alpha)}{h'(\alpha)} &= \alpha - (\|\boldsymbol{u}(\alpha)\|_2^{-1} - \lambda^{-1}) \cdot \frac{\|\boldsymbol{u}(\alpha)\|_2^3}{\boldsymbol{u}(\alpha)^T(\boldsymbol{D}\boldsymbol{D}^T + \alpha\boldsymbol{I})^{-1}\boldsymbol{u}(\alpha)}, \\
&= \alpha - \frac{\|\boldsymbol{u}(\alpha)\|_2^2 - \lambda^{-1}\|\boldsymbol{u}(\alpha)\|_2^3}{\|\boldsymbol{q}\|_2^2}, \\
&= \alpha - \frac{\|\boldsymbol{u}(\alpha)\|_2^2}{\|\boldsymbol{q}\|_2^2}\left(1 - \frac{\|\boldsymbol{u}(\alpha)\|_2}{\lambda}\right),
\end{aligned}$$

and therefore

$$\alpha \quad \leftarrow \quad \alpha - \frac{\|\boldsymbol{u}(\alpha)\|_2^2}{\|\boldsymbol{q}\|_2^2}\left(1 - \frac{\|\boldsymbol{u}(\alpha)\|_2}{\lambda}\right). \tag{2.18}$$

As in TV-L_1, the tridiagonal structure of $(\boldsymbol{D}\boldsymbol{D}^T + \alpha\boldsymbol{I})$ allows to compute both $\boldsymbol{R}$ and $\boldsymbol{q}$ in linear time, so the overall iteration runs in $O(n)$ time.

The above ideas are presented as pseudocode in Algorithm 5. As a stopping criterion two conditions are checked: whether the duality gap is small enough, and whether $\boldsymbol{u}$ is close enough to the boundary. This latter check is useful because intermediate solutions could be dual-infeasible, thus making the duality gap an inadequate optimality measure on its own. In practice we use tolerance values $\epsilon_\lambda = 10^{-6}$ and $\epsilon_{\text{gap}} = 10^{-5}$.

Even though Algorithm 5 requires only linear time per iteration, it is fairly sophisticated, and in fact a much simpler method can be devised. This is illustrated here by a gradient-projection method with a *fixed* stepsize α_0, whose iteration is

$$\boldsymbol{u}^{t+1} = P_{\|\cdot\|_2 \le \lambda}(\boldsymbol{u}^t - \alpha_0 \nabla\phi(\boldsymbol{u}^t)). \tag{2.19}$$

The theoretically ideal choice for the stepsize α_0 is given by the inverse of the Lipschitz constant L of the gradient $\nabla\phi(\boldsymbol{u})$ [Nesterov, 2007, Beck and Teboulle, 2009]. Since $\phi(\boldsymbol{u})$ is a convex quadratic, L is simply the largest eigenvalue of the Hessian $\boldsymbol{D}\boldsymbol{D}^T$. Owing to its special structure, the eigenvalues of the Hessian have closed-form expressions, namely $\lambda_i = 2 - 2\cos\left(\frac{i\pi}{n+1}\right)$ (for $1 \le i \le n$). The largest one is $\lambda_n = 2 - 2\cos\left(\frac{(n-1)\pi}{n}\right)$, which tends to 4 as $n \to \infty$; thus the choice $\alpha_0 = 1/4$ is a good approximation. Pseudocode showing the whole procedure is presented in Algorithm 6. Combining this with the fact that the the projection $P_{\|\cdot\|_2 \le \lambda}$ is also trivial to compute, the GP iteration (2.19) turns out to be very attractive. Indeed, sometimes it can even outperform the more sophisticated MSN method, though only for a very limited range of λ values. Therefore, in practice we recommend a hybrid of GP and MSN, as suggested by our experiments.

Algorithm 6 GP algorithm for TV-L_2 proximity

Initialize $\boldsymbol{u}^0 \in \mathbb{R}^N$, $t = 0$.
while ($\neg$ converged) **do**
  Gradient update: $\boldsymbol{v}^t = \boldsymbol{u}^t - \frac{1}{4}\nabla f(\boldsymbol{u}^t)$.
  Projection: $\boldsymbol{u}^{t+1} = \max(1 - \lambda/\|\boldsymbol{v}^t\|_2, 0) \cdot \boldsymbol{v}^t$.
  $t \leftarrow t + 1$.
end while
return $\boldsymbol{u}^t$.

2.3 TV-Lp: Proximity for Tv_p^{1D}

For TV-L_p proximity (for $1 < p < \infty$) the dual (2.2) problem becomes

$$\min_{\boldsymbol{u}} \ \phi(\boldsymbol{u}) := \tfrac{1}{2}\|\boldsymbol{D}^T\boldsymbol{u}\|_2^2 - \boldsymbol{u}^T\boldsymbol{D}\boldsymbol{y}, \quad \text{s.t. } \|\boldsymbol{u}\|_q \leq \lambda, \tag{2.20}$$

where $q = 1/(1 - 1/p)$. Problem (2.20) is not particularly amenable to the Newton-type approaches taken above, as neither PN, nor MSN-type methods can be applied easily. It is somewhat amenable to a gradient-projection (GP) strategy, for which the same update rule as in (2.19) applies, but unlike the $q = 2$ case, the projection step here is much more involved. Thus, to complement GP, we also propose an alternative strategy using the projection-free Frank-Wolfe (FW) method. As expected, the overall best performing approach is actually a hybrid of GP and FW. Let us thus present details of both below.

2.3.1 Efficient projection onto the ℓ_q-ball

The problem of projecting onto the ℓ_q-norm ball is

$$\min_{\boldsymbol{w}} \quad d(\boldsymbol{w}) := \tfrac{1}{2}\|\boldsymbol{w} - \boldsymbol{u}\|_2^2, \quad \text{s.t. } \|\boldsymbol{w}\|_q \leq \lambda. \tag{2.21}$$

For this problem, it turns out to be more convenient to address its Fenchel dual

$$\min_{\boldsymbol{w}} \quad d^*(\boldsymbol{w}) := \tfrac{1}{2}\|\boldsymbol{w} - \boldsymbol{u}\|_2^2 + \lambda\|\boldsymbol{w}\|_p, \tag{2.22}$$

which is actually nothing but $\mathrm{prox}_{\lambda\|\cdot\|_p}(\boldsymbol{u})$. The optimal solution, say $\boldsymbol{w}^*$, to (2.21) can be obtained by solving (2.22), by using the Moreau-decomposition (A.6) which yields

$$\boldsymbol{w}^* = \boldsymbol{u} - \mathrm{prox}_{\lambda\|\cdot\|_p}(\boldsymbol{u}).$$

Projection (2.21) is computed many times within GP, so it is crucial to solve it rapidly and accurately. To this end, we first turn (2.22) into a differentiable problem and then derive a projected-Newton method following our approach of §2.1.

Assume therefore, without loss of generality that $\boldsymbol{u} \geq 0$, so that $\boldsymbol{w} \geq 0$ also holds (the signs can be restored after solving this problem). Thus, instead of (2.22), we solve

$$\min_{\boldsymbol{w}} \quad d^*(\boldsymbol{w}) := \tfrac{1}{2}\|\boldsymbol{w} - \boldsymbol{u}\|_2^2 + \lambda\big(\textstyle\sum_i w_i^p\big)^{1/p} \quad \text{s.t. } \boldsymbol{w} \geq 0. \tag{2.23}$$

The gradient of d^* may be compactly written as

$$\nabla d^*(\boldsymbol{w}) = \boldsymbol{w} - \boldsymbol{u} + \lambda\|\boldsymbol{w}\|_p^{1-p}\boldsymbol{w}^{p-1}, \tag{2.24}$$

where $\boldsymbol{w}^{p-1}$ denotes elementwise exponentiation of $\boldsymbol{w}$. Elementary calculation yields

$$\begin{aligned}\tfrac{\partial^2}{\partial w_i \partial w_j} d^*(\boldsymbol{w}) &= \delta_{ij}\big(1 + \lambda(p-1)\big(\tfrac{w_i}{\|w\|_p}\big)^{p-2}\|\boldsymbol{w}\|_p^{-1}\big) + \lambda(1-p)\big(\tfrac{w_i}{\|w\|_p}\big)^{p-1}\big(\tfrac{w_j}{\|w\|_p}\big)^{p-1}\|\boldsymbol{w}\|_p^{-1} \\ &= \delta_{ij}\big(1 - c\hat{\boldsymbol{w}}_i^{p-2}\big) + c\bar{\boldsymbol{w}}_i\bar{\boldsymbol{w}}_j,\end{aligned}$$

where $c := \lambda(1-p)\|\boldsymbol{w}\|_p^{-1}$, $\hat{\boldsymbol{w}} := \boldsymbol{w}/\|\boldsymbol{w}\|_p$, $\bar{\boldsymbol{w}} := (\boldsymbol{w}/\|\boldsymbol{w}\|_p)^{p-1}$, and δ_{ij} is the Dirac delta. In matrix notation, this Hessian's diagonal plus rank-1 structure becomes apparent

$$\boldsymbol{H}(\boldsymbol{w}) = \operatorname{Diag}\big(1 - c\hat{\boldsymbol{w}}^{p-2}\big) + c\bar{\boldsymbol{w}} \cdot \bar{\boldsymbol{w}}^T \tag{2.25}$$

To develop an efficient Newton method it is imperative to exploit this structure. It is not hard to see that for a set of non-active variables $\bar{I}$ the reduced Hessian takes the form

$$\boldsymbol{H}_{\bar{I}}(\boldsymbol{w}) = \operatorname{Diag}\big(\mathbf{1} - c\hat{\boldsymbol{w}}_{\bar{I}}^{p-2}\big) + c\bar{\boldsymbol{w}}_{\bar{I}}\bar{\boldsymbol{w}}_{\bar{I}}^T. \tag{2.26}$$

With the shorthand $\Delta = \operatorname{Diag}\big(\mathbf{1} - c\hat{\boldsymbol{w}}_{\bar{I}}^{p-2}\big)$, the matrix-inversion lemma yields

$$\boldsymbol{H}_{\bar{I}}^{-1}(\boldsymbol{w}) = \big(\Delta + c\bar{\boldsymbol{w}}_{\bar{I}}\bar{\boldsymbol{w}}_{\bar{I}}^T\big)^{-1} = \Delta^{-1} - \frac{\Delta^{-1}c\bar{\boldsymbol{w}}_{\bar{I}}\bar{\boldsymbol{w}}_{\bar{I}}^T\Delta^{-1}}{1 + c\bar{\boldsymbol{w}}_{\bar{I}}^T\Delta^{-1}\bar{\boldsymbol{w}}_{\bar{I}}}. \tag{2.27}$$

Furthermore, since in PN the inverse of the reduced Hessian always operates on the reduced gradient, we can rearrange the terms in this operation for further efficiency; that is,

$$\boldsymbol{H}_{\bar{I}}(\boldsymbol{w})^{-1}\nabla_{\bar{I}}f(\boldsymbol{w}) = \boldsymbol{v} \odot \nabla_{\bar{I}}f(\boldsymbol{w}) - \frac{\big(\boldsymbol{v} \odot \bar{\boldsymbol{w}}_{\bar{I}}\big)\big(\boldsymbol{v} \odot \bar{\boldsymbol{w}}_{\bar{I}}\big)^T\nabla_{\bar{I}}f(\boldsymbol{w})}{1/c + \bar{\boldsymbol{w}}_{\bar{I}}\big(\boldsymbol{v} \odot \bar{\boldsymbol{w}}_{\bar{I}}\big)}, \tag{2.28}$$

where $\boldsymbol{v} := \big(\mathbf{1} - c\hat{\boldsymbol{w}}_{\bar{I}}^{p-2}\big)^{-1}$, and $\odot$ denotes componentwise product.

The relevant point of the above derivations is that the Newton direction, and thus the overall PN iteration can be computed in $O(n)$ time, which results in a highly effective solver.

2.3.2 Frank-Wolf algorithm for TV ℓ_p proximity

The Frank-Wolfe (FW) algorithm (see e.g., [Jaggi, 2013] for a recent overview), also known as the conditional gradient method [Bertsekas, 1999] solves differentiable optimization problems over compact convex sets, and can be quite effective if we have access to a subroutine to solve linear problems over the constraint set.

The generic FW iteration is illustrated in Algorithm 7. FW offers an attractive strategy for TV ℓ_p proximity because both the descent-direction as well as stepsizes can be computed very easily. Specifically, to find the descent direction we need to solve

$$\min_{\boldsymbol{s}} \quad \boldsymbol{s}^T\left(\boldsymbol{D}\boldsymbol{D}^T\boldsymbol{u} - \boldsymbol{D}\boldsymbol{y}\right), \quad \text{s.t.} \quad \|\boldsymbol{s}\|_q \leq \lambda. \tag{2.29}$$

This problem can be solved by observing that $\max_{\|\boldsymbol{s}\|_q \leq 1} \boldsymbol{s}^T\boldsymbol{z}$ is attained by some vector $\boldsymbol{s}$ proportional to $\boldsymbol{z}$, of the form $|\boldsymbol{s}^*| \propto |\boldsymbol{z}|^{p-1}$. Therefore, $\boldsymbol{s}^*$ in (2.29) is found by taking $\boldsymbol{z} = \boldsymbol{D}\boldsymbol{D}^T\boldsymbol{u} - \boldsymbol{D}\boldsymbol{y}$, computing $\boldsymbol{s} = -\operatorname{sgn}(\boldsymbol{z}) \odot |\boldsymbol{z}|^{p-1}$ and then rescaling $\boldsymbol{s}$ to meet $\|\boldsymbol{s}\|_q = \lambda$.

The stepsize can also be computed in closed form owing as the objective function is quadratic. Note the update in FW takes the form $\boldsymbol{u} + \gamma(\boldsymbol{s} - \boldsymbol{u})$, which can be rewritten as $\boldsymbol{u} + \gamma\boldsymbol{d}$ with $\boldsymbol{d} = \boldsymbol{s} - \boldsymbol{u}$. Using this notation the optimal stepsize is obtained by solving

$$\min_{\gamma \in [0,1]} \tfrac{1}{2}\|\boldsymbol{D}^T(\boldsymbol{u} + \gamma\boldsymbol{d})\|_2^2 - (\boldsymbol{u} + \gamma\boldsymbol{d})^T\boldsymbol{D}\boldsymbol{y}.$$

A brief calculation on the above problem yields

$$\gamma^* = \min\left\{\max\left\{\hat{\gamma}, 1\right\}, 0\right\},$$

where $\hat{\gamma} = -(\boldsymbol{d}^T\boldsymbol{D}\boldsymbol{D}^T\boldsymbol{u} + \boldsymbol{d}^T\boldsymbol{D}\boldsymbol{y})/(\boldsymbol{d}^T\boldsymbol{D}\boldsymbol{D}^T\boldsymbol{d})$ is the unconstrained optimal stepsize. We note that following [Jaggi, 2013] we also check a "surrogate duality-gap"

$$g(\boldsymbol{x}) = \boldsymbol{x}^T\nabla f(\boldsymbol{x}) - \min_{\boldsymbol{s} \in \mathcal{D}} \boldsymbol{s}^T\nabla f(\boldsymbol{x}) = (\boldsymbol{x} - \boldsymbol{s}^*)^T\nabla f(\boldsymbol{x}),$$

at the end of each iteration. If this gap is smaller than the desired tolerance, the real duality gap is computed and checked; if it also meets the tolerance, the algorithm stops.

Algorithm 7 Frank-Wolfe (FW)

Inputs: f, compact convex set $\mathcal{D}$.
Initialize $\boldsymbol{x}_0 \in \mathcal{D}$, $t = 0$.
while stopping criteria not met **do**
  Find descent direction: $\min_{\boldsymbol{s}} \boldsymbol{s} \cdot \nabla f(\boldsymbol{x}_t)$ s.t. $\boldsymbol{s} \in \mathcal{D}$.
  Determine stepsize: $\min_{\gamma} f(\boldsymbol{x}_t + \gamma(\boldsymbol{s} - \boldsymbol{x}_t))$ s.t. $\gamma \in [0, 1]$.
  Update: $\boldsymbol{x}_{t+1} = \boldsymbol{x}_t + \gamma(\boldsymbol{s} - \boldsymbol{x}_t)$
  $t \leftarrow t + 1$.
end while
return $\boldsymbol{x}_t$.

2.4 Prox operator for TV-L$_\infty$

The final case is $\text{Tv}_\infty^{\text{1D}}$. We mention this case only for completeness, but do not spend much time in developing tuned methods.. The dual (2.2) here becomes

$$\min_{\boldsymbol{u}} \quad \tfrac{1}{2}\|\boldsymbol{D}^T\boldsymbol{u}\|_2^2 - \boldsymbol{u}^T\boldsymbol{D}\boldsymbol{y}, \quad \text{s.t. } \|\boldsymbol{u}\|_1 \leq \lambda. \tag{2.30}$$

This problem can be again easily solved by invoking GP, where the only non-trivial step is projection onto the ℓ_1-ball. But the latter is an extremely well-studied operation (see e.g., [Liu and Ye, 2009, Kiwiel, 2008]), and so $O(n)$ time routines for this purpose are readily available. By integrating them in our GP framework an efficient prox solver is obtained.

3 Prox operators for multidimensional TV

This section shows how to build on our efficient 1D-TV prox operators to handle proximity for the much harder multidimensional TV (1.3). To that end, we follow classical proximal optimization techniques [Combettes and Pesquet, 2009, Bauschke and Combettes, 2011].

3.1 Proximity stacking

The basic composite objective (1.1) is a special case of the more general class of models where one may have several regularizers, so that we now solve

$$\min_{\boldsymbol{x}} \quad f(\boldsymbol{x}) + \sum\nolimits_{i=1}^{m} r_i(\boldsymbol{x}), \tag{3.1}$$

where each r_i (for $1 \leq i \leq m$) is lsc and convex.

Just like the basic problem (1.1), the more complex problem (3.1) can also be tackled via proximal methods. The key to doing so is to use *inexact proximal methods* along with a technique that we call **proximity stacking**. Inexact proximal methods allow one to use approximately computed prox operators without impeding overall convergence, while proximity stacking allows one to compute the prox operator for the entire sum $r(\boldsymbol{x}) = \sum_{i=1}^{m} r_i(\boldsymbol{x})$ by "stacking" the individual r_i prox operators. This stacking leads to a highly modular design; see Figure 5 for a visualization. In other words, proximity stacking involves computing the prox operator

$$\text{prox}_r(\boldsymbol{y}) := \operatorname*{argmin}_{\boldsymbol{x}} \quad \tfrac{1}{2}\|\boldsymbol{x} - \boldsymbol{y}\|_2^2 + \sum\nolimits_{i=1}^{m} r_i(\boldsymbol{x}), \tag{3.2}$$

by iteratively invoking the individual prox operators prox_{r_i} and then combining their outputs. This mixing is done by means of a combiner method, which guarantees convergence to the solution of the overall $\text{prox}_r(\boldsymbol{y})$.

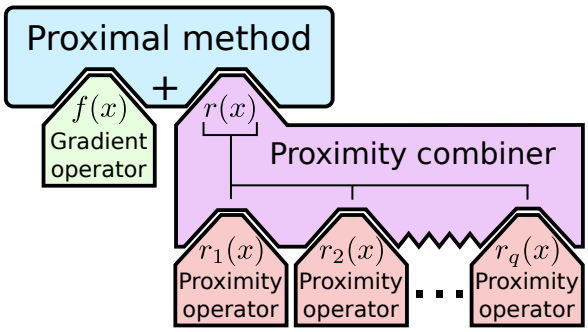

Figure 5: Design schema in proximal optimization for minimizing the function $f(\boldsymbol{x}) + \sum_{i=1}^{m} r_i(\boldsymbol{x})$. Proximal stacking makes the sum of regularizers appear as a single one to the proximal method, while retaining modularity in the design of each proximity step through the use of a combiner method. For non-smooth f the same schema applies by just replacing the f gradient operator by its corresponding proximity operator.

Different proximal combiners can used for computing prox_r (3.2). For instance, for $m = 2$, the Proximal Dykstra (PD) [Combettes and Pesquet, 2009] method is a reasonable choice; alternatively, as shown recently in [Jegelka et al., 2013], the Douglas-Rachford (DR) scheme proves to be a more effective choice. The crux of both PD and DR, however lies in that they require only subroutines to compute the individual prox operators prox_{r_1} and prox_{r_2}, which allows us to reuse our 1D-TV subroutines.

More generally, if more than two regularizers are present (i.e., $m > 2$), then a it is easier to use *Parallel-Proximal Dykstra* (PPD) [Combettes, 2009] or *Parallel Douglas-Rachford* (PDR) as the proximal combiners—both methods being generalizations obtained via the "product-space trick" of Pierra [1984].

These parallel proximal methods are attractive because they not only combine an arbitrary number of regularizers, but also allows parallelizing the calls to the individual prox operators. This feature allows us to develop a highly parallel implementation for multidimensional TV proximity (§3.3).

Thus, using proximal stacking and combination, any convex machine learning problem with multiple regularizers can be solved in a highly modular proximal framework. Below we exemplify these ideas by applying them to two- and higher-dimensional TV proximity, which we then use within proximal solvers for addressing a wide array of applications.

3.2 Two-dimensional TV

Recall that for a matrix $\boldsymbol{X} \in \mathbb{R}^{n_1 \times n_2}$, our anisotropic 2D-TV regularizer takes the form

$$\text{Tv}^2_{p,q}(\boldsymbol{X}) := \sum\nolimits_{i=1}^{n_1} \Big(\sum\nolimits_{j=1}^{n_2-1} |x_{i,j+1} - x_{i,j}|^p \Big)^{1/p} + \sum\nolimits_{j=1}^{n_2} \Big(\sum\nolimits_{i=1}^{n_1-1} |x_{i+1,j} - x_{i,j}|^q \Big)^{1/q}. \tag{3.3}$$

This regularizer applies a $\text{Tv}^{1\text{D}}_p$ regularization over each row of $\boldsymbol{X}$, and a $\text{Tv}^{1\text{D}}_q$ regularization over each column. Introducing differencing matrices $\boldsymbol{D}_n$ and $\boldsymbol{D}_m$ for the row and column dimensions, the regularizer (3.3) can be rewritten as

$$\text{Tv}^{2\text{D}}_{p,q}(\boldsymbol{X}) = \sum\nolimits_{i=1}^{n} \|\boldsymbol{D}_n \boldsymbol{x}_{i,:}\|_p + \sum\nolimits_{j=1}^{m} \|\boldsymbol{D}_m \boldsymbol{x}_{:,j}\|_q, \tag{3.4}$$

where $\boldsymbol{x}_{i,:}$ denotes the i-th row of $\boldsymbol{X}$, and $\boldsymbol{x}_{:,j}$ its j-th column. The corresponding $\text{Tv}^{2\text{D}}_{p,q}$-proximity problem is

$$\min\nolimits_{\boldsymbol{X}} \quad \tfrac{1}{2}\|\boldsymbol{X} - \boldsymbol{Y}\|_{\text{F}}^2 + \lambda \, \text{Tv}^{2\text{D}}_{p,q}(\boldsymbol{X}), \tag{3.5}$$

where we use the Frobenius norm $\|\boldsymbol{X}\|_{\mathrm{F}} = \sqrt{\sum_{ij} x_{i,j}^2} = \|\mathrm{vec}(\boldsymbol{X})\|_2$, where $\mathrm{vec}(\boldsymbol{X})$ is the vectorization of $\boldsymbol{X}$. Using (3.4), problem (3.5) becomes

$$\min_{\boldsymbol{X}} \quad \tfrac{1}{2}\|\boldsymbol{X} - \boldsymbol{Y}\|_{\mathrm{F}}^2 + \lambda \left(\sum\nolimits_i \|\boldsymbol{D}_n x_{i,:}\|_p \right) + \lambda \left(\sum\nolimits_j \|\boldsymbol{D}_m x_{:,j}\|_q \right), \tag{3.6}$$

where the parentheses make explicit that $\mathrm{Tv}_{p,q}^{\mathrm{2D}}$ is a combination of two regularizers: one acting over the rows and the other over the columns. Formulation (3.6) fits the model solvable by PD or DR, though with an important difference: each of the two regularizers that make up $\mathrm{Tv}_{p,q}^{\mathrm{2D}}$ is itself composed of a sum of several (n or m) 1D-TV regularizers. Moreover, each of the 1D row (column) regularizers operates on a different row (columns), and can thus be solved independently.

3.3 Higher-dimensional TV

Going even beyond $\mathrm{Tv}_{p,q}^{\mathrm{2D}}$ is the general multidimensional TV (1.3), which we recall below.

Let X be an order-m tensor in $\mathbb{R}^{\prod_{j=1}^m n_j}$, whose components are indexed as $\mathsf{X}_{i_1,i_2,\ldots,i_m}$ ($1 \leq i_j \leq n_j$ for $1 \leq j \leq m$); we define TV for X as

$$\mathrm{Tv}_{\boldsymbol{p}}^m(\mathsf{X}) \stackrel{\text{def}}{=} \sum_{k=1}^{m} \sum_{\{i_1,\ldots,i_m\}\setminus i_k} \Big(\sum_{j=1}^{n_k-1} |\mathsf{X}_{i_1,\ldots,i_{k-1},j+1,i_{k+1},\ldots,i_m} - \mathsf{X}_{i_1,\ldots,i_{k-1},j,i_{k+1},\ldots,i_m}|^{p_k} \Big)^{1/p_k}, \tag{3.7}$$

where $\boldsymbol{p} = [p_1, \ldots, p_m]$ is a vector of scalars $p_k \geq 1$. This corresponds to applying a 1D-TV to each of the 1D fibers of X along each of the dimensions.

Introducing the *multi-index* $\boldsymbol{i}(k) = (i_1, \ldots, i_{k-1}, i_{k+1}, \ldots, i_m)$, which iterates over every 1-dimensional fiber of X along the k-th dimension, the regularizer (3.7) can be written more compactly as

$$\mathrm{Tv}_{\boldsymbol{p}}^m(\mathsf{X}) = \sum\nolimits_{k=1}^{m} \sum\nolimits_{\boldsymbol{i}(k)} \|\boldsymbol{D}_{n_k} \boldsymbol{x}_{\boldsymbol{i}(k)}\|_{p_k}, \tag{3.8}$$

where $\boldsymbol{x}_{\boldsymbol{i}(k)}$ denotes a row of X along the k-th dimension, and $\boldsymbol{D}_{n_k}$ is a differencing matrix of appropriate size for the 1D-fibers along dimension k (of size n_k). The corresponding m-dimensional-TV proximity problem is

$$\min_{\mathsf{X}} \ \tfrac{1}{2}\|\mathsf{X} - \mathsf{Y}\|_{\mathrm{F}}^2 + \lambda\, \mathrm{Tv}_{\boldsymbol{p}}^m(\mathsf{X}), \tag{3.9}$$

where $\lambda > 0$ is a penalty parameter, and the Frobenius norm for a tensor just denotes the ordinary sum-of-squares norm over the vectorization of such tensor.

Problem (3.9) looks very challenging, but it enjoys decomposability as suggested by (3.8) and made more explicit by writing it as a sum of $\mathrm{Tv}^{\mathrm{1D}}$ terms

$$\min_{\mathsf{X}} \ \tfrac{1}{2}\|\mathsf{X} - \mathsf{Y}\|_{\mathrm{F}}^2 + \sum\nolimits_{k=1}^{m} \sum\nolimits_{\boldsymbol{i}(k)} \mathrm{Tv}_{p_k}^{\mathrm{1D}}\big(\boldsymbol{x}_{\boldsymbol{i}(k)}\big). \tag{3.10}$$

The proximity task (3.10) can be regarded as the sum of m proximity terms, each of which further decomposes into a number of inner $\mathrm{Tv}^{\mathrm{1D}}$ terms. These inner terms are trivial to address since, as in the 2D-TV case, each of the $\mathrm{Tv}^{\mathrm{1D}}$ terms operates on different entries of X. Regarding the m major terms, we can handle them by applying the PPD combiner algorithm (§3), which ultimately yields the prox operator for $\mathrm{Tv}_{\boldsymbol{p}}^m$ by just repeatedly calling $\mathrm{Tv}^{\mathrm{1D}}$ prox operators. Most importantly, both PPD and the natural decomposition of the problem provide a vast potential for parallel multithreaded computing, which is valuable when dealing with such complex and high-dimensional data.

4 1D-TV: Experiments and Applications

Since the most important components of our methods are the efficient 1D-TV prox operators, let us begin by highlighting their empirical performance. In particular, we compare our methods against state-of-the-art algorithms, showing the advantages of our approach.

Our solvers are implemented in C++, with calls to the LAPACK (FORTRAN) library [Anderson et al., 1999]. To permit reproducibility and to facilitate use of our TV prox-operators, we have made our complete toolbox available at: https://github.com/albarji/proxTV

We test solvers for 1D-TV regularization under two scenarios:

I) Increasing input size ranging from $n = 10^1$ to $n = 10^7$. A penalty $\lambda \in [0, 50]$ chosen at random for each run, and the data vector $\boldsymbol{y}$ with uniformly random entries $y_i \in [-2\lambda, 2\lambda]$ (proportionally scaled to λ).

II) Varying penalty parameter λ ranging from 10^{-3} (negligible regularization) to 10^3 (the TV term dominates); here n is set to 1000 and y_i is randomly generated in the range $[-2, 2]$ (uniformly).

4.1 Running time results for TV-L1

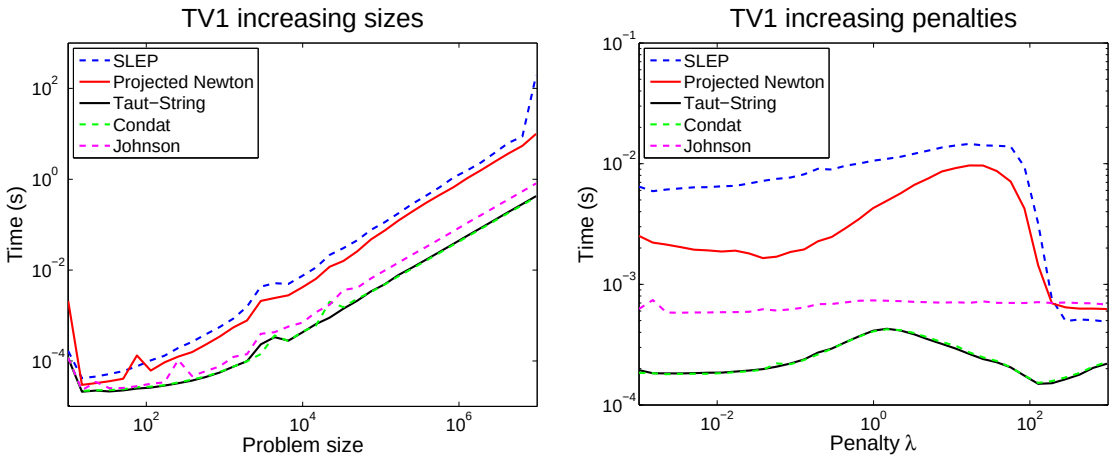

(a) (b)

Figure 6: Running times (in secs) for SLEP, Projected Newton, Taut String, Condat and Johnson solvers for $\mathrm{Tv}_1^{1\mathrm{D}}$-proximity with increasing a) input sizes, b) penalties. Both axes are on a log-scale. The proposed methods are marked as bold lines.

Starting with the proposed methods for $\mathrm{Tv}_1^{1\mathrm{D}}$ proximity (Projected Newton and Optimized Taut String), running times are compared against the following competing solvers:

- The **FLSA** function (C implementation) of the SLEP library of Liu et al. [2009] for $\mathrm{Tv}_1^{1\mathrm{D}}$-proximity [Liu et al., 2010].
- The state-of-the-art method of Condat [2012], which by a different reasoning arrives at an algorithm essentially equivalent to the (unweighted) taut-string method.
- The dynamic programming method of Johnson [2013], which guarantees linear running time.

For Projected Newton and SLEP a duality gap of 10^{-5} is used as the stopping criterion. The rest of algorithms are direct methods, and thus they are run until completion. Timing results are presented in Figure 6 for both experimental scenarios. The following interesting facts are drawn from these results

- Direct methods (Taut string, Condat, Johnson) prove to be much faster than iterative methods (Projected Newton, SLEP). This is true even for the case of the taut string and Condat's methods, which have a theoretical worst-case performance of $O(n^2)$. This possibility was already noted at Condat [2012].
- Even more, though Johnson's method has a guaranteed running time of $O(n)$, it turns out to be slower than the taut string and Condat's methods. This is explained by the need of Johnson's method of an extra $\sim 8n$ memory storage, which becomes a burden in contrast to the in-place strategies of taut string and Condat's.
- The best methods are taut string and Condat's solvers; both show equivalent performance for this unweighted TV problem.

4.2 Running time results for weighted TV-L1

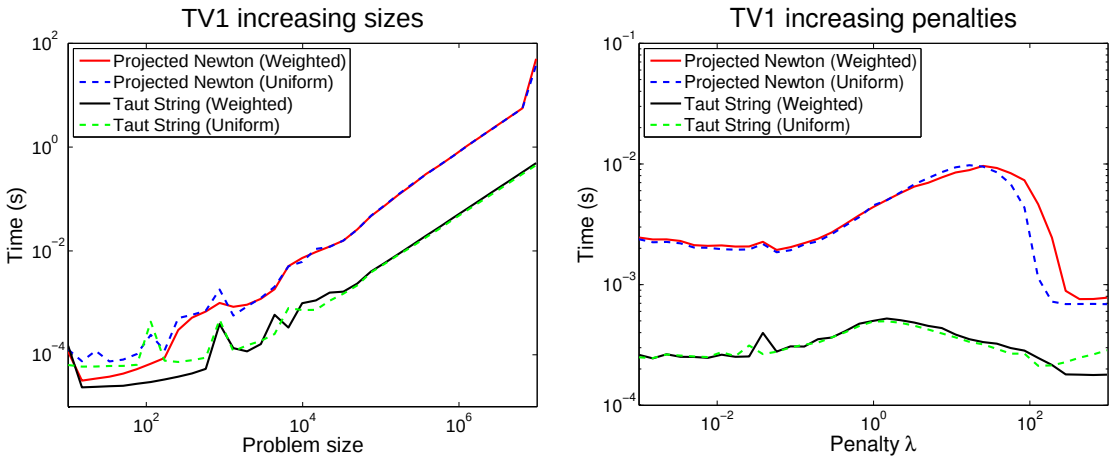

(a) (b)

Figure 7: Running times (in secs) for Projected Newton and Taut String solvers for weighted and uniform $\mathrm{Tv}_1^{1\mathrm{D}}$-proximity with increasing a) input sizes, b) penalties. Both axes are on a log-scale.

An advantage of the solvers proposed in this paper is their flexibility to easily deal with the more difficult, weighted version of the TV-L1 proximity problem. To illustrate this, Figure 7 shows the running times of the Projected Newton and Optimized Taut String methods when solving both the standard and weighted TV-L1 prox operators.

Since for this set of experiments a whole vector of weights $\boldsymbol{w}$ is needed, we have adjusted the experimental scenarios as follows:

I) n is generated as in the general setting, penalties $\boldsymbol{w} \in [0, 100]$ are chosen at random for each run, and the data vector $\boldsymbol{y}$ with uniformly random entries $y_i \in [-2\lambda, 2\lambda]$, with λ the mean of $\boldsymbol{w}$, using also this λ choice for the uniform (unweighted) case.

II) λ and n are generated as in the general setting, and the weights vector $\boldsymbol{w}$ is drawn randomly from the uniform distribution $\boldsymbol{w}_i \in [0.5\lambda, 1.5\lambda]$.

As can be readily observed, performance for both versions of the problem is almost identical, even if the weighted problem is conceptually harder. Conversely, adapting the other reviewed algorithms to address this problem while keeping up with performance is not a straightforward task.

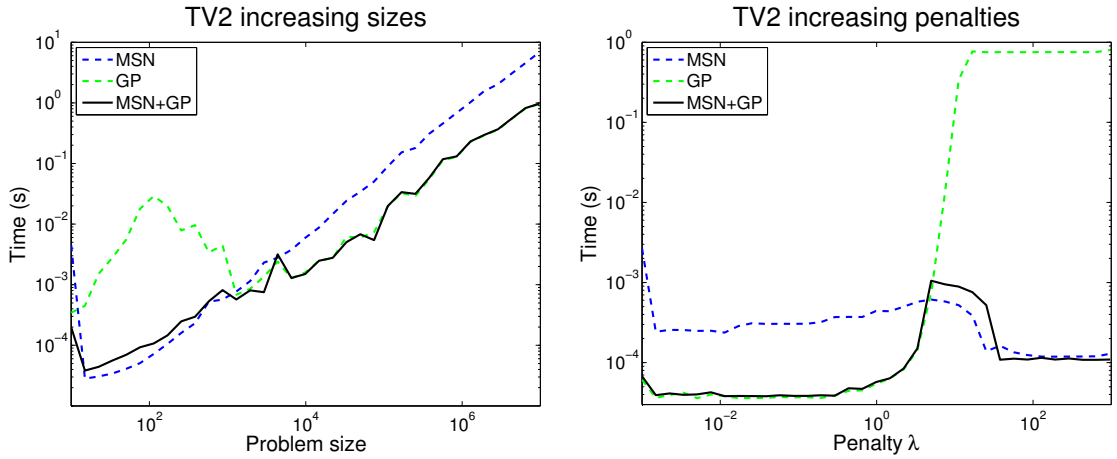

(a) (b)

Figure 8: Running times (in secs) for MSN, GP and a hybrid MSN+GP approach for $\mathrm{Tv}_2^{1\mathrm{D}}$-proximity with increasing a) input sizes, b) penalties. Both axes are on a log-scale.

4.3 Running time results for TV-L2

Next we show results for $\mathrm{Tv}_2^{1\mathrm{D}}$ proximity. To our knowledge, this version of TV has not been explicitly treated before, so there do not exist highly-tuned solvers for it. Thus, we show running time results only for the MSN and GP methods. We use a duality gap of 10^{-5} as the stopping criterion; we also add an extra boundary check for MSN with tolerance 10^{-6} to avoid early stopping due to potentially infeasible intermediate iterates. Figure 8 shows results for the two experimental scenarios under test.

The results indicate that the performance of MSN and GP differs noticeably in the two experimental scenarios. While the results for the first scenario (Figure 8(a)) might suggest that GP converges faster than MSN for large inputs, it actually does so depending on the size of λ relative to $\|\boldsymbol{y}\|_2$. Indeed, the second scenario (Figure 8(b)) shows that although for small values of λ, GP runs faster than MSN, as λ increases, GP's performance worsens dramatically, so much that for moderately large λ, it is unable to find an acceptable solution even after 10,000 iterations (an upper limit imposed in our implementation). Conversely, MSN finds a solution satisfying the stopping criterion under every situation, thus showing a more robust behavior.

These results suggest that it is preferable to employ a hybrid approach that combines the strengths of MSN and GP. Such a hybrid approach is guided using the following (empirically determined) rule of thumb: if $\lambda < \|\boldsymbol{y}\|_2$ use GP, otherwise use MSN. Further, as a safeguard, if GP is invoked but fails to find a solution within 50 iterations, the hybrid should switch to MSN. This combination guarantees rapid convergence in practice. Results for this hybrid approach are also included in the plots in Figure 8, and show how it successfully mimics the behavior of the better algorithm amongst MSN and GP.

4.4 Running time results for TV-Lp

Now we show results for $\mathrm{Tv}_p^{1\mathrm{D}}$ proximity. Again, to our knowledge efficient solvers for this version of TV are not available; still proposals for solving the ℓ_q-ball projection problem do exist, such as the *epp* function in SLEP library [Liu et al., 2009], based on a zero finding approach. Consequently, we present here a comparison between this reference projection subroutine and our PN–based projection when embedded in our proposed Gradient Projection solver of §2.3. The alternative proposal given by

the Frank–Wolfe algorithm of §2.3.2 is also present in the comparison. We use a duality gap of 10^{-5} as stopping criterion both for GP and FW. Figure 9 shows results for the two experimental scenarios under test, for p values of 1.5, 1.9 and 3.

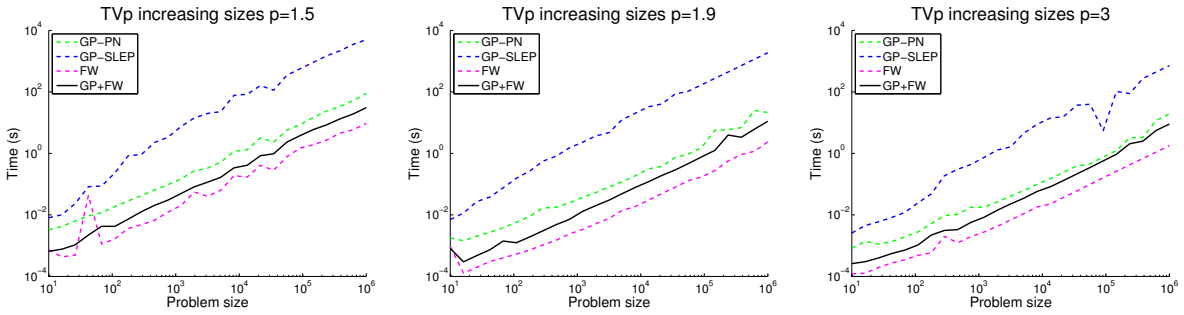

Figure 9: Running times (in secs) for GP with PN projection, GP with SLEP's *epp* projection, FW and a hybrid GP+FW algorithm, for $\mathrm{Tv}_p^{1\mathrm{D}}$-proximity with increasing input sizes and three different choices of p. Both axes are on a log-scale.

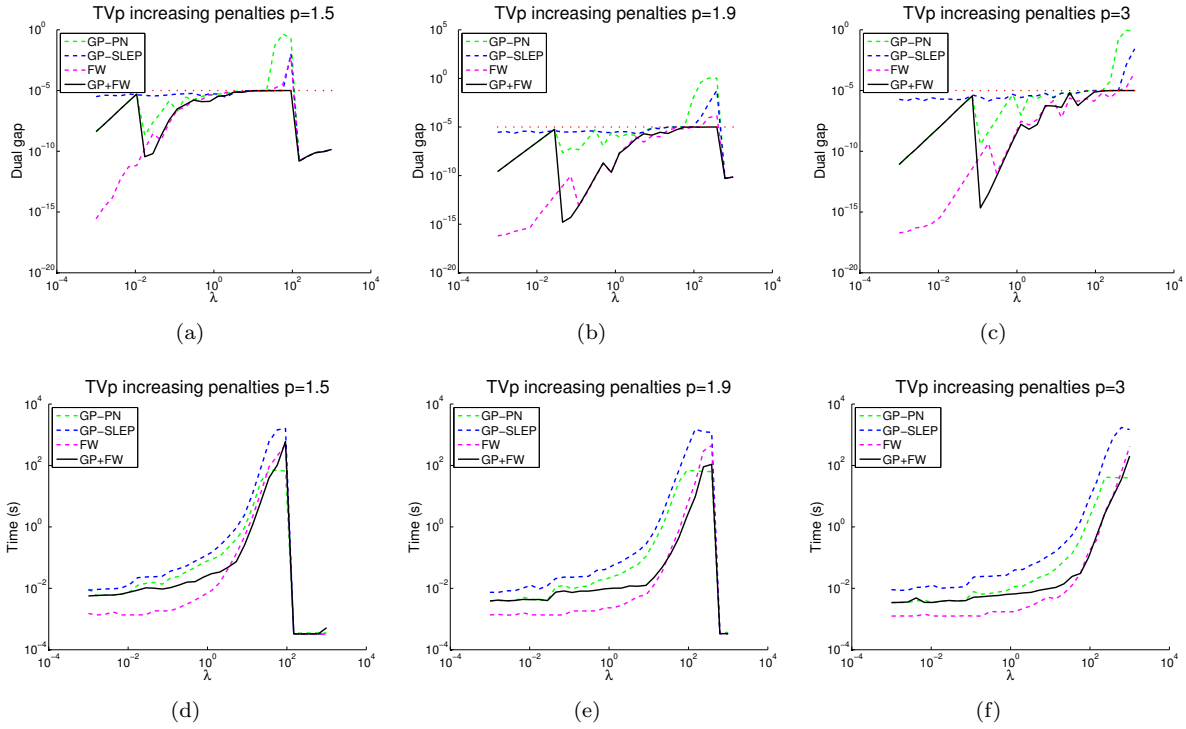

Figure 10: Attained duality gaps (a-c) and running times (d-f, in secs) for GP with PN projection, GP with SLEP's *epp* projection, FW and a hybrid GP+FW algorithm, for $\mathrm{Tv}_p^{1\mathrm{D}}$-proximity with increasing penalties and three different choices of p. Both axes are on a log-scale.

A number of interesting conclusions can be drawn from the results. First, our Projected Newton

ℓ_q-ball subroutine is far more efficient than *epp* when in the context of the GP solver. Two factors seem to be the cause of this: in the first place our Projected Newton approach proves to be faster than the zero finding method used by *epp*. Secondly, in order for the GP solver to find a solution within the desired duality gap, the projection subroutine must provide very accurate results (about 10^{-12} in terms of duality gap). Given its Newton nature, our ℓ_q-ball subroutine scales better in term of running times as a factor of the desired accuracy, which explains he observed differences in performance.

It is also of relevance noting that Frank–Wolfe is significantly faster than Projected Newton. This should discourage the use of Projected Newton, but we find it to be extremely useful in the range of λ penalties where λ is large, but not enough to render the problem trivial ($\boldsymbol{w} = 0$ solution). In this range the two variants of PN and also FW are unable to find a solution within the desired duality gap (10^{-5}), getting stuck at suboptimal solutions. We solve this issue by means of a hybrid GP+FW algorithm, in which updates from both methods are interleaved at a ratio of 10 FW updates per 1 GP update, as FW updates are faster. As both algorithms guarantee improvement in each iteration but follow different procedures for doing so, they complement each other nicely, resulting a superior method attaining the objective duality gap and performing faster than GP.

4.5 Running time results for TV-L∞

For completeness we also include results for our $\text{Tv}_\infty^{\text{1D}}$ solver based on GP + a standard ℓ_1-projection subroutine. Figure 11 presents running times for the two experimental scenarios under test. Since ℓ_1-projection is an easier problem than the general ℓ_q-projection the resultant algorithm converges faster to the solution than the general GP Tv_p^{1D} prox solver, as expected.

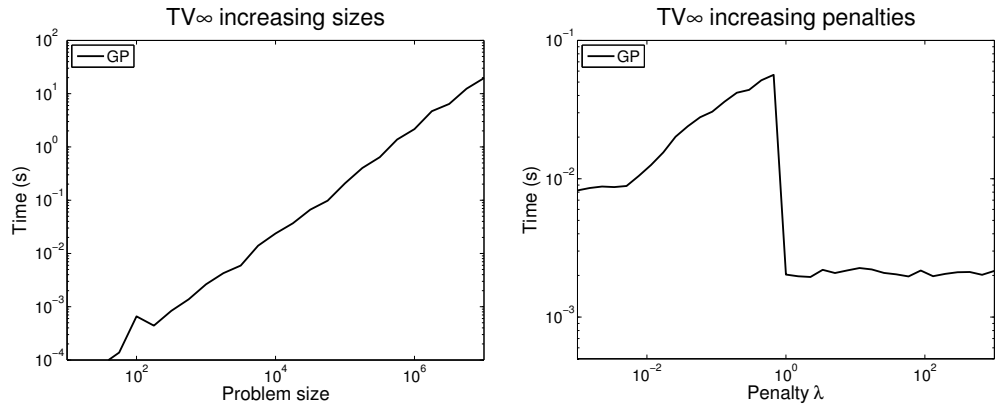

(a) (b)

Figure 11: Running times (in secs) for GP for $\text{Tv}_\infty^{\text{1D}}$-proximity with increasing a) input sizes, b) penalties. Both axes are on a log-scale.

4.6 Application: Proximal optimization for Fused-Lasso

We now present a key application that benefits from our TV prox operators: **Fused-Lasso** (FL) [Tibshirani et al., 2005], a model that takes the form

$$\min_{\boldsymbol{x}} \quad \tfrac{1}{2}\|\boldsymbol{A}\boldsymbol{x} - \boldsymbol{y}\|_2^2 + \lambda_1\|\boldsymbol{x}\|_1 + \lambda_2 \text{Tv}_1^{\text{1D}}(\boldsymbol{x}). \tag{4.1}$$

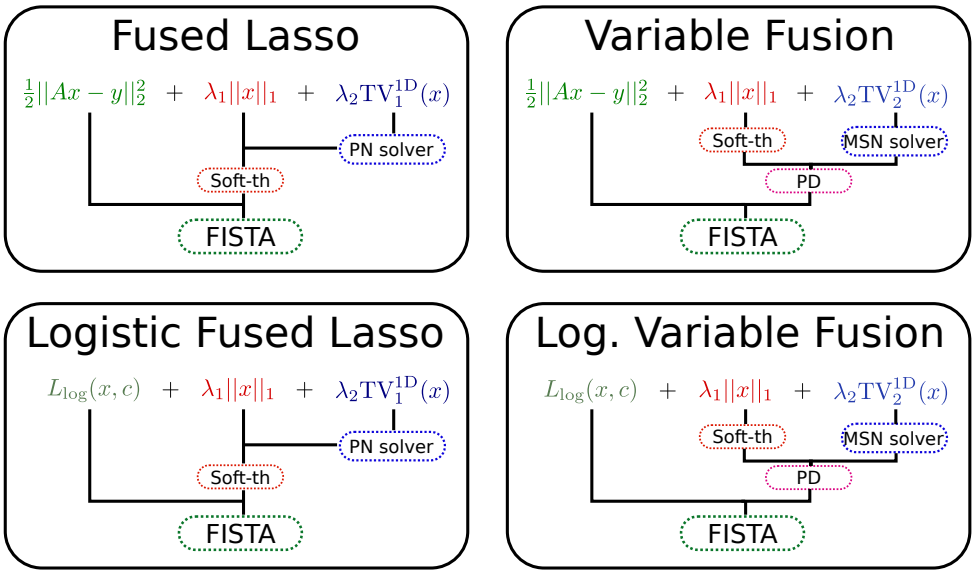

Figure 12: Fused-Lasso models addressed by proximal splitting.

The ℓ_1-norm in (4.1) forces many x_i to be zero, while $\mathrm{Tv}_1^{1\mathrm{D}}$ favors nonzero components to appear in blocks of equal values $x_{i-1} = x_i = x_{i+1} = \ldots$. The FL model has been successfully applied in several bioinformatics applications [Tibshirani and Wang, 2008, Rapaport and Vert, 2008, Friedman et al., 2007], as it encodes prior knowledge about consecutive elements in microarrays becoming active at once.

Following the ideas presented in Sec. 3, since the FL model uses two regularizers, we can use Proximal Dykstra as the combiner to handle the prox operator. To illustrate the benefits of this framework in terms of reusability, we apply it to several variants of FL.

- **Fused-Lasso (FL):** Least-squares loss $+\ell_1 + \mathrm{Tv}_1^{1\mathrm{D}}$ as in (4.1)
- **ℓ_p-Variable Fusion (VF):** Least-squares loss $+\ell_1 + \mathrm{Tv}_p^{1\mathrm{D}}$. Though Variable Fusion was already studied by Land and Friedman [1997], their approach proposed an ℓ_p^p-like regularizer in the sense that $r(\boldsymbol{x}) = \sum_{i=1}^{n-1} |x_{i+1} - x_i|^p$ is used instead of the TV regularizer $\mathrm{Tv}_p^{1\mathrm{D}}(x) = \left(\sum_{i=1}^{n-1} |x_{i+1} - x_i|^p\right)^{1/p}$. Using Tv_p leads to a more conservative penalty that does not oversmooth the estimates. This FL variant seems to be new.
- **Logistic-fused lasso (LFL):** Logistic-loss $+\ell_1 + \mathrm{Tv}_1^{1\mathrm{D}}$, where the loss takes the form $\ell(\boldsymbol{x}, c) = \sum_i \log\left(1 + e^{-y_i(\boldsymbol{a}_i^T \boldsymbol{x} + c)}\right)$, and can be used in a FL formulation to obtain models more appropriate for classification on a dataset $\{(\boldsymbol{a}_i, y_i)\}$ [Kolar et al., 2010].
- **Logistic + ℓ_p-fusion (LVF):** Logistic loss $+\ell_1 + \mathrm{Tv}_p^{1\mathrm{D}}$.

To solve these variants of FL, all that remains is to compute the gradients of the loss functions, but this task is trivial. Each of these four models can be then solved easily by invoking any proximal splitting method by appropriately plugging in gradient and prox operators. Incidentally, the **SLEP** library [Liu et al., 2010] includes an implementation of FISTA [Beck and Teboulle, 2009] carefully tuned for Fused Lasso, which we base our experiments on. Figure 12 shows a schematic of the algorithmic modules for solving each FL model.

Remark: A further algorithmic improvement can be obtained by realizing that for $r(\boldsymbol{x}) = \lambda_1 \|\boldsymbol{x}\|_1 + \lambda_2 \mathrm{Tv}_1^{1\mathrm{D}}(\boldsymbol{x})$ the prox operator $\mathrm{prox}_r \equiv \mathrm{prox}_{\lambda_1\|\cdot\|_1} \circ \mathrm{prox}_{\lambda_2 \mathrm{Tv}_1^{1\mathrm{D}}(\cdot)}$. Such a decomposition does not usually

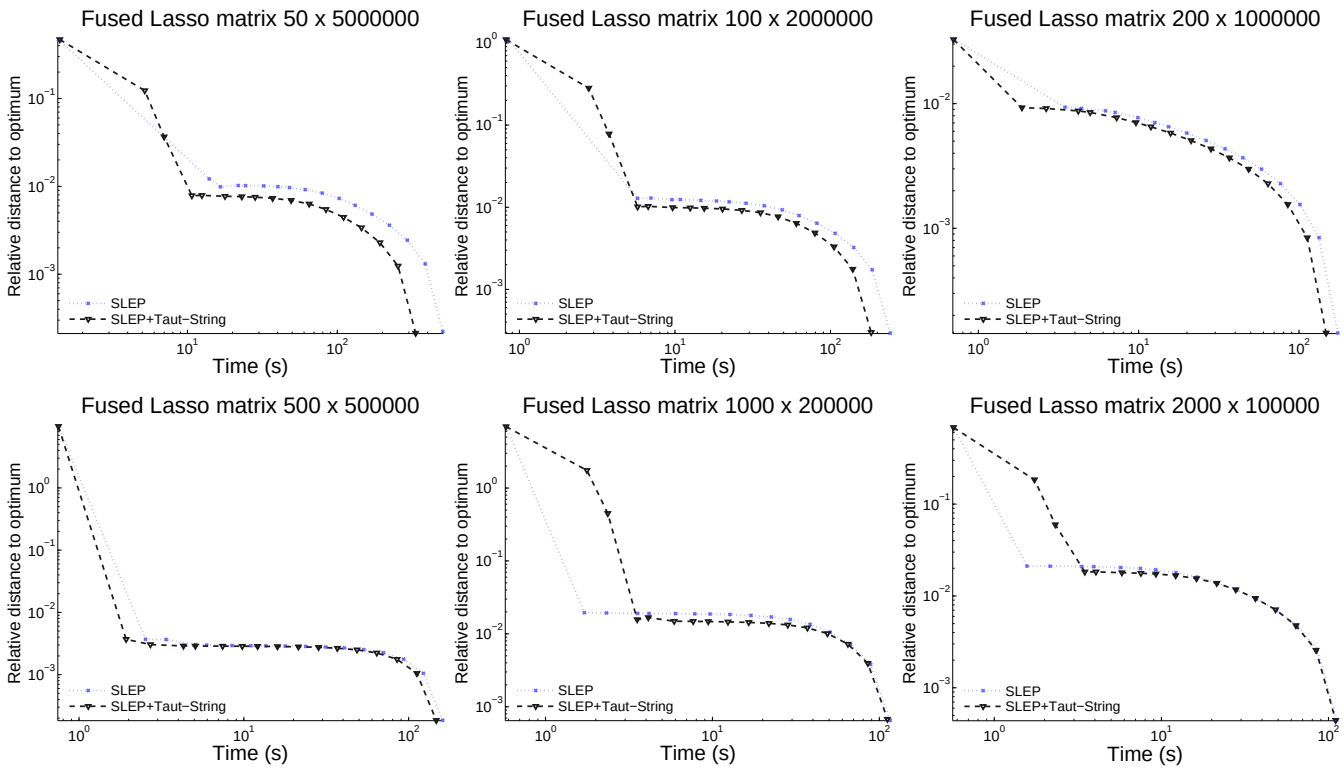
Fused Lasso matrix 50 x 5000000
Fused Lasso matrix 100 x 2000000
Fused Lasso matrix 200 x 1000000
Fused Lasso matrix 500 x 500000
Fused Lasso matrix 1000 x 200000
Fused Lasso matrix 2000 x 100000
Relative distance to optimum
Time (s)
SLEP
SLEP+Taut−String

Figure 13: Relative distance to optimum vs time of the Fused Lasso optimizers under comparison, for the different layouts of synthetic matrices.

hold, but it can be shown to hold for this particular case [Yu, 2013, Rinaldo, 2009, Tibshirani et al., 2005]. Therefore, for FL and LFL we can compute the proximal operator for the combined regularizer r directly, thus removing the need for a combiner algorithm. This is also shown in Figure 12.

4.6.1 Fused-Lasso experiments: simulation

The standard FL model has been well-studied in the literature, so a number of practical algorithms addressing it have already been proposed. The aforementioned Fused-Lasso algorithm in the **SLEP** library can be regarded as the state of the art, making extensive use of an efficient proximity subroutine (FLSA). Our experiments on $\mathrm{Tv}_1^{\mathrm{1D}}$-proximity (§4) have already shown superiority of our prox solvers over FLSA; what remains to be checked is whether this benefit has a significant impact on the overall FL solver. To do so, we compare running times with synthetic data.

We generate random matrices $\boldsymbol{A} \in \mathbb{R}^{n \times m}$ with i.i.d. entries drawn from a zero mean, unit variance gaussian. We set the penalties to $\lambda_1 = \lambda_2 = 10$. We select the vector of responses $\boldsymbol{y}$ using the formula $\boldsymbol{y} = \mathrm{sgn}(\boldsymbol{A}\boldsymbol{x}_t + \boldsymbol{v})$, where $\boldsymbol{x}_t$, and $\boldsymbol{v}$ are random vectors whose entries have variances 1 and 0.01, respectively. The numerical results are summarized in Figure 13, which compares out of the box SLEP (version 4.0) [Liu et al., 2009] against the very same algorithm employing our fast taut–string $\mathrm{Tv}_1^{\mathrm{1D}}$ solver instead of the default FLSA subroutine of SLEP. Comparison is done by showing the relative distance to the problem's optimum versus time. The optimal values in each setting were estimated by running both algorithms for a very large number of iterations.

The plots show a clear trend: when the input matrices feature a very large column dimension the

Table 1: Classification accuracies for the presented Fused–Lasso models on microarray data. For the Variable Fusion models an ℓ_2 version of TV was employed.

Dataset	FL	VF-ℓ_2	LFL	LVF-ℓ_2
ArrayCGH	73.6%	73.6%	**84.2%**	73.6%
Leukemias	**92.0%**	88.0%	**92.0%**	88.0%
Colon	**77.2%**	**77.2%**	**77.2%**	**77.2%**
Ovarian	**88.8%**	83.3%	83.3%	83.3%
Rat	68.8%	65.5%	**72.1%**	**72.1%**

use of our taut-string $\mathrm{Tv}_1^{\mathrm{1D}}$ solver turns into speedups in optimization times, which however become negligible for matrices with a more balanced rows/columns ratio. This result is reasonable, as the vector x under optimization has size equal to the number of columns of the data matrix A. If A has a large number of columns the cost of solving $\mathrm{Tv}_1^{\mathrm{1D}}$ is significant, and thus any improvement in this step has a noticeable impact on the overall algorithm. Conversely, when the number of rows in A is large the cost of computing the gradient of the loss function ($\nabla \frac{1}{2}\|\boldsymbol{A}\boldsymbol{x} - \boldsymbol{y}\|_2^2 = \boldsymbol{A}^T(\boldsymbol{A}\boldsymbol{x} - \boldsymbol{y})$) dominates, getting limited benefits from such improvements in prox computations. Therefore, it is for data with a very large number of features where our proposed method can provide a useful speedup.

4.6.2 Fused-Lasso Experiments: Microarray classification

Now we report results of applying the four FL models on a series of problems from bioinformatics. We test the FL models on binary classification tasks for the following real microarray datasets: ArrayCGH [Stransky et al., 2006], Leukemias [Golub et al., 1999], Colon [U. Alon et al., 1999], Ovarian [Rogers et al., 2005] and Rat [Hua et al., 2009]. Each dataset was split into three equal parts (ensuring similar proportion of classes in every split) for training, validation and test. The penalty parameters were found by exhaustive grid search in the range $\lambda_1, \lambda_2 \in [10^{-4}, 10^2]$ to maximize classification accuracy on the validation splits.

Table 1 shows test accuracies. In general, as expected the logistic-loss based FL models yield better classification accuracies than those based on least-squares, as such loss function tends to be more appropriate for classification problems. However the Ovarian dataset proves to be an exception, showing better performance under a squared loss. Regarding the TV-regularizer, the classic $\mathrm{Tv}_1^{\mathrm{1D}}$-penalty seems to perform better in general, with the $\mathrm{Tv}_2^{\mathrm{1D}}$-penalty showing competitive results in some settings.

5 2D-TV: Experiments and Applications

We address now several practical applications that benefit from two-dimensional TV regularization; our results show again how our $\mathrm{Tv}_{p,q}^{\mathrm{2D}}$ prox operator fits in seamlessly into our modular framework to produce efficient proximal splitting solvers.

5.1 Image denoising through anisotropic filtering

Our first example is to the classic problem of image denoising, but with the twist that we deal with noise of an anisotropic character. More specifically, suppose that the true image $\mu \in \mathbb{R}^{n \times m}$ is contaminated by additive noise $\boldsymbol{N}$, so that only $\mu_0 = \mu + \boldsymbol{N}$ is observed. The denoising problem estimates μ given just the noisy version μ_0. This problem is highly ill-posed and as such not approachable unless additional assumptions on the noise (or on the underlying image) are made.

5.1.1 Isotropic and anisotropic models

An extremely common choice is to simply assume the noise to be gaussian, or some other zero-mean distribution. Under these conditions, a classic method to perform such denoising task is the **Rudin-Osher-Fatemi** (ROF) model [Rudin et al., 1992], which finds an approximation $\boldsymbol{X}$ to the original image by solving

$$\min_{\boldsymbol{X}} \quad \|\boldsymbol{X} - \mu_0\|_{\mathrm{F}}^2 + \lambda \sum_{i=2}^{n} \sum_{j=2}^{m} \|\partial x_{i,j}\|_2, \tag{5.1}$$

where $\partial x_{i,j}$ is the *discrete gradient*

$$\partial x_{i,j} = \begin{bmatrix} x_{i,j} - x_{i-1,j} \\ x_{i,j} - x_{i,j-1} \end{bmatrix}.$$

That is, it is the vector of differences of $\boldsymbol{X}_{i,j}$ and its neighbors along both axes.

The objective of the first term in the ROF model is to penalize any deviation of $\boldsymbol{X}$ from the observed image μ_0, while the second term can be readily recognized as a mixed $(2,1)$-norm over the discrete gradient of $\boldsymbol{X}$. This regularizer models caters to some prior knowledge: in natural images sharp discontinuities in intensity between neighboring points only appear in borders of objects, while the rest of the pixels usually show smooth variations in intensity. It makes sense, therefore, to penalize large values of the gradient, as sharp changes have a higher probability of having being produced by noise. Conversely, as the mean of the noise is zero, it is also sensible to maintain the denoised image $\boldsymbol{X}$ close to the observed μ_0. Merging these two goals produces the ROF model (5.1).

A closer look at the ROF regularizer reveals that it follows the spirit of our 2D-TV regularizer which also penalizes sharp variations between neighboring pixels. Indeed, all such regularizers are broadly categorized as TV regularizers within the image processing community. It is clear, though, that the ROF regularizer (5.1) does not coincide with our $\mathrm{Tv}_{p,q}^{\mathrm{2D}}$ regularizer. Some authors [Bioucas-Dias and Figueiredo, 2007] differentiate between these regularizers by naming the ROF approach as **isotropic TV** and the $\mathrm{Tv}_{p,q}^{\mathrm{2D}}$-style approach as **anisotropic TV**. This naming comes from the fact that isotropic TV penalizes each component of the discrete gradient $\partial x_{i,j}$ following an ℓ_2 norm, whereas the anisotropic $\mathrm{Tv}_{p,q}^{\mathrm{2D}}$-norm and in particular $\mathrm{Tv}_{1,1}^{\mathrm{2D}}$-norm, penalize rows and columns independently.

While image filtering using isotropic TV is generally preferred for natural images denoising [Bioucas-Dias et al., 2006], in some settings anisotropic filtering can produce better results, and in fact has been favored by some authors in the past [Choksi et al., 2010, Li and Santosa, 1996]. This is specially true on those images that present a "blocky" structure, and thus are better suited to the structure modeled by the $\mathrm{Tv}_{p,q}^{\mathrm{2D}}$-norm. Therefore, efficient methods to perform anisotropic filtering are also important.

5.1.2 Anisotropic denoising experiments

Denoising using the anisotropic $\mathrm{Tv}_{p,q}^{\mathrm{2D}}$-norm reduces to solving

$$\min_{\boldsymbol{X}} \quad \|\boldsymbol{X} - \mu_0\|_{\mathrm{F}}^2 + \lambda \mathrm{Tv}_{p,q}^{\mathrm{2D}}(\boldsymbol{X}). \tag{5.2}$$

But (5.2) is nothing but the $\mathrm{Tv}_{p,q}^{\mathrm{2D}}$-proximity problem, and hence can be directly solved by applying the 2D-TV prox operators developed above. We solve (5.2) below for the choice $p = q = 1$ (which is common in practice), and compare it against the following state of the art algorithms:

- The Split Bregman method of Goldstein T. [2009], which follows an ADMM–like approach to split the ℓ_1 norm apart from the discrete gradient operator, thus not requiring the use of a 1D-TV prox operator.

- The splitting method by Chambolle and Pock [2011], which can be thought as a kind of preconditioned ADMM algorithm.
- The general splitting method by Condat [2014], which is a generalization of the method by Chambolle and Pock.
- The method by Yang et al. [2013] which also proposes an ADMM approach, though splitting the problem in a way that takes advantage of fast 1D-TV prox operator.
- The maximum flow approach by Goldfarb and Yin [2009], which shows the relationship between the 2D-TV proximity minimization and the maximum flow problem over a grid, and thus applies an efficient maximum flow method to solve a discrete-valued version of 2D-TV.

The method by Yang et al. is the closest in spirit to our stacking proposal, also relying on basic 1D-TV prox solvers. Both for this method and our proposed algorithms we use the taut–string strategy presented before as this basic piece. All algorithm parameters were set as recommended in their corresponding papers or public implementations, except our proposed methods, which are parameter free.

Table 2: Types of noise and parameters for each test image. A ∅ indicates that such noise was not applied for the image. *Gaussian* and *Speckle* correspond to gaussian additive and multiplicative (respectively) noises with zero mean and the indicated variance. *Salt & Pepper* noise turns into black or white the indicated fraction of image pixels. *Poisson* regenerates each pixel by drawing a random value from a Poisson distribution with mean equal to the original pixel value, thus producing a more realistic noise.

Image	Gaussian	Speckle	Poisson	Salt & Pepper
randomQR	0.2	0.3	∅	∅
shape	0.05	∅	∅	∅
trollface	∅	1	∅	∅
diagram	∅	∅	✓	∅
text	∅	∅	∅	0.1
comic	0.05	∅	✓	∅
contour	∅	∅	✓	0.4
phantom	∅	2	✓	∅

The images used in the experiments are displayed in Appendix D as Figure 21. To test the filters under a variety of scenarios, different kinds of noise were introduced for each image. Table 2 gives details on this, while the noisy images are shown in Figure 22. All QR barcode images used the same kind and parameters of noise. Noise was introduced using Matlab's *imnoise* function.

Values for the regularization parameter λ were found by maximizing the quality of the reconstruction, measured using **Improved Signal-to-Noise Ratio** (ISNR) [Afonso et al., 2010]. ISNR is defined as

$$\mathrm{ISNR}(\boldsymbol{X}, \mu, \mu_0) = 10 \log_{10} \frac{\|\mu_0 - \boldsymbol{X}\|_{\mathrm{F}}^2}{\|\boldsymbol{X} - \mu\|_{\mathrm{F}}^2},$$

where μ is the original image, μ_0 its noisy variant, and $\boldsymbol{X}$ the reconstruction.

To compare the algorithms we run all of them for each image and measured its ISNR and relative distance to the optimal objective value of the current solution at each iteration through their execution. The only exception to this procedure is the method of Goldfarb and Yin, which is non–iterative and thus always returns an exact solution, and so we just measure the time required to finish. The optimal objective value was estimated by running all methods for very large number of iterations and taking the minimum value of them all. This produced the plots shown in Figures 14-15. From them the following observations are of relevance

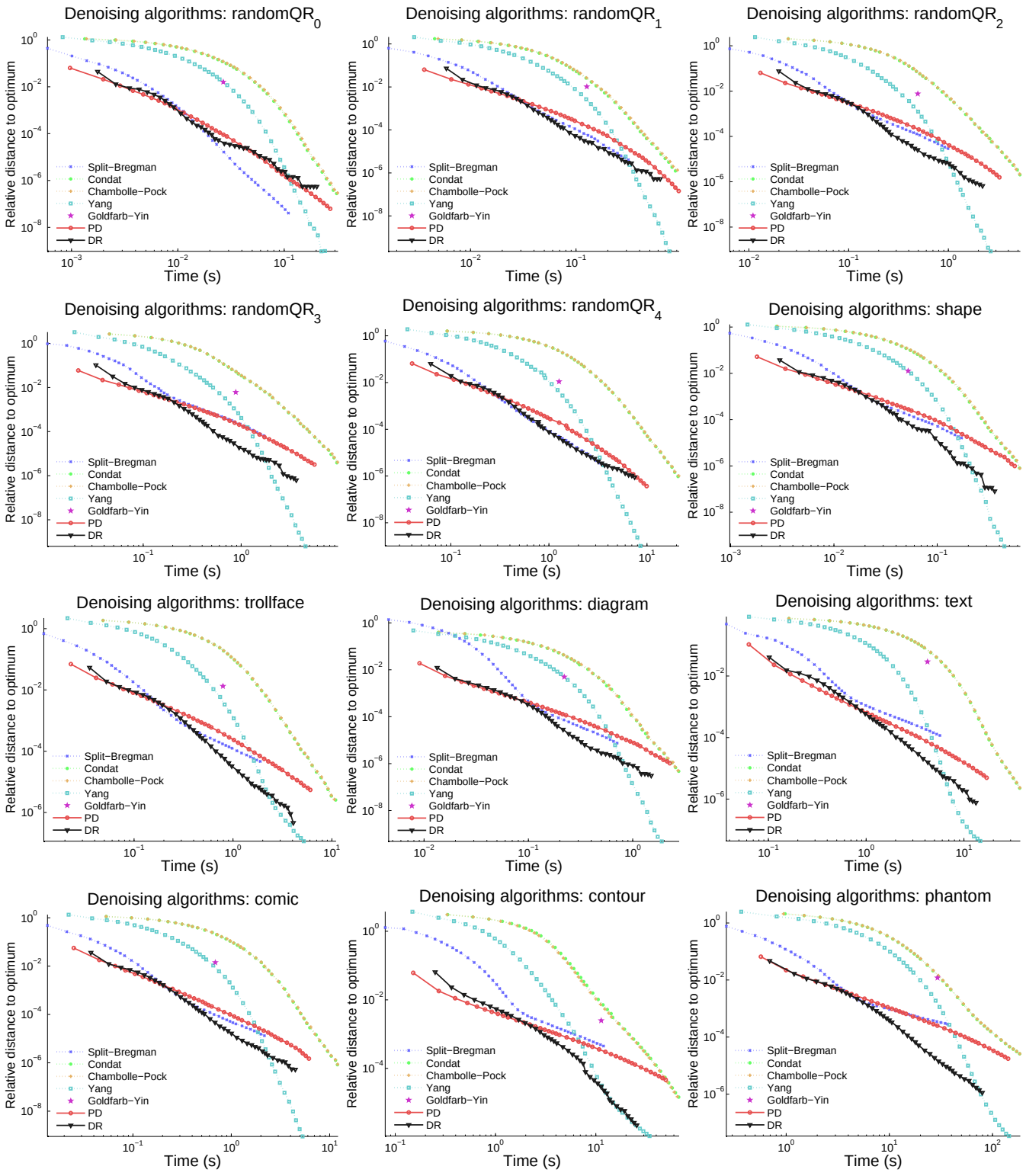

Figure 14: Relative distance to optimum vs time of the denoising 2D-TV algorithms under comparison, for the different images considered in the experiments.

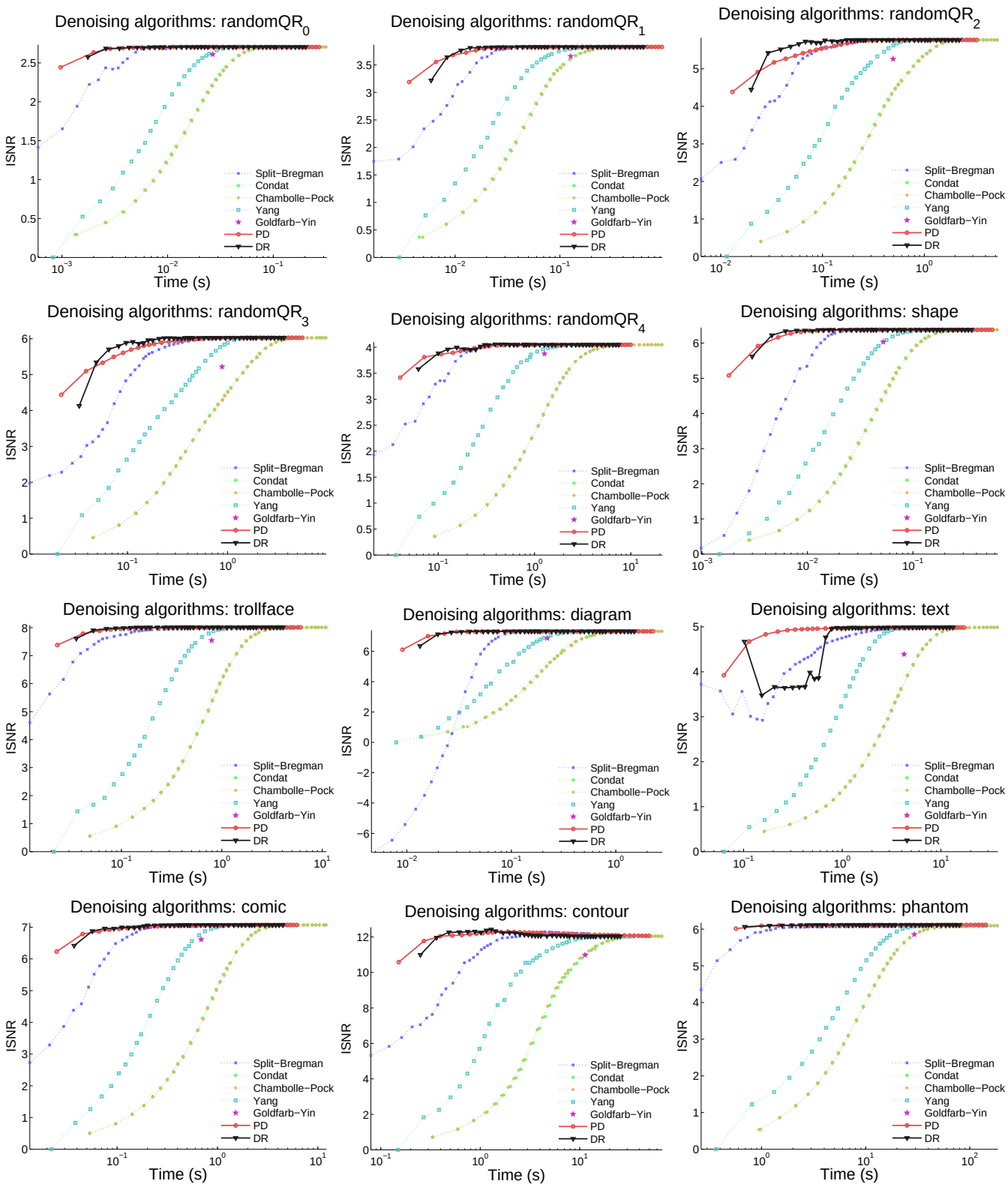

Figure 15: Increased Signal to Noise Ratio (ISNR) vs time of the denoising 2D-TV algorithms under comparison, for the different images considered in the experiments.

- Condat's method and Chambolle-Pock's method are reduced to essentially the same algorithm when applied to the particular case of TV denoising. Furthermore, they seem to perform slowly when compared to other methods.
- Yang's method exhibits slow performance at the beginning, but when run for sufficient time is able to achieve the best approximation to the optimum.
- The Split Bregman method, in spite of being an ADMM–like method much like Condat's or Chambolle-Pock, performs significantly better than those. We attribute this to the very efficient implementation provided by its authors, and to the fact that a fast approximate method is employed to compute the required matrix inversions throughout the method.
- The method by Goldfarb and Yin is slower than other approaches and seems to provide suboptimal solutions. We attribute this to the fact that this method solves a discrete (integer–rounded) approximation to the problem. We acknowledge that other methods exploiting the Total Variation - Minimum-cut relationship have been proposed with varying speed results, e.g. [Duan and Tai, 2012], however the suboptimality issues still apply.
- The two approaches proposed in this paper are the fastest to achieve a mid-quality solution, with Douglas-Rachford performing better than Proximal Dykstra.

Considering these facts, the method of choice among the ones considered depends on the desired accuracy. We argue, however, that for the purpose of image processing a mid-quality solution is sufficient. The ISNR plots of Figure 15 certainly seem to support this, as the perceived quality of the reconstruction, roughly approximated by the ISNR, saturates rapidly and no significant improvements are obtained through further optimization. Given this, the proposed methods seem to be the best suited for the considered task.

For quick reference, Table 3 presents a summary of key points of the compared methods, along with some recommendations about when to put them to use.

5.1.3 Parallelization experiments

In addition to the previous experiments and to illustrate the parallelization potential of the developed anisotropic filtering method, Figure 16 plots running times for the PD algorithm as the number of processor core ranges from 1 through 16. We see that for the smaller images, the gains due to more processors essentially flatten out by 8 cores, where synchronization and memory contention offsets potential computational gains (first row). For the larger images, there is steadier speedup as the number of cores increase (in each plot there seems to be a "bump" at 14 processors; we attribute this to a quirk of the multicore machine that we used). From all the plots, however, the message is clear: our TV prox operators exploit parallelization well, and show substantial speedups as more processor cores become available.

5.2 Anisotropic image deconvolution

Taking a step forward we now confront the problem of **image deconvolution** (or image deblurring). This setting is more complex since the task of image recovery is made harder by the presence of a **convolution kernel** K that distorts the image as

$$\mu_0 = \boldsymbol{K} * \mu + \boldsymbol{N},$$

where $\boldsymbol{N}$ is noise as before and $*$ denotes convolution. To recover the original image μ from the observed μ_0, it is common to solve the following deconvolution problem

$$\min_{\boldsymbol{X}} \quad \tfrac{1}{2}\|\boldsymbol{K} * \boldsymbol{X} - \mu\|_{\mathrm{F}}^2 + \lambda r(\boldsymbol{X}). \tag{5.3}$$

Table 3: Summary of key points of the compared $\mathrm{Tv}^{2\mathrm{D}}_{1,1}$ proximity (denoising) methods.

Method		Key points
Douglas Rachford	+	Fast convergence to medium-quality
	+	Embarrassingly parallel
	−	Slow for higher accuracies
	⇒	Ideal for standard denoising tasks
Proximal Dykstra	+	Attainable accuracies similar to DR
	−	But slower than DR
	⇒	Use DR instead
Split Bregman	+	Eventually performs similarly to DR
	−	Slow convergence at first iterations
	⇒	Use DR instead
Chambolle–Pock	−	Slow
	⇒	Use other method instead
Condat	+	Solves objectives involving a sum of smooth/non–smooth functions with linear operators
	−	Reduces to Chambolle–Pock when solving basic image denoising
	⇒	Use only when dealing with more complex functionals
Yang	+	More accurate
	−	Slow
	⇒	Useful when extremely accurate solutions are required
Goldfarb-Yin	+	Solves the discrete version of the problem
	−	Slow
	−	Poor accuracy for the continuous version
	⇒	Apply only when solving the discrete problem

As before the regularizer $r(\boldsymbol{X})$ can be isotropic or anisotropic TV, among others. Here we focus again on the anisotropic TV case to show how our solvers can also be used for this image task.

Problem (5.3) also fits the proximal splitting framework, and so we employ the popular FISTA [Beck and Teboulle, 2009] method for image processing. The gradient of the loss can be dealt efficiently by exploiting $\boldsymbol{K}$ being a convolution operator, which through the well–known convolution theorem is equivalent to a dot product in the frequencies space, and so the computation is done by means of fast Fourier transforms and products. Several other solvers that explicitly deal with convolution operators are also available [Afonso et al., 2010, Bioucas-Dias and Figueiredo, 2007]. A notable solver specific for the isotropic case is given by the work of Krishnan and Fergus [2009], that handles even nonconvex isotropic TV-norms ($0 < p < 1$). But this approach does not extend to the anisotropic case, so we focus on general proximal splitting.

We use the same test images as for our denoising experiments (Figure 21), with identical noise patterns (Table 2) for the QR images, and gaussian noise with variance 0.05 for the rest. In addition, we convolve each image with a different type of kernel to assess the behavior for a variety of convolutions; Table 4 shows the kernels applied. We constructed these kernels using Matlab's *fspecial* function; the convolved

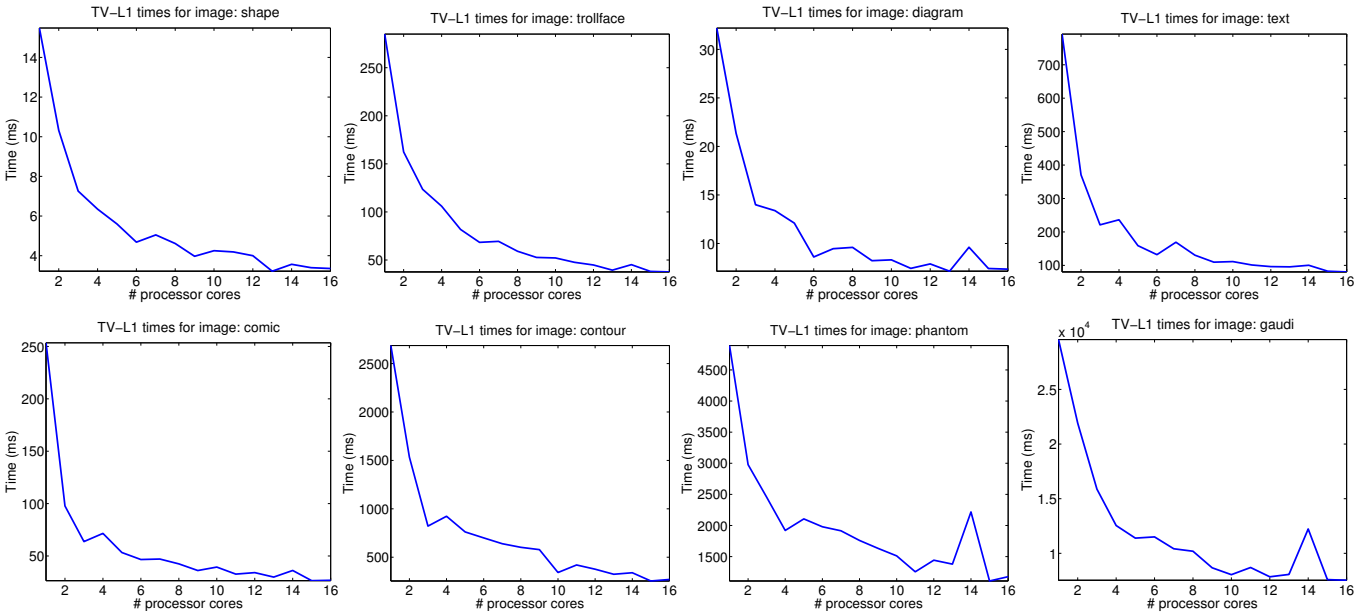
TV–L1 times for image: shape
TV–L1 times for image: trollface
TV–L1 times for image: diagram
TV–L1 times for image: text
TV–L1 times for image: comic
TV–L1 times for image: contour
TV–L1 times for image: phantom
TV–L1 times for image: gaudi
Time (ms)
processor cores
x 10^4

Figure 16: Multicore speedups on different images (see also Table 4)

images are shown in Figure 24.

The values for the regularizer λ were determined by maximizing the reconstruction quality measured in ISNR. Since deconvolution is much more expensive than denoising, instead of performing an exhaustive search for the best λ, we used a Focused Grid Search strategy [Barbero et al., 2008, 2009] to find the best performing values.

Any denoising subroutine can be plugged into the aforementioned deconvolution methods, however for comparison purposes we run our experiments with our best proposed method, Douglas Rachford, and the best competing method, Split Bregman. A key parameter in deconvolution performance is for how long should these methods be run at each FISTA iteration. To select this, we first run FISTA with 100 iterations of Douglas Rachford per step, for a large number of FISTA steps, and take the final objective value as an estimate of the optimum. Then we find the minimum number of Douglas Rachford and Split Bregman iterations for which FISTA can achieve a relative distance to such optimum below 10^{-3}. The reason for doing this is that for larger distances the attained ISNR values are still far from convergence. This turned to be 5 iterations for Douglas Rachford and 20 for Split Bregman. We then run FISTA for such configurations of the inner solvers, and others with a larger number of inner iterations, for comparison purposes.

Figures 17-18 shows the evolution of objective values and ISNR for all the tested configurations. In general, Douglas Rachford seems to be slightly better at finding more accurate solutions, though in terms of ISNR both methods converge similarly. We explain this by the fact that the major advantage of Douglas Rachford is its aforementioned ability to find medium–quality solutions in a very small number of iterations. However, for image deconvolution we have seen that a minimum of 5 Douglas Rachford iterations are needed to achieve convergence in ISNR, and at such level the method tends to behave similarly to Split Bregman (see denoising experiments above), only becoming better at higher accuracies, as observed.

We conclude therefore that Douglas Rachford and Split Bregman perform similarly for image deconvolution, with Douglas Rachford being superior only when high–accuracy solutions are sought.

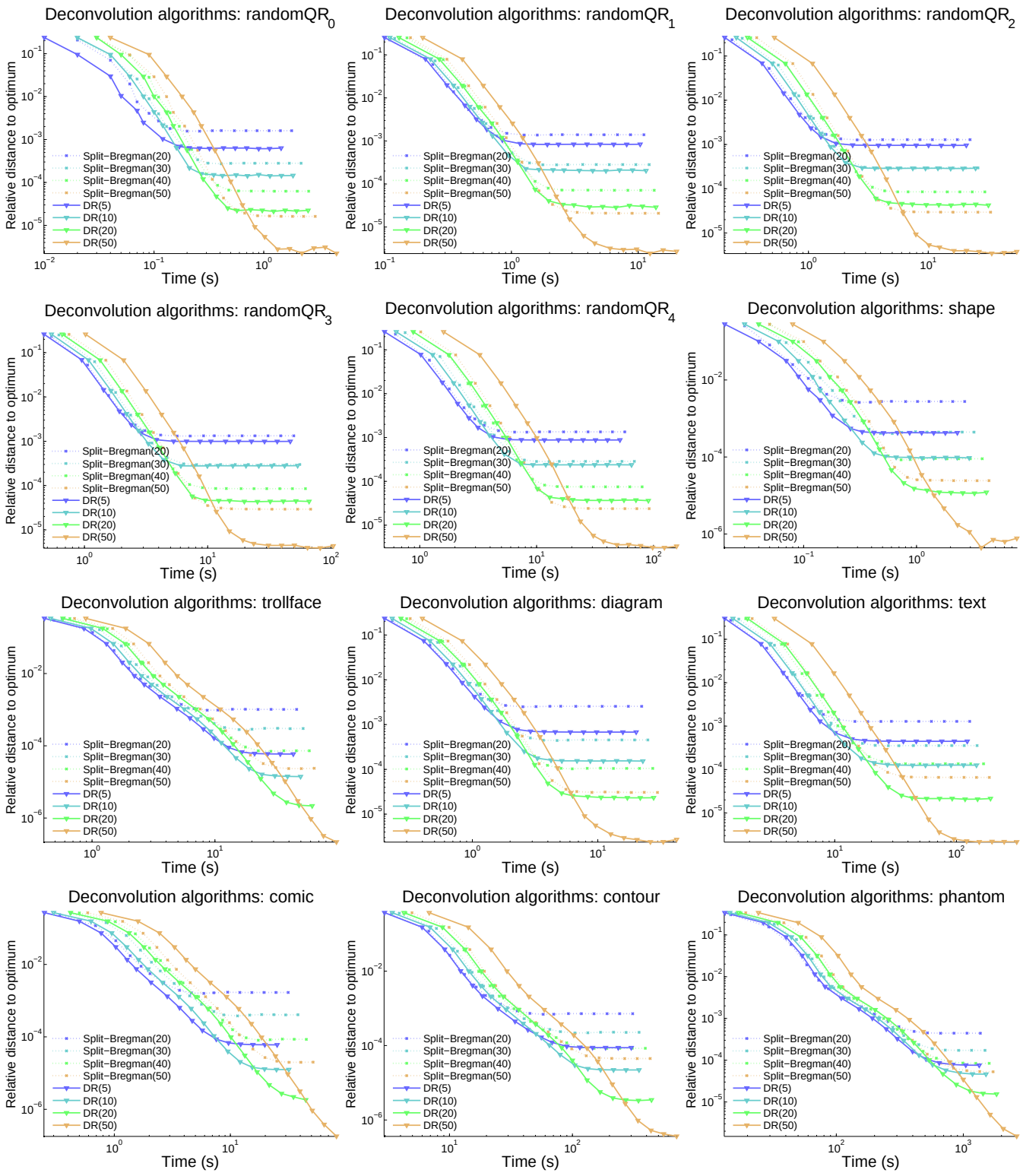

Figure 17: Relative distance to optimum vs time of the deconvolution 2D-TV algorithms under comparison, for the different images considered in the experiments.

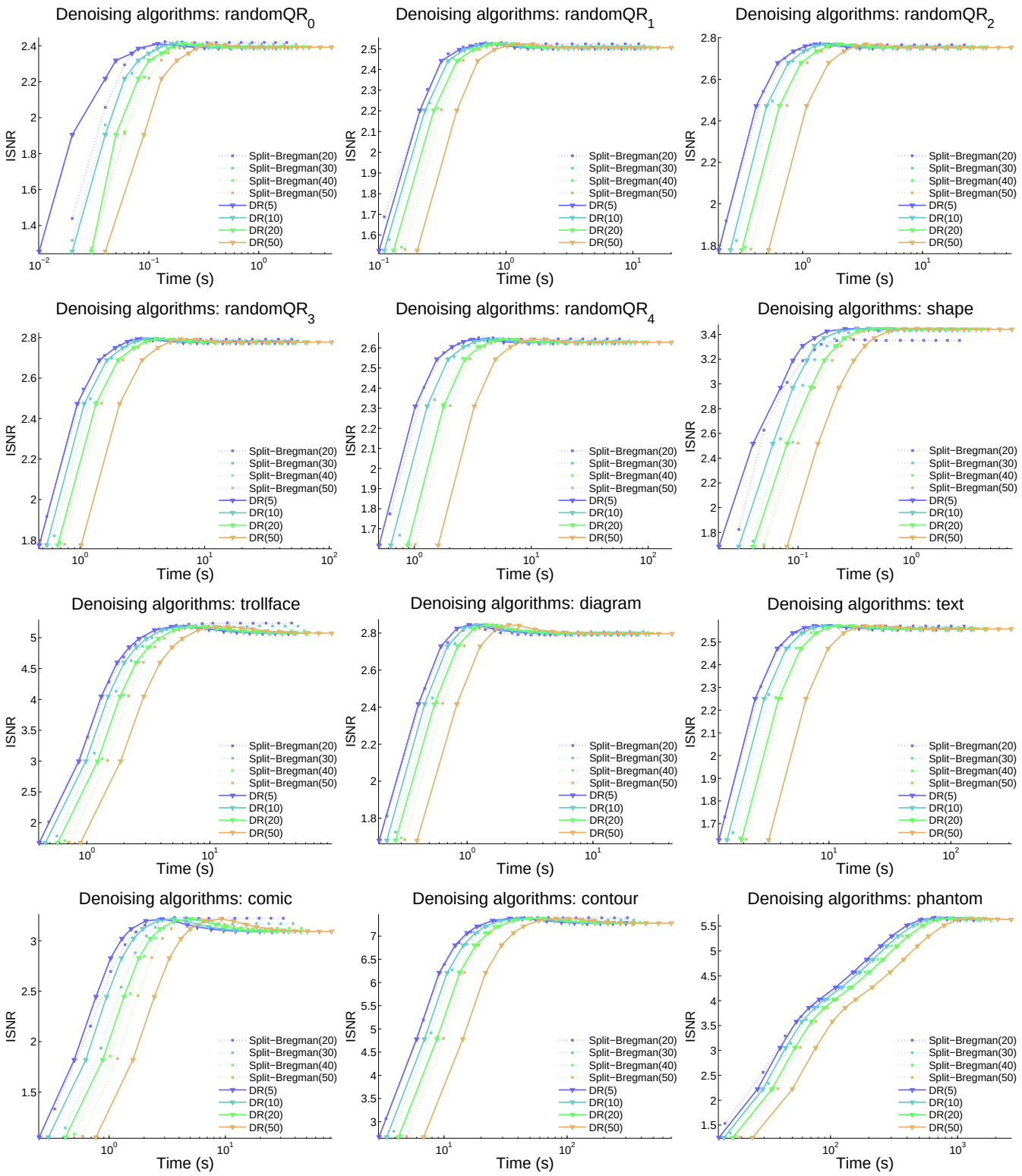

Figure 18: Increased Signal to Noise Ratio (ISNR) vs time of the deconvolution 2D-TV algorithms under comparison, for the different images considered in the experiments.

Image	Convolution	Parameters
randomQR	Motion	Length 5, Angle 35^o
shape	Average	Size 3×3
trollface	Disk	Radius 5
diagram	Motion	Length 5, Angle 0^o
text	Average	Size 1×10
comic	Gaussian	Size 15, Deviation 2
contour	Disk	Radius 5
phantom	Motion	Length 100, Angle 240^o

Table 4: Convolution kernels used for each test image. *Average* substitutes each pixel with the average of its surrounding $n \times m$ neighbors. *Disk* performs the same operation within a disk-shaped neighborhood of the shown radius. *Gaussian* uses a $n \times n$ neighborhood and assigns different weights to each neighbor following the value of a gaussian distribution of the indicated deviation centered at the current pixel. *Motion* emulates the distortions produced when taking a picture in motion, defining a neighborhood following a vector of the indicated length and angle.

5.3 2D Fused-Lasso Signal Approximator

The **Fused–Lasso Signal Approximator** (FLSA) [Friedman et al., 2007] can be regarded as a particular case of Fused-Lasso where the input matrix $\boldsymbol{A}$ is the identity matrix $\boldsymbol{I}$, i.e.,

$$\min_{\boldsymbol{x}} \quad \tfrac{1}{2}\|\boldsymbol{x} - \boldsymbol{y}\|_2^2 + \lambda_1\|\boldsymbol{x}\|_1 + \lambda_2 \mathrm{Tv}_1^{1\mathrm{D}}(\boldsymbol{x}).$$

This problem can be solved immediately using the methods presented in §4.6. A slightly less trivial problem is the one posed by the 2D variant of FLSA:

$$\min_{\boldsymbol{X}} \quad \tfrac{1}{2}\|\boldsymbol{X} - \boldsymbol{Y}\|_{\mathrm{F}}^2 + \lambda_1\|\mathrm{vec}(\boldsymbol{X})\|_1 + \lambda_2 \mathrm{Tv}_{1,1}^{2\mathrm{D}}(\boldsymbol{X}). \tag{5.4}$$

Friedman et al. [2007] used this model for denoising images where a large number of pixels are known to be completely black (intensity 0), which aligns well with the structure imposed by the ℓ_1 regularizer.

Akin to the 1D-case, 2D-FLSA (5.4) can also be solved by decomposing its computation into two prox operators [Friedman et al., 2007]; formally,

$$\mathrm{prox}_{\lambda_1\|\cdot\|_1 + \lambda_2 \mathrm{Tv}_{1,1}^{2\mathrm{D}}(\cdot)}(\boldsymbol{Y}) = \mathrm{prox}_{\lambda_1\|\cdot\|_1}\big(\mathrm{prox}_{\lambda_2 \mathrm{Tv}_{1,1}^{2\mathrm{D}}(\cdot)}(\boldsymbol{Y})\big).$$

Thus, to solve (5.4) we merely invoke our $\mathrm{Tv}_{1,1}^{2\mathrm{D}}$ prox operator and then apply soft-thresholding to the results. Since soft-thresholding is done in closed form, the performance of a 2D-FLSA solver depends only on its ability to compute $\mathrm{Tv}_{1,1}^{2\mathrm{D}}$-proximity efficiently. We can then safely claim that the results summarized in table 3 apply equivalently to 2D-FLSA, and so the proposed Douglas Rachford method performs best when reconstruction ISNR is the primary concern.

6 Application of multidimensional TV

We now apply our multidimensional TV regularizer to anisotropic filtering for **video denoising**. The extension to videos from images is natural. Say a video contains f frames of size $n \times m$ pixels; this video can be viewed as a 3D-tensor $\mathsf{X} \in \mathbb{R}^{n \times m \times f}$, on which a 3D-TV based filter can be effected by

$$\min_{\mathsf{X}} \quad \tfrac{1}{2}\|\mathsf{X} - \mathsf{U}_0\|_{\mathrm{F}}^2 + \lambda \mathrm{Tv}_{p_1,p_2,p_3}^{3\mathrm{D}}(\mathsf{X}), \tag{6.1}$$

Sequence	Frame resolution	Number of frames	Total number of pixels
salesman	288 × 352	50	5 million
coastguard	176 × 144	300	7.6 million
bicycle	720 × 576	30	12.4 million

Table 5: Size details of video sequences used in the video denoising experiments.

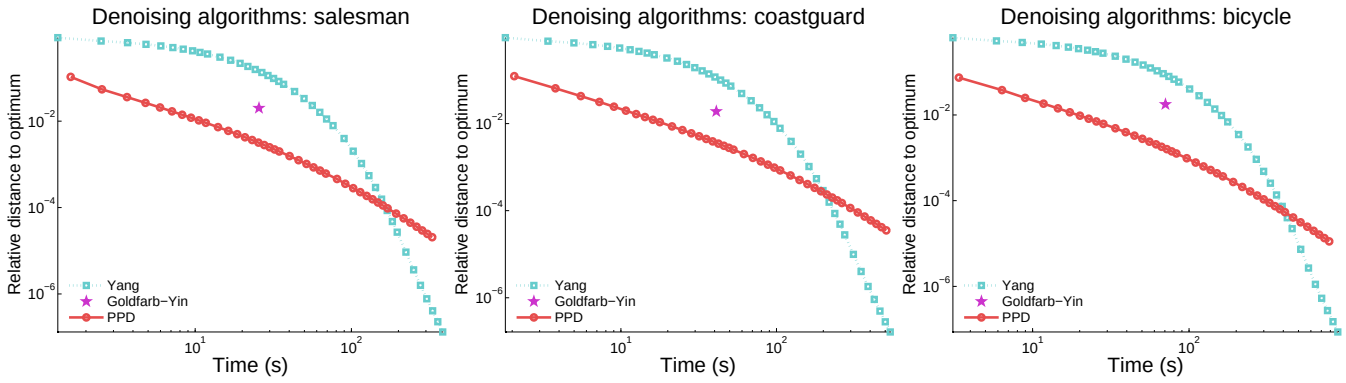

Figure 19: Relative distance to optimum vs time of the denoising 3D-TV algorithms under comparison, for the different video sequences considered in the experiments.

where U_0 is the observed noisy video, and $\mathrm{Tv}^{3\mathrm{D}}_{p_1,p_2,p_3} = \mathrm{Tv}^3_{\boldsymbol{p}}$ with $\boldsymbol{p} = [p_1, p_2, p_3]$. Application of the filter (6.1) is nothing but computation of the prox operator, which can be done using the Parallel-Proximal Dykstra (PPD) algorithm presented in Sec. 3.

We apply this idea to the video sequences detailed in Table 5. All of the sequences are made of grayscale pixels. Figure 26 in the Appendix shows some of the frames of the *salesman* sequence. We noise every frame of these sequences by applying gaussian noise with zero mean and variance 0.01, using Matlab's *imnoise* function. Then we solve problem 6.1 for each sequence, using PPD and adjusting the regularization value so as to maximize ISNR of the reconstructed signal. For comparison purposes we also test the following algorithms, which have been previously presented as good solvers for 3D-TV:

- The method by Yang et al. [2013], which was already proposed for multidimensional filtering. As this method requires providing a 1D-TV prox subroutine, for which we employ our presented taut-string method.
- The maximum flow approach by Goldfarb and Yin [2009], which features an implementation for 3D grids, thus solving a discrete-valued version of 3D-TV.

We must point out that other image denoising methods seem amenable for extension into the multidimensional setting, such as Condat's and Chambolle-Pock methods. However in the light of the image denoising results they do not seem a good choice for this problem. A more reasonable choice might be to extend Split-Bregman to multiple dimensions, but such an extension has not been implemented or proposed as far as we know. We would also like to note that we have considered extending the Douglas Rachford method to a multidimensional setting, however such task is complex and thus we decided to focus on Parallel Proximal Dykstra.

Similarly to our previous image denoising experiments, we ran the algorithms under comparison for each video sequence and measured its ISNR and relative distance to the optimal objective value of the

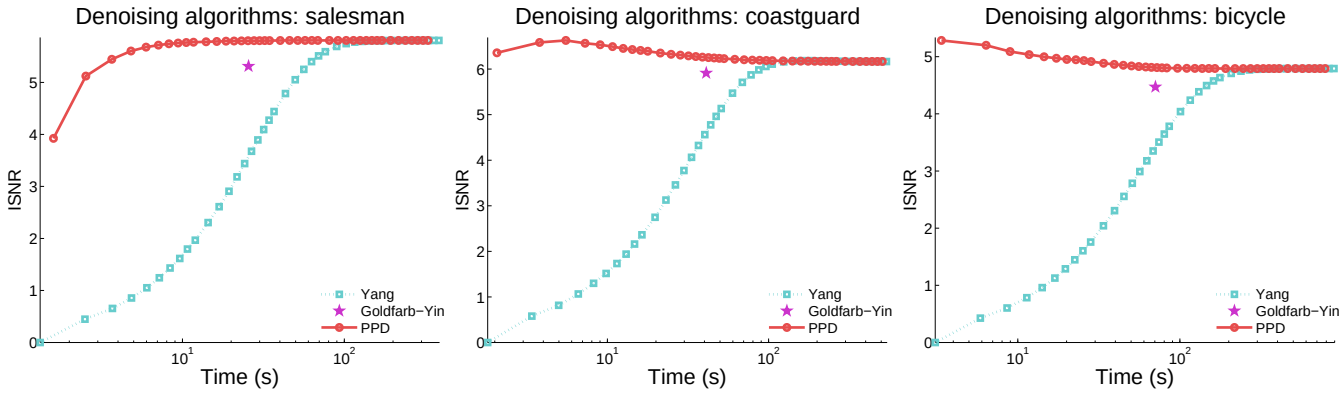

Figure 20: Increased Signal to Noise Ratio (ISNR) vs time of the denoising 3D-TV algorithms under comparison, for the different video sequences considered in the experiments.

current solution at each iteration through their execution. Again the exception is the Goldfarb-Yin method, which is non–iterative and so we only report the time required for its termination. The optimal objective value was estimated by running all methods for a very large number of iterations and taking the minimum value of them all. This produced the plots shown in Figures 19-20. From them the following observations are of relevance

- Following the pattern observed in the image denoising experiments, Yang's method is best suited for finding very accurate solutions.
- The method by Goldfarb and Yin again provides suboptimal solutions, due to the discrete approximation it uses.
- Parallel Proximal Dykstra is the fastest to achieve a mid-quality solution.
- Intermediate solutions prior to convergence of the PPD run result in better ISNR values for the *coastguard* and *bicycle* datasets. This hints that the denoising model used in this experiment may not be optimal for these kind of signals; indeed, more advanced denoising models abound in the signal processing literature. Hence we do not claim novel results in terms of ISNR quality, but just in solving this classic denoising model more efficiently.

The ISNR plots in Figure 20 also show how both Parallel Proximal Dykstra and Goldfarb-Yin converge to equivalent solutions in practice. Therefore, for the purpose of video denoising PPD seems to be the best choice, unless for some reason a high degree of accuracy is required, for which the method of Goldfarb and Yin should be preferred.

Acknowledgments

ÁB acknowledges partial financial support from Spain's TIN 2010-21575-C02-01. We thank R. Tibshirani for bringing [Johnson, 2013] to our attention, and S. Jegelka for alerting us to the importance of weighted total-variation problems.

References

M. V. Afonso, J. M. Bioucas-Dias, and M. A. T. Figueiredo. Fast image recovery using variable splitting and constrained optimization. *IEEE Transactions on Image Processing*, 19(9), September 2010.

C. M. Alaız, Á. Barbero, and J. R. Dorronsoro. Group fused lasso. *Artificial Neural Networks and Machine Learning–ICANN 2013*, page 66, 2013.

E. Anderson et al. *LAPACK Users' Guide*. Society for Industrial and Applied Mathematics, Philadelphia, PA, third edition, 1999. ISBN 0-89871-447-8 (paperback).

F. Bach. Structured sparsity-inducing norms through submodular functions. In *NIPS*, 2010.

F. Bach, R. Jenatton, J. Mairal, and G. Obozinski. Convex optimization with sparsity-inducing norms. In S. Sra, S. Nowozin, and S. J. Wright, editors, *Optimization for Machine Learning*. MIT Press, 2011.

Á. Barbero, J. López, and J. R. Dorronsoro. Finding Optimal Model Parameters by Discrete Grid Search. In *Advances in Soft Computing: Innovations in Hybrid Intelligent Systems 44*, pages 120–127. Springer, 2008.

Á. Barbero, J. López, and J. R. Dorronsoro. Finding Optimal Model Parameters by Deterministic and Annealed Focused Grid Search. *Neurocomputing*, 72(13-15):2824–2832, 2009. ISSN 0925-2312. doi: DOI:10.1016/j.neucom.2008.09.024.

H. H. Bauschke and P. L. Combettes. *Convex analysis and monotone operator theory in Hilbert spaces*. CMS Books in Mathematics. Springer, 2011.

A. Beck and M. Teboulle. A Fast Iterative Shrinkage-Thresholding Algorithm for Linear Inverse Problems. *SIAM Journal of Imgaging Sciences*, 2(1):183–202, 2009.

D. P. Bertsekas. Projected newton methods for optimization problems with simple constraints. *SIAM Journal on Control and Optimization*, 20(2), March 1982.

D. P. Bertsekas. *Nonlinear Programming*. Athena Scientific, 2nd edition, September 1999.

J. M. Bioucas-Dias and M. A. T. Figueiredo. A new twist: Two-step iterative shrinkage/thresholding algorithms for image restoration. *IEEE Transactions on Image Processing*, 16(12):2992–3004, December 2007.

J. M. Bioucas-Dias, M. A. T. Figueiredo, and J. P. Oliveira. Total variation-based image deconvolution: A majorization-minimization approach. In *ICASSP Proceedings*, 2006.

BM3D. Bm3d software and test sequences, 2013. URL http://www.cs.tut.fi/~foi/GCF-BM3D/.

R. H. Byrd, P. Lu, J. Nocedal, and C. Zhu. A limited memory algorithm for bound constrained optimization. Technical report, Northwestern University, 1994.

E. J. Candès and T. Tao. Near-optimal signal recovery from random projections: universal encoding strategies. *IEEE Trans. Info. Theory*, 52:5406–5425, 2004.

A. Chambolle and J. Darbon. On total variation minimization and surface evolution using parametric maximum flows. *International Journal of Computer Vision*, 84(3), 2009.

A. Chambolle and T. Pock. A first-order primal-dual algorithm for convex problems with applications to imaging. *Journal of Mathematical Imaging and Vision*, 40(1):120–145, 2011.

V. Chandrasekaran, B. Recht, P. A. Parrilo, and A. S. Willsky. The Convex Geometry of Linear Inverse Problems. *Foundations of Computational Mathematics*, 12(6), 2012.

R. Choksi, Y. van Gennip, and A. Oberman. Anisotropic Total Variation Regularized L1-Approximation and Denoising/Deblurring of 2D Bar Codes. Technical report, McGill University, July 2010.

P. L. Combettes. Iterative construction of the resolvent of a sum of maximal monotone operators. *Journal of Convex Analysis*, 16:727–748, 2009.

P. L. Combettes and J.-C. Pesquet. Proximal splitting methods in signal processing. *arXiv:0912.3522*, 2009.

L. Condat. A direct algorithm for 1d total variation denoising. Technical report, GREYC laboratory, CNRS-ENSICAEN-Univ. of Caen, 2012.

L. Condat. A generic proximal algorithm for convex optimization - application to total variation minimization. *IEEE SIGNAL PROC. LETTERS*, 21(8):985–989, 2014.

A. R. Conn, N. I. M. Gould, and P. L. Toint. *Trust-Region Methods*. SIAM, 2000.

J. Dahl, P. C. Hansen, S. H. Jensen, and T. L. Jensen. Algorithms and software for total variation image

reconstruction via first-order methods. *Numer Algor*, 53:67–92, 2010.

P. L. Davies and A. Kovac. Local extremes, runs, strings and multiresolution. *The Annals of Statistics*, 29(1):1–65, 2001.

Y. Duan and X.-C. Tai. Domain decomposition methods with graph cuts algorithms for total variation minimization. *Adv Comput Math*, 36:175–199, 2012. doi: 10.1007/s10444-011-9213-4.

J. Friedman, T. Hastie, H. Höfling, and R. Tibshirani. Pathwise coordinate optimization. *Annals of Applied Statistics*, 1(2):302–332, Aug. 2007.

D. Goldfarb and W. Yin. Parametric maximum flow algorithms for fast total variation minimization. *SIAM Journal on Scientific Computing*, 31(5):3712–3743, 2009.

O. S. Goldstein T. The Split Bregman Method for L1 Regularized Problems. *SIAM Journal on Imaging Sciences*, 2(2):323–343, 2009.

T. R. Golub et al. Molecular classification of cancer. *Science*, 286(5439):531–537, October 1999.

M. Grasmair. The equivalence of the taut string algorithm and bv-regularization. *Journal of Mathematical Imaging and Vision*, 27(1):59–66, 2007. ISSN 0924-9907. doi: 10.1007/s10851-006-9796-4. URL http://dx.doi.org/10.1007/s10851-006-9796-4.

Z. Harchaoui and C. Lévy-Leduc. Multiple Change-Point Estimation With a Total Variation Penalty. *Journal of the American Statistical Association*, 105(492):1480–1493, 2010.

J. Hua, W. D. Tembe, and E. R. Dougherty. Performance of feature-selection methods in the classification of high-dimension data. *Pattern Recognition*, 42:409–424, 2009.

K. Ito and K. Kunisch. An active set strategy based on the augmented lagrangian formulation for image restoration. *ESAIM: Mathematical Modelling and Numerical Analysis*, 33(1):1–21, 1999. URL http://eudml.org/doc/193911.

M. Jaggi. Revisiting frank-wolfe: Projection-free sparse convex optimization. In *Proceedings of the 30th International Conference on Machine Learning,*, 2013.

S. Jegelka, F. Bach, and S. Sra. Reflection methods for user-friendly submodular optimization. In *Advances in Neural Information Processing Systems*, 2013. To appear.

N. A. Johnson. A dynamic programming algorithm for the fused Lasso and l_0-segmentation. *J. Computational and Graphical Statistics*, 2013.

D. Kim, S. Sra, and I. Dhillon. A scalable trust-region algorithm with application to mixed-norm regression. In *International Conference on Machine Learning*, 2010.

S. Kim, K. Koh, S. Boyd, and D. Gorinevsky. ℓ_1 trend filtering. *SIAM Review*, 51(2):339–360, 2009. doi: 10.1137/070690274.

K. C. Kiwiel. Variable fixing algorithms for the continuous quadratic knapsack problem. *J. Optim. Theory Appl.*, 136:445–458, 2008.

M. Kolar, L. Song, A. Ahmed, and E. Xing. Estimaging time-varying networks. *The Annals of Applied Statistics*, 4(1):94–123, 2010.

D. Krishnan and R. Fergus. Fast image deconvolution using hyper-laplacian priors. In *Advances in Neural Information Processing Systems*, 2009.

S. R. Land and J. H. Friedman. Variable fusion: A new adaptive signal regression method. Technical Report 656, Department of Statistics, Carnegie Mellon University Pittsburgh, 1997.

Y. Li and F. Santosa. A computational algorithm for minimizing total variation in image restoration. *IEEE Transactions on Image Processing*, 5(6):987–995, 1996. URL http://dblp.uni-trier.de/db/journals/tip/tip5.html#LiS96.

C.-J. Lin and J. J. Moré. Newton's method for large bound-constrained optimization problems. *SIAM Journal on Optimization*, 9(4):1100–1127, 1999.

H. Liu and J. Zhang. Estimation Consistency of the Group Lasso and its Applications. In *Int. Conf. Mach. Learning (ICML)*, 2009.

J. Liu and J. Ye. Efficient Euclidean projections in linear time. In *ICML*, Jun. 2009.

J. Liu, S. Ji, and J. Ye. *SLEP: Sparse Learning with Efficient Projections*. Arizona State University, 2009. *http://www.public.asu.edu/ jye02/Software/SLEP*.

J. Liu, L. Yuan, and J. Ye. An efficient algorithm for a class of fused lasso problems. In *ACM SIGKDD Conference on Knowledge Discovery and Data Mining*, 2010.

J. Mairal, R. Jenatton, G. Obozinski, and F. Bach. Network Flow Algorithms for Structured Sparsity. In *NIPS*, 2010. To appear.

B. Martinet. Régularisation d'inéquations variationnelles par approximations successives. *Modélisation Mathématique et Analyse Numérique*, 4(R3):154–158, 1970.

L. Meier, S. van de Geer, and P. Bühlmann. The group lasso for logistic regression. *J. R. Statist. Soc.*, 70:53–71, 2008.

J. J. Moré and D. C. Sorensen. Computing a trust region step. *SIAM Journal of Scientific Computing*, 4(3), September 1983.

J. J. Moreau. Fonctions convexes duales et points proximaux dans un espace hilbertien. *C. R. Acad. Sci. Paris Sér. A Math.*, 255:2897–2899, 1962.

Y. Nesterov. Gradient methods for minimizing composite objective function. Technical Report 76, Catholic University of Louvain, CORE, 2007.

J. Nocedal and S. J. Wright. *Numerical Optimization*. Springer Verlag, 2000.

G. Pierra. Decomposition through formalization in a product space. *Mathematical Programming*, 28(1): 96–115, 1984.

C. Pontow and O. Scherzer. A derivative free approach for total variation regularization. *arXiv:0911.1293*, 2009. URL http://arxiv.org/abs/0911.1293.

A. Ramdas and R. J. Tibshirani. Fast and flexible admm algorithms for trend filtering. *arXiv:1406.2082*, 2014.

F. Rapaport and E. B. J.-P. Vert. Classification of arrayCGH data using fused SVM. *Bioinformatics*, 24 (13):i375–i382, 2008.

A. Rinaldo. Properties and refinements of the fused lasso. *Annals of Statistics*, 37(5B):2922–2952, 2009.

R. T. Rockafellar. Monotone operators and hte proximal point algorithm. *SIAM J. Control and Opt.*, 14 (5):877–898, 1976.

S. Rogers, M. Girolami, C. Campbell, and R. Breitling. The latent process decomposition of cdna microarray data sets. *IEEE/ACM Trans. Comp. Bio. and Bioinformatics*, 2(2), April-June 2005.

L. I. Rudin, S. Osher, and E. Fatemi. Nonlinear total variation based noise removal algorithms. *Physica D*, 60:259–268, 1992.

S. Salzo and S. Villa. Inexact and accelerated proximal point algorithms. *J. Convex Analysis*, 19(4), 2012.

M. Schmidt, N. L. Roux, and F. Bach. Convergence Rates of Inexact Proximal-Gradient Methods for Convex Optimization. In *Advances in Neural Information Processing Systems (NIPS)*, 2011.

S. Sra. Scalable nonconvex inexact proximal splitting. In *Advances in Neural Information Processing Systems*, 2012.

S. Sra, S. Nowozin, and S. Wright, editors. *Optimization for machine learning*. MIT Press, 2011.

G. Steidl, S. Didas, and J. Neumann. Relations between higher order tv regularization and support vector regression. In *Scale-Space*, pages 515–527, 2005.

N. Stransky et al. Regional copy number-independent deregulation of transcription in cancer. *Nature Genetics*, 38(12):1386–1396, December 2006.

R. Tibshirani. Regression shrinkage and selection via the lasso. *J. R. Statist. Soc.*, 58(1):267–288, 1996.

R. Tibshirani and P. Wang. Spatial smoothing and hot spot detection for CGH data using the fused lasso. *Biostatistics*, 9(1):18–29, 2008.

R. Tibshirani, M. Saunders, S. Rosset, J. Zhu, and K. Knight. Sparsity and smoothness via the fused lasso. *J. Royal Stat. Soc.: Series B*, 67(1):91–108, 2005.

R. J. Tibshirani. Adaptive piecewise polynomial estimation via trend filtering. *The Annals of Statistics*, 42(1):285–323, 02 2014. doi: 10.1214/13-AOS1189.

U. Alon et al. Broad patterns of gene expression revealed by clustering analysis of tumor and normal colon tissues probed by oligonucleotide arrays. *Proc. Natl. Acad. Sci. USA*, 96:6745–6750, June 1999.

J.-P. Vert and K. Bleakley. Fast detection of multiple change-points shared by many signals using group LARS. In *Advances in Neural Information Processing Systems*, 2010.

C. R. Vogel and M. E. Oman. Iterative methods for total variation denoising. *SIAM Journal on Scientific Computing*, 17(1):227–238, 1996.

B. Wahlberg, S. Boyd, M. Annergren, and Y. Wang. An ADMM Algorithm for a Class of Total Variation Regularized Estimation Problems. In *Proceedings 16th IFAC Symposium on System Identification*, volume 16, 2012.

S. J. Wright, R. D. Nowak, and M. A. T. Figueiredo. Sparse reconstruction by separable approximation. *IEEE Trans. Sig. Proc.*, 57(7):2479–2493, 2009.

M. Wytock, S. Sra, and J. Z. Kolter. Fast Newton Methods for the Group Fused Lasso. In *Conference on Uncertainty in Artificial Intelligence*, 2014.

S. Yang, J. Wang, W. Fan, X. Zhang, P. Wonka, and J. Ye. An Efficient ADMM Algorithm for Multi-dimensional Anisotropic Total Variation Regularization Problems. In *ACM Knowledge Discovery and Data Mining (KDD)*, Chicago, Illinois, USA, August 2013.

Y. Yu. On decomposing the proximal map. In *Advances in Neural Information Processing Systems*, 2013.

M. Yuan and Y. Lin. Model Selection and Estimation in Regression with Grouped Variables. *J. R. Statist. Soc. B*, 68(1):49–67, 2006.

M. Zhu and T. Chan. An efficient primal-dual hybrid gradient algorithm for total variation image restoration. Technical report, UCLA CAM, 2008.

A Mathematical background

We begin by recalling a few basic ideas from convex analysis; we recommend the recent book [Bauschke and Combettes, 2011] for more details.

Let $\mathcal{X} \subset \mathbb{R}^n$ be any set. A function $r : \mathcal{X} \to \mathbb{R} \cup \{-\infty, +\infty\}$ is called *lower semicontinuous* if for every $\boldsymbol{x} \in \mathcal{X}$ and a sequence $(\boldsymbol{x}_k)$ that converges to $\boldsymbol{x}$, it holds that

$$\boldsymbol{x}_k \to \boldsymbol{x} \implies r(\boldsymbol{x}) \leq \liminf_k r(\boldsymbol{x}_k). \tag{A.1}$$

The set of proper lsc convex functions on $\mathcal{X}$ is denoted by $\Gamma_0(\mathcal{X})$ (such functions are also called *closed convex functions*). The *indicator function* of a set C is defined as

$$\delta_C : \mathcal{X} \to [0, \infty] : \boldsymbol{x} \mapsto \begin{cases} 0, & \text{if } \boldsymbol{x} \in C; \\ \infty, & \text{if } \boldsymbol{x} \notin C, \end{cases} \tag{A.2}$$

which is lsc if and only if C is closed.

The *convex conjugate* of r is given by $r^*(\boldsymbol{z}) := \sup_{\boldsymbol{x} \in \operatorname{dom} r} \ \langle \boldsymbol{x}, \boldsymbol{z} \rangle - r(\boldsymbol{x})$, and a particularly important example is the Fenchel conjugate of a norm $\|\cdot\|$

$$\text{if } r = \|\cdot\|, \quad \text{then } \ r^* = \delta_{\|\cdot\|_* \leq 1}, \tag{A.3}$$

where the norm $\|\cdot\|_*$ is dual to $\|\cdot\|$. Let r and h be proper convex functions. The *infimal convolution* of r with h is the convex function given by $(r \,\square\, h)(\boldsymbol{x}) := \inf_{\boldsymbol{y} \in \mathcal{X}} \big(r(\boldsymbol{y}) + h(\boldsymbol{x} - \boldsymbol{y})\big)$. For our purposes, the most important special case is infimal convolution of a convex function with the squared euclidean norm, which yields the *Moreau envelope* [Moreau, 1962].

Proposition A.1. *Let $r \in \Gamma_0(\mathcal{X})$ and let $\gamma > 0$. The* Moreau envelope *of r indexed by γ is*

$$E_r^\gamma(\cdot) := r \,\square\, (\tfrac{1}{2\gamma}\|\cdot\|_2^2). \tag{A.4}$$

The Moreau envelope (A.4) is convex, real-valued, and continuous.

Proof. See e.g. [Bauschke and Combettes, 2011, Prop. 12.15]. □

Using the Moreau envelope (A.4), we now formally introduce prox operators.

Definition A.2 (Prox operator)**.** *Let $r \in \Gamma_0(\mathcal{X})$, and let $\boldsymbol{y} \in \mathcal{X}$. Then $\operatorname{prox}_r \boldsymbol{y}$ is the unique point in $\mathcal{X}$ that satisfies $E_r^1(\boldsymbol{y}) = \min_{\boldsymbol{x}\in\mathcal{X}}(r(\boldsymbol{x}) + \frac{1}{2}\|\boldsymbol{x}-\boldsymbol{y}\|_2^2)$, i.e.,*

$$\operatorname{prox}_r(\boldsymbol{y}) := \operatorname*{argmin}_{\boldsymbol{x}\in\mathcal{X}} r(\boldsymbol{x}) + \tfrac{1}{2}\|\boldsymbol{x}-\boldsymbol{y}\|_2^2, \tag{A.5}$$

and the nonlinear map $\operatorname{prox}_r : \mathcal{X} \to \mathcal{X}$ is called the prox operator *of r.*

Sometimes the Fenchel conjugate r^* is easier to use than r; similarly, sometimes the operator $\operatorname{prox}_{r^*}$ is easier to compute than prox_r. The result below shows the connection.

Proposition A.3 (Moreau decomposition)**.** *Let $r \in \Gamma_0(\mathcal{X})$, $\gamma > 0$, and $\boldsymbol{y} \in \mathcal{X}$. Then,*

$$\boldsymbol{y} = \operatorname{prox}_{\gamma r}\boldsymbol{y} + \gamma \operatorname{prox}_{r^*/\gamma}(\gamma^{-1}\boldsymbol{y}). \tag{A.6}$$

Proof. A brief exercise; see e.g., [Bauschke and Combettes, 2011, Thm. 14.3]. □

This decomposition provides the necessary tools to exploit useful primal–dual relations. For the sake of clarity we also present a last result regarding a particular primal-dual relation that plays a key role in our algorithms.

Proposition A.4. *Let $f \in \Gamma_0(\mathcal{X})$ and $r \in \Gamma_0(\mathcal{Z})$. The problems below form a primal-dual pair.*

$$\inf_{\boldsymbol{x}\in\mathcal{X}} \quad f(\boldsymbol{x}) + r(\boldsymbol{B}\boldsymbol{x}) \quad \text{s.t.} \quad \boldsymbol{B}\boldsymbol{x} \in \mathcal{Z} \tag{A.7}$$

$$\inf_{\boldsymbol{u}\in\mathcal{Z}} \quad f^*(-\boldsymbol{B}^T\boldsymbol{u}) + r^*(\boldsymbol{u}). \tag{A.8}$$

Proof. Introduce an extra variable $\boldsymbol{z} = \boldsymbol{B}\boldsymbol{x}$, so that the dual function is

$$g(\boldsymbol{u}) = \inf_{\boldsymbol{x}\in\mathcal{X}} \; f(\boldsymbol{x}) + \boldsymbol{u}^T\boldsymbol{B}\boldsymbol{x} + \inf_{\boldsymbol{z}\in\mathcal{Z}} \; r(\boldsymbol{z}) - \boldsymbol{u}^T\boldsymbol{z},$$

which upon rewriting using Fenchel conjugates yields (A.8). □

B proxTV toolbox

All the Total–Variation proximity solvers in this paper have been implemented as the **proxTV** toolbox, available at https://github.com/albarji/proxTV. The toolbox has been designed to be used out of the box in a user friendly way; the top–level Matlab function `TV` solves Total–Variation proximity for a given signal under a variety of settings. For instance

```
>> TV(X, lambda)
```

solves Tv_1 proximity for a signal `X` of any dimension and a regularization value `lambda`. The weighted version of this problem is also seamlessly tackled by just providing a vector of weights of the appropriate length as the `lambda` parameter.

If a third parameter `p` is provided as

>> TV(X, lambda , p)

the general Tv_p proximity problem is addressed, whereupon an adequate solver is chosen by the library.

More advanced uses of the library are possible, allowing to specify which norm `p` and regularizer `lambda` values to use for each dimension of the signal, and even applying combinations of several different Tv_p regularizers along the same dimension. Please refer to the documentation within the toolbox for further information.

C Proof on the equality of taut-string problems

Theorem C.1 (Equality of taut-string problems)**.** *Given the problems*

$$\min_{\boldsymbol{s}} \sum_{i=1}^{n} (\boldsymbol{s}_i - \boldsymbol{s}_{i-1})^2 \,, \;\; s.t. \;\; |\boldsymbol{s}_i - \boldsymbol{r}_i| \leq \boldsymbol{w}_i \, \forall i = 1, \ldots, n-1 \,, \boldsymbol{s}_0 = 0, \boldsymbol{s}_n = \boldsymbol{r}_n, \tag{C.1}$$

and

$$\min_{\hat{\boldsymbol{s}}} \sum_{i=1}^{n} \sqrt{1 + (\hat{\boldsymbol{s}}_i - \hat{\boldsymbol{s}}_{i-1})^2}, \;\; s.t. \;\; |\hat{\boldsymbol{s}}_i - \boldsymbol{r}_i| \leq \boldsymbol{w}_i \, \forall i = 1, \ldots, n-1 \,, \hat{\boldsymbol{s}}_0 = 0, \hat{\boldsymbol{s}}_n = \boldsymbol{r}_n, \tag{C.2}$$

for a non-zero vectors $\boldsymbol{w}$, both problems share the same minimum $\boldsymbol{s}^* = \hat{\boldsymbol{s}}^*$.

Proof. The Lagrangian of problem C.1 takes the form

$$L(\boldsymbol{s}, \boldsymbol{\alpha}, \boldsymbol{\beta}) = \sum_{i=1}^{n} (\boldsymbol{s}_i - \boldsymbol{s}_{i-1})^2 + \sum_{i=1}^{n-1} \boldsymbol{\alpha}_i (\boldsymbol{s}_i - \boldsymbol{r}_i - \boldsymbol{w}_i) + \sum_{i=1}^{n-1} \boldsymbol{\beta}_i (-\boldsymbol{w}_i - \boldsymbol{s}_i + \boldsymbol{r}_i),$$

and its Karush-Kuhn-Tucker optimality conditions are given by

$$(\boldsymbol{s}_{i+1} - \boldsymbol{s}_i) - (\boldsymbol{s}_i - \boldsymbol{s}_{i-1}) = \boldsymbol{\alpha}_i - \boldsymbol{\beta}_i, \tag{C.3}$$

$$|\boldsymbol{s}_i - \boldsymbol{r}_i| \leq \boldsymbol{w}_i, \tag{C.4}$$

$$\boldsymbol{\alpha}_i, \boldsymbol{\beta}_i \geq 0, \tag{C.5}$$

$$\boldsymbol{\alpha}_i (\boldsymbol{s}_i - \boldsymbol{r}_i - \boldsymbol{w}_i) = 0, \tag{C.6}$$

$$\boldsymbol{\beta}_i (-\boldsymbol{w}_i - \boldsymbol{s}_i + \boldsymbol{r}_i) = 0, \tag{C.7}$$

$\forall i = 1, \ldots, n-1$, and where the first equation comes from the fact that $\frac{\partial L(\boldsymbol{s}, \boldsymbol{\alpha}, \boldsymbol{\beta})}{\partial \boldsymbol{s}} = 0$ at the minimum.

As the only difference between problems C.1 and C.2 is in the form of the objective, the KKT conditions for problem C.2 take the same form, but for the first one,

$$\frac{(\hat{\boldsymbol{s}}_{i+1} - \hat{\boldsymbol{s}}_i)}{\sqrt{1 + (\hat{\boldsymbol{s}}_{i+1} - \hat{\boldsymbol{s}}_i)^2}} - \frac{(\hat{\boldsymbol{s}}_i - \hat{\boldsymbol{s}}_{i-1})}{\sqrt{1 + (\hat{\boldsymbol{s}}_i - \hat{\boldsymbol{s}}_{i-1})^2}} = \hat{\boldsymbol{\alpha}}_i - \hat{\boldsymbol{\beta}}_i, \tag{C.8}$$

$$|\hat{\boldsymbol{s}}_i - \boldsymbol{r}_i| \leq \boldsymbol{w}_i, \tag{C.9}$$

$$\hat{\boldsymbol{\alpha}}_i, \hat{\boldsymbol{\beta}}_i \geq 0, \tag{C.10}$$

$$\hat{\boldsymbol{\alpha}}_i (\hat{\boldsymbol{s}}_i - \boldsymbol{r}_i - \boldsymbol{w}_i) = 0, \tag{C.11}$$

$$\hat{\boldsymbol{\beta}}_i (-\boldsymbol{w}_i - \hat{\boldsymbol{s}}_i + \boldsymbol{r}_i) = 0, \tag{C.12}$$

$\forall i = 1, \ldots, n-1$, and where we use hat notation for the dual coefficients to tell them apart from those of problem C.1.

Suppose $\boldsymbol{s}^*$ minimizer to problem C.1, hence fulfilling the conditions C.3-C.7. In particular this means that it is feasible to assign values to the dual coefficients $\boldsymbol{\alpha}, \boldsymbol{\beta}$ in such a way that the conditions above are met. If we set $\hat{\boldsymbol{s}} = \boldsymbol{s}^*$ in the conditions C.8-C.12 the following observations are of relevance

- Condition C.9 becomes the same as condition C.4, and so it is immediately met.
- The operator $f(x) = \frac{x}{\sqrt{1+x^2}}$ is contractive and monotonous.
- The couple $(\boldsymbol{\alpha}_i, \boldsymbol{\beta}_i)$ cannot be both zero at the same time, since $\boldsymbol{\alpha}_i > 0$ enforces $\boldsymbol{s}_i = \boldsymbol{r}_i + \boldsymbol{w}_i$ and $\boldsymbol{\beta}_i > 0$ enforces $\boldsymbol{s}_i = \boldsymbol{r}_i - \boldsymbol{w}_i$.
- Hence and because $\boldsymbol{\alpha}_i, \boldsymbol{\beta}_i \geq 0$ and condition C.3 holds, when $(\boldsymbol{s}_{i+1} - \boldsymbol{s}_i) - (\boldsymbol{s}_i - \boldsymbol{s}_{i-1}) > 0$ then $\boldsymbol{\alpha}_i > 0$, $\boldsymbol{\beta}_i = 0$, and when $(\boldsymbol{s}_{i+1} - \boldsymbol{s}_i) - (\boldsymbol{s}_i - \boldsymbol{s}_{i-1}) < 0$ then $\boldsymbol{\alpha}_i = 0$, $\boldsymbol{\beta}_i > 0$.
- $f(\boldsymbol{s}_{i+1} - \boldsymbol{s}_i) - f(\boldsymbol{s}_i - \boldsymbol{s}_{i-1})$ has the same sign as $(\boldsymbol{s}_{i+1} - \boldsymbol{s}_i) - (\boldsymbol{s}_i - \boldsymbol{s}_{i-1})$, since f is monotonous and as such preserves ordering.
- Since f is contractive, condition C.8 can be met by setting $(\hat{\boldsymbol{\alpha}}_i, \hat{\boldsymbol{\beta}}_i) = (k\boldsymbol{\alpha}_i, k\boldsymbol{\beta}_i)$ for some $0 \leq k < 1$. Note that this works because $(\boldsymbol{\alpha}_i, \boldsymbol{\beta}_i)$ cannot be both zero at the same time.
- Condition C.10 is met for those choices of $\hat{\boldsymbol{\alpha}}_i, \hat{\boldsymbol{\beta}}_i$, as C.5 was met for $\boldsymbol{\alpha}_i, \boldsymbol{\beta}_i$ and $0 \leq k < 1$.
- Conditions C.11 and C.12 are also met for those choices of $\hat{\boldsymbol{\alpha}}_i, \hat{\boldsymbol{\beta}}_i$, as $\hat{\boldsymbol{\alpha}}_i(\boldsymbol{s}_i - \boldsymbol{r}_i - \boldsymbol{w}_i) = k\boldsymbol{\alpha}_i(\boldsymbol{s}_i - \boldsymbol{r}_i - \boldsymbol{w}_i) = 0$ and $\hat{\boldsymbol{\beta}}_i(-\boldsymbol{w}_i - \boldsymbol{s}_i + \boldsymbol{r}_i) = k\boldsymbol{\beta}_i(-\boldsymbol{w}_i - \boldsymbol{s}_i + \boldsymbol{r}_i) = 0$.

Therefore, all of the optimality conditions C.8-C.12 for problem C.2 are met for $\boldsymbol{s}^*$ solution of problem C.1, and so a minimum of problem C.1 is also a minimum for problem C.2.

The proof can be repeated the other way round by setting $\boldsymbol{s} = \hat{\boldsymbol{s}}^*$ optimal for problem C.2, defining the operator $f^{-1}(x) = \frac{x}{\sqrt{1-x^2}}$, and observing that this operator is monotonous and expansive, so we can establish $(\boldsymbol{\alpha}_i, \boldsymbol{\beta}_i) = (k\hat{\boldsymbol{\alpha}}_i, k\hat{\boldsymbol{\beta}}_i)$ for some $k \geq 1$ and the optimality conditions C.3-C.7 for problem C.1 are met following a similar reasoning to the one presented above. Thus, a minimum for problem C.2 is also a minimum for problem C.1, which joined with the previous result completes the proof.

□

D Testing images and videos, and experimental results

The images used in the experiments are displayed in what follows, along with their noisy/denoised and convoluted/deconvoluted versions for each algorithm tested. QR barcode images were generated by encoding random text using Google chart API[5]. Images *shape* and *phantom* [6] are publicly available and frequently used in image processing. *trollface* and *comic* [7] are also publicly available. *gaudi*, used in the multicore experiments, is a high resolution 3197×3361 photograph of Gaudi's Casa Batlló[8]. The rest of the images were originally created by the authors.

For the video experiments, the *salesman* sequence was used, which is publicly available at BM3D [2013]. Frames from the video are displayed in what follows, along with their noisy/denoised versions.

[5] http://code.google.com/intl/en-EN/apis/chart/
[6] Extracted from http://en.wikipedia.org/wiki/File:Shepp_logan.png
[7] Author: Francisco Molina. http://www.afrikislife.net/english/
[8] Extracted from http://www.flickr.com/photos/jeffschwartz/202423023/

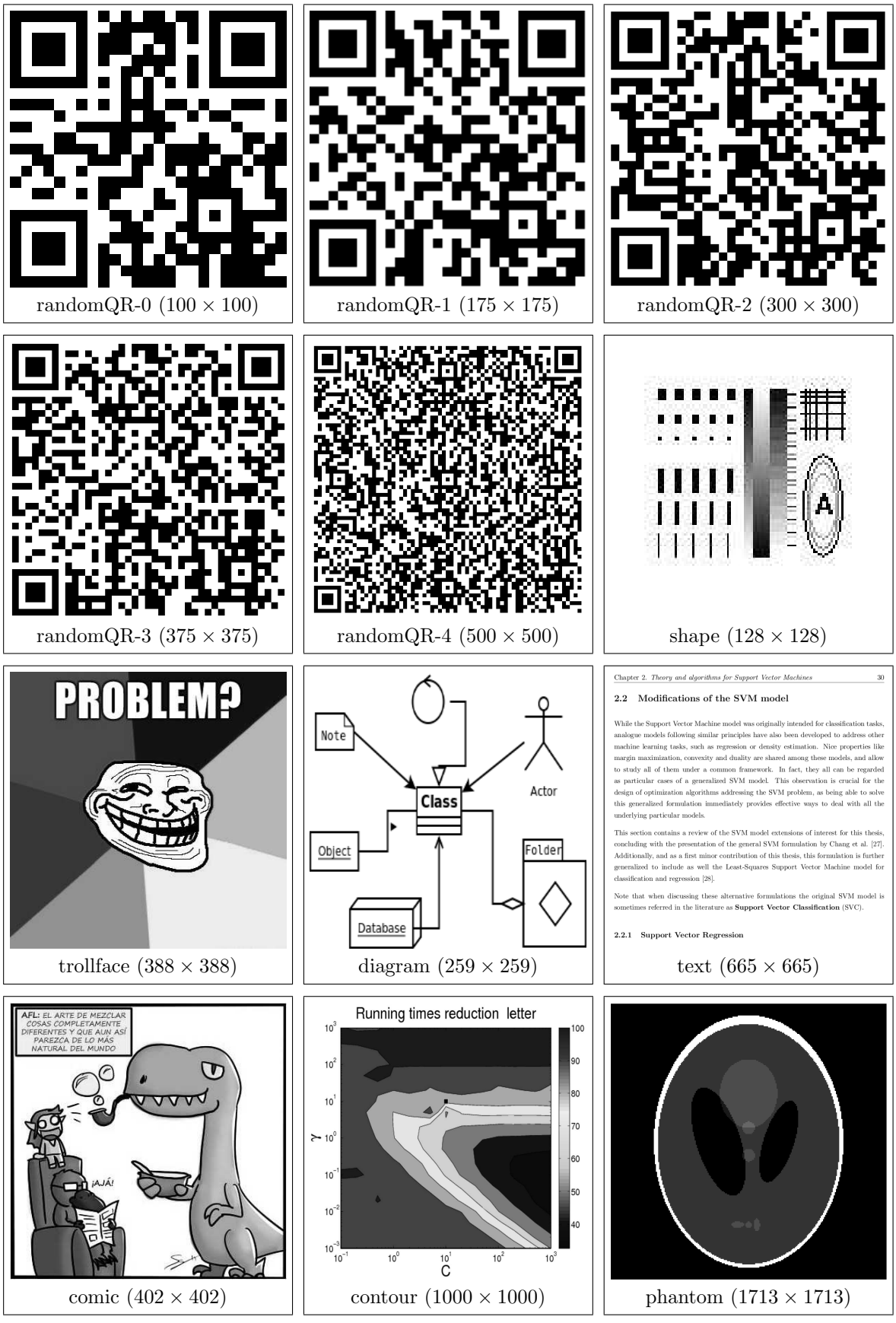
randomQR-0 (100 × 100)
randomQR-1 (175 × 175)
randomQR-2 (300 × 300)
randomQR-3 (375 × 375)
randomQR-4 (500 × 500)
shape (128 × 128)
A
PROBLEM?
trollface (388 × 388)
Note
Actor
Class
Object
Folder
Database
diagram (259 × 259)
Chapter 2. Theory and algorithms for Support Vector Machines 30
2.2 Modifications of the SVM model
While the Support Vector Machine model was originally intended for classification tasks, analogue models following similar principles have also been developed to address other machine learning tasks, such as regression or density estimation. Nice properties like margin maximization, convexity and duality are shared among these models, and allow to study all of them under a common framework. In fact, they all can be regarded as particular cases of a generalized SVM model. This observation is crucial for the design of optimization algorithms addressing the SVM problem, as being able to solve this generalized formulation immediately provides effective ways to deal with all the underlying particular models.
This section contains a review of the SVM model extensions of interest for this thesis, concluding with the presentation of the general SVM formulation by Chang et al. [27]. Additionally, and as a first minor contribution of this thesis, this formulation is further generalized to include as well the Least-Squares Support Vector Machine model for classification and regression [28].
Note that when discussing these alternative formulations the original SVM model is sometimes referred in the literature as Support Vector Classification (SVC).
2.2.1 Support Vector Regression
text (665 × 665)
AFL: EL ARTE DE MEZCLAR COSAS COMPLETAMENTE DIFERENTES Y QUE AUN ASÍ PAREZCA DE LO MÁS NATURAL DEL MUNDO
¡AJÁ!
comic (402 × 402)
Running times reduction letter
γ
C
contour (1000 × 1000)
phantom (1713 × 1713)

Figure 21: Test images used in the experiments together with their sizes in pixels. Images displayed have been scaled down to fit in page.

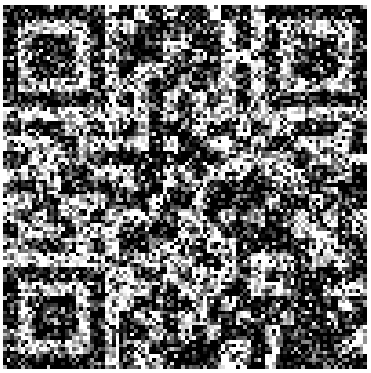

randomQR-0 (100 × 100)

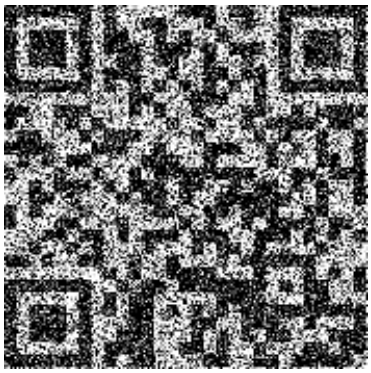

randomQR-1 (175 × 175)

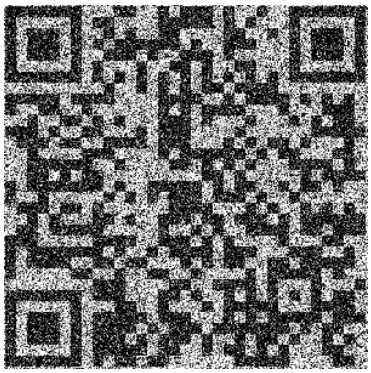

randomQR-2 (300 × 300)

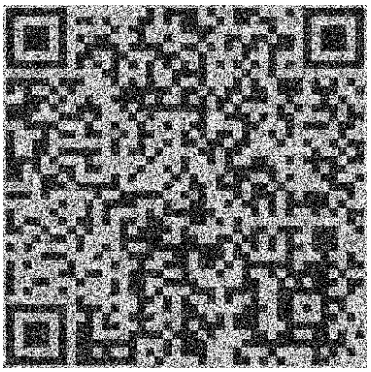

randomQR-3 (375 × 375)

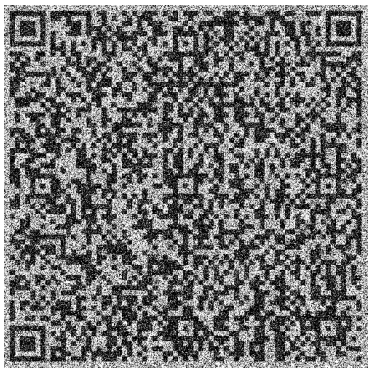

randomQR-4 (500 × 500)

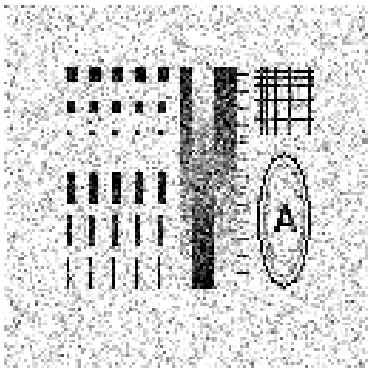

shape (128 × 128)

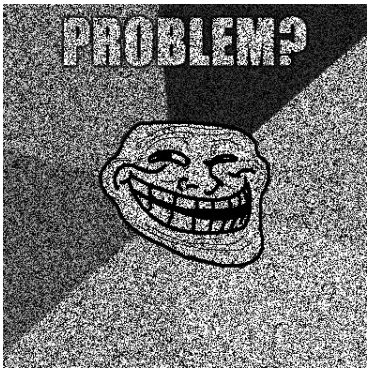

trollface (388 × 388)

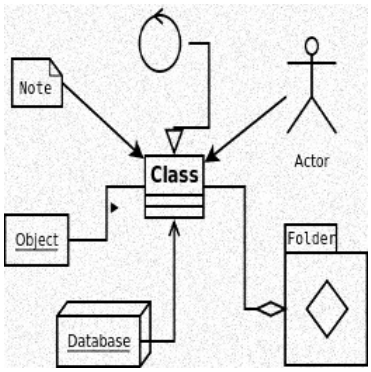

diagram (259 × 259)

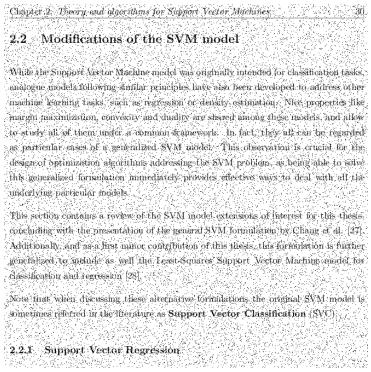

Chapter 2. Theory and algorithms for Support Vector Machines 30

2.2 Modifications of the SVM model

While the Support Vector Machine model was originally intended for classification tasks, analogous models following similar principles have also been developed to address other machine learning tasks, such as regression or density estimation. Nice properties like margin maximization, convexity and duality are shared among those models, and allow to study all of them under a common framework. In fact, they all can be regarded as particular cases of a generalized SVM model. This observation is crucial for the design of optimization algorithms addressing the SVM problem, as being able to solve this generalized formulation immediately provides effective ways to deal with all the underlying particular models.

This section contains a review of the SVM model extensions of interest for this thesis, concluding with the presentation of the general SVM formulation by Chang et al. [27]. Additionally, and as a first minor contribution of this thesis, this formulation is further generalized to include as well the Least-Squares Support Vector Machine model for classification and regression [28].

Note that when discussing these alternative formulations, the original SVM model is sometimes referred in the literature as **Support Vector Classification** (SVC).

2.2.1 Support Vector Regression

text (665 × 665)

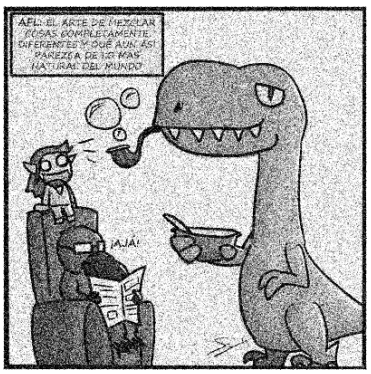

comic (402 × 402)

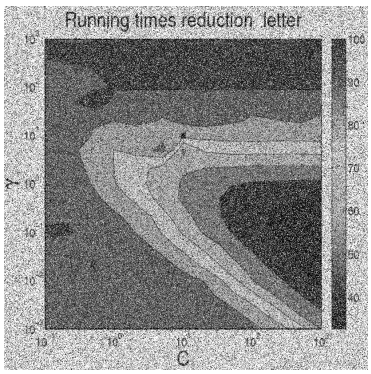

contour (1000 × 1000)

phantom (1713 × 1713)

Figure 22: Noisy versions of images used in the experiments.

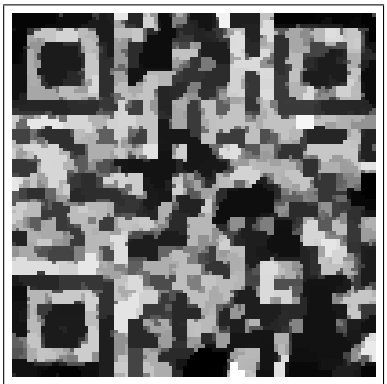

randomQR-0 (100 × 100)

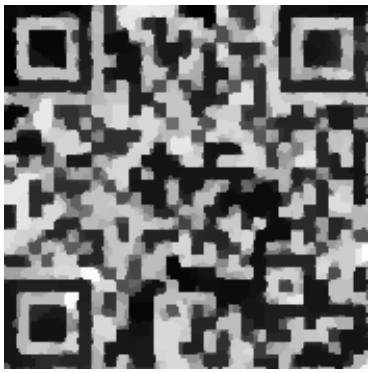

randomQR-1 (175 × 175)

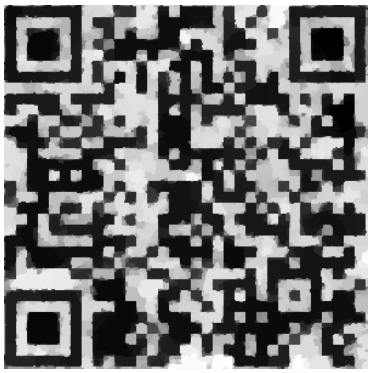

randomQR-2 (300 × 300)

randomQR-3 (375 × 375)

randomQR-4 (500 × 500)

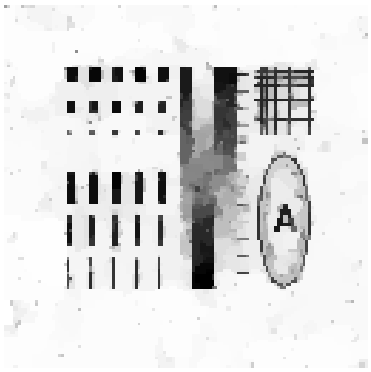

shape (128 × 128)

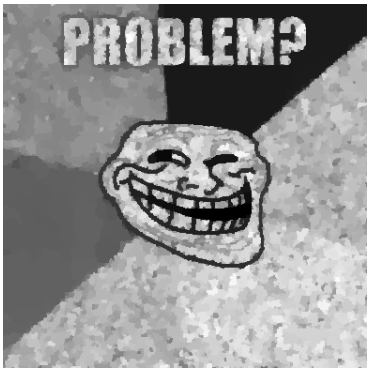

trollface (388 × 388)

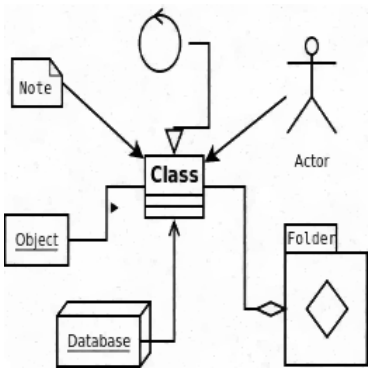

diagram (259 × 259)

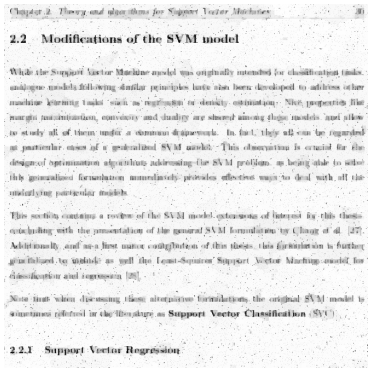

2.2 Modifications of the SVM model

text (665 × 665)

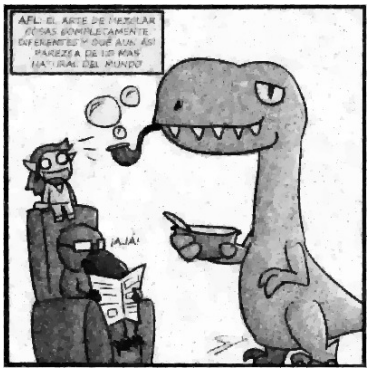

comic (402 × 402)

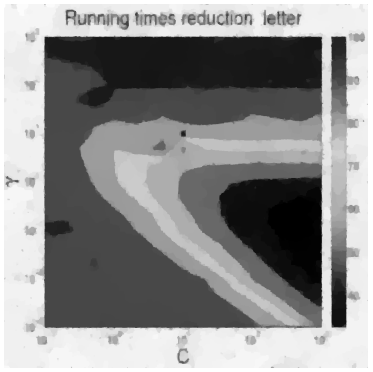

contour (1000 × 1000)

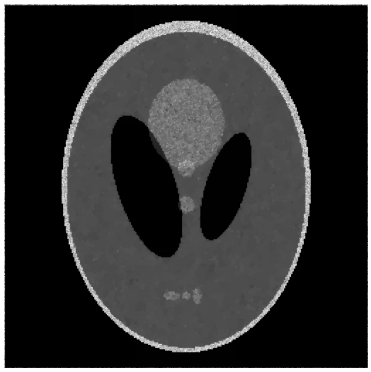

phantom (1713 × 1713)

Figure 23: Denoising results for the test images.

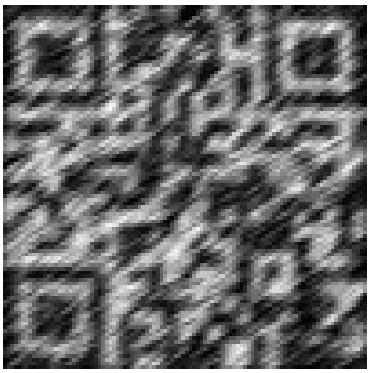

randomQR-0 (100 × 100)

randomQR-1 (175 × 175)

randomQR-2 (300 × 300)

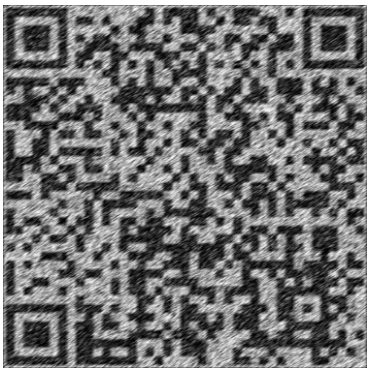

randomQR-3 (375 × 375)

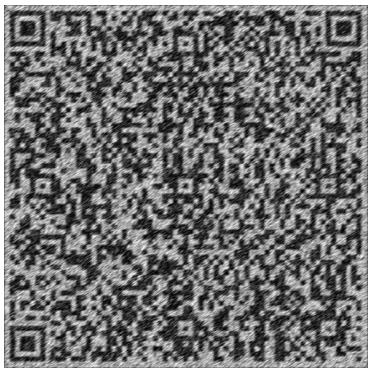

randomQR-4 (500 × 500)

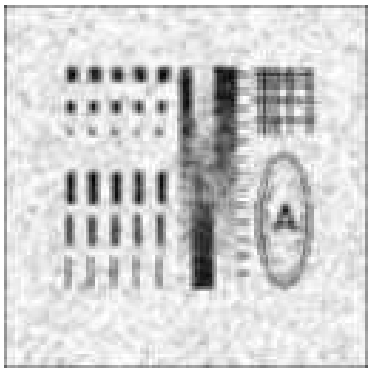

shape (128 × 128)

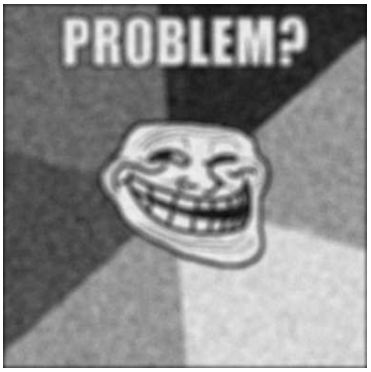

trollface (388 × 388)

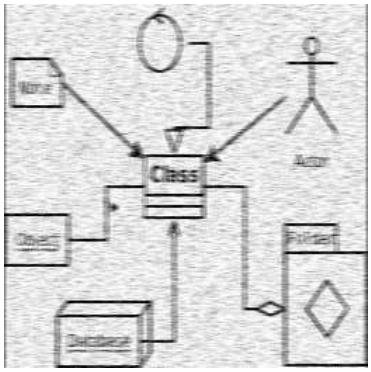

diagram (259 × 259)

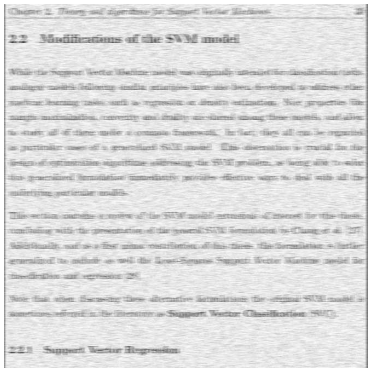

text (665 × 665)

comic (402 × 402)

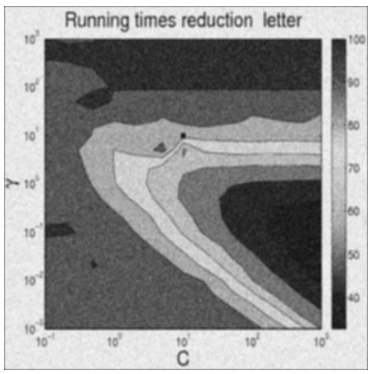

contour (1000 × 1000)

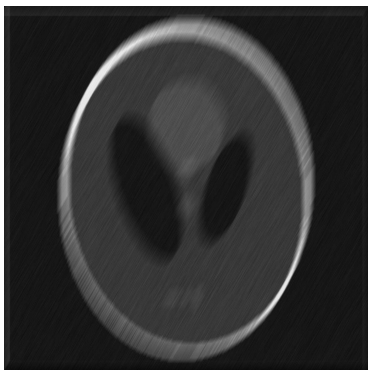

phantom (1713 × 1713)

Figure 24: Noisy and convoluted versions of images used in the experiments.

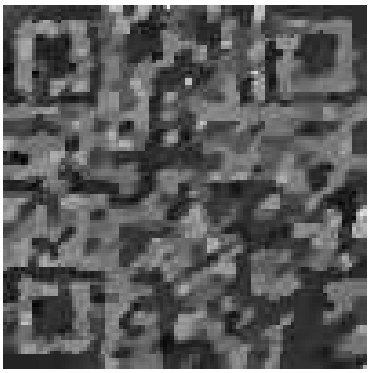

randomQR-0 (100 × 100)

randomQR-1 (175 × 175)

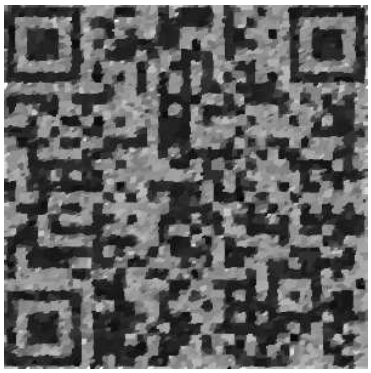

randomQR-2 (300 × 300)

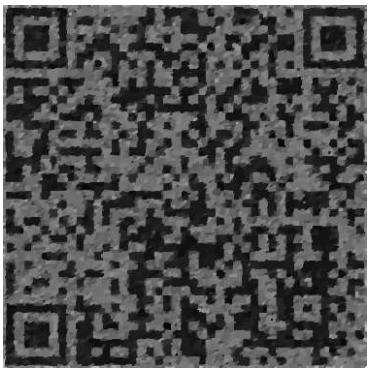

randomQR-3 (375 × 375)

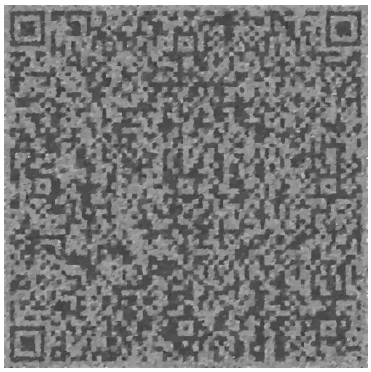

randomQR-4 (500 × 500)

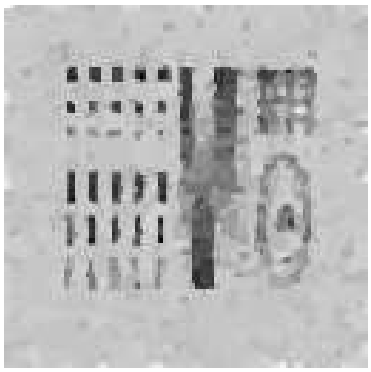

shape (128 × 128)

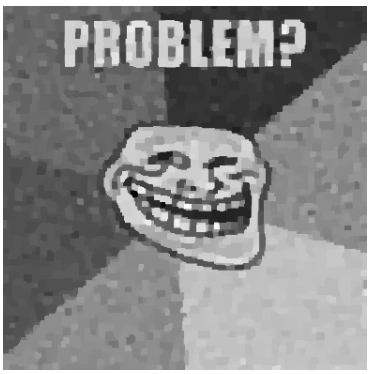

trollface (388 × 388)

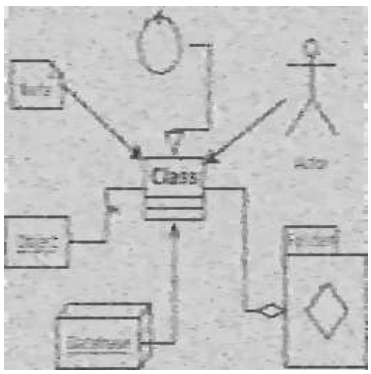

diagram (259 × 259)

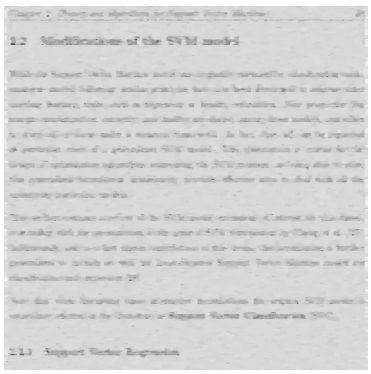

text (665 × 665)

comic (402 × 402)

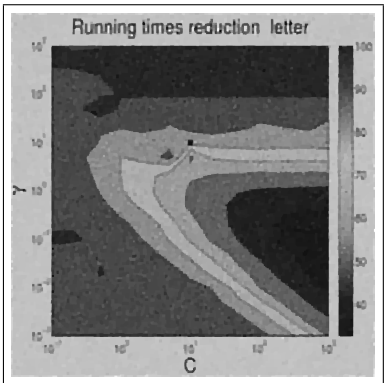

contour (1000 × 1000)

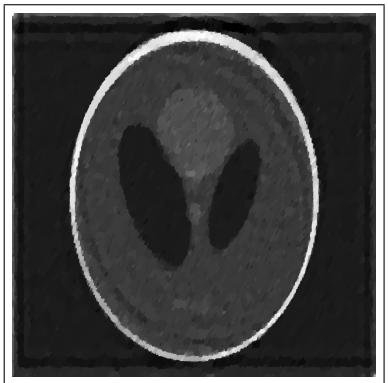

phantom (1713 × 1713)

Figure 25: Deconvolution results for the test images.

Figure 26: A selection of frames from the *salesman* video sequence.

Figure 27: Noisy frames from the *salesman* video sequence.

Figure 28: Denoised frames from the *salesman* video sequence.